

# POLITECNICO DI TORINO

**Corso di Laurea Magistrale in Ingegneria Meccanica**

Tesi di Laurea Magistrale

**Correlation between microstructure, properties and  
process parameters of Ti-6Al-4V products produced  
with EBM**



**Relatore**

Prof. Giovanni Maizza

**Candidato**

Antonio Caporale

Aprile 2018

# Contents

<b>Abstract</b> .....	<b>1</b>
<b>1. Introduction</b> .....	<b>3</b>
<b>2. Additive Manufacturing</b> .....	<b>5</b>
2.1 Electron Beam Selective Melting Process (EBSM) .....	6
2.1.1 <i>Process description</i> .....	7
<b>3. Ti-6Al-4V Powder Material</b> .....	<b>14</b>
3.1 Microstructure .....	14
<b>4. Macro instrumented indentation test</b> .....	<b>17</b>
4.1 Macro indenter prototype.....	18
4.2.1 <i>Vickers indenter</i> .....	20
4.2 Procedure .....	21
<b>5. Experimental work</b> .....	<b>27</b>
5.1 Objectives .....	27
5.2 Manual mode (MM) vs. Build theme mode (BTM) .....	28
5.3 Methods .....	30
5.3.1 <i>Parameters utilized</i> .....	30
5.3.2 <i>Work Procedure</i> .....	31
5.4 Specimens .....	32
5.4.1 <i>Procedure</i> .....	32
5.4.2 <i>Results and comparisons</i> .....	35
5.5 Porosity and density .....	39
5.5.1 <i>Procedure</i> .....	39
5.5.2 <i>Results and comparisons</i> .....	40
5.6 Microstructure analysis.....	45

5.6.1	<i>Procedure</i>	45
5.6.2	<i>Results and comparisons</i>	47
5.7	Tensile test	53
5.7.1	<i>Procedure</i>	53
5.7.2	<i>Results and comparisons</i>	54
5.8	Macro-instrumented indentation test	57
5.8.1	<i>Procedure</i>	57
5.8.2	<i>Results and comparisons</i>	58
5.9	Comparisons between Macro-instrumented indentation test and Tensile test	63
<b>6.</b>	<b>Simplified EBM model</b>	<b>65</b>
6.1	Assumptions	66
6.2	Equations	67
6.3	Powder, solid and liquid material properties	70
6.4	Model structure	74
<b>7.</b>	<b>Inconveniences and future work</b>	<b>80</b>
<b>8.</b>	<b>Conclusions</b>	<b>84</b>
	<b>References</b>	<b>87</b>

# Abstract

Electron Beam Melting Process (EBM) is an additive manufacturing process recognized as one of the most used technologies for the production of metal components for biomedical and aerospace industry. The EBM process gives the possibility to produce components with very complex geometries, ensuring high material density and good agreements with the project specifications. The process is based on the use of an electron beam that melts the powder of metallic material such as Ti-6AL-4V, deposited layer by layer by a rack system, inside a vacuum chamber. In this way, geometries of any type can be created, with materials that would require very complex and expensive treatments with standard machines in terms of time and money.

The following work was carried out by a close collaboration between the University of Rostock and the Polytechnic of Turin. The design and operative phase of the work was carried out at the University of Rostock, while the post-process phase was carried out at the Polytechnic of Turin. The aim of this project was to study the two build modality of the EBM process, the manual mode (MM) and build theme mode (BTM), trying to understand which process mode gives best quality results in terms of microstructure and mechanical properties.

An Arcam EBM® A1 machine, provided by the University of Rostock, was used to produce Ti-6Al-4V specimens (cylinder samples and mechanical tensile test samples). Initially the machine worked with process parameters set by the manufacturer (BTM) with 'speed function 98' enabled, beam current values ranging from 15 to 20 mA (regulated by the "speed function" law, supplied by the manufacturer) and beam speed  $v = 4530 \text{ mm / s}$ . Starting from these standard parameters, it was decided to perform a first inspection to verify the quality of the specimens. Subsequently, it was decided to carry out different tests in manual mode (MM), namely 4 tests keeping constant the beam speed and varying the current of the electron beam and 4 tests using a constant value of the beam current and varying the speed. Once the builds were done, the three best samples achieved in manual mode were chosen: one keeping constant the current at 15 mA with a scan speed of 4530 mm/s, another one with a current of  $I=15 \text{ mA}$  and scan speed of 5900 mm/s and the last one with  $I=12 \text{ mA}$  and scan speed of 4530 mm/s. Both the BTM and MM specimens were tested and studied

through microstructure, mechanical tests and macro instrumented indentation test and comparisons between the two process mode were carried out.

Porosity development and microstructure variations of Ti-6Al-4V alloy were examined through the Archimedes' principle and optical microscopy (OM) with systematic changes of EBM process parameters.

Macro-indentation tests were performed on Ti6Al4V alloy to better understand the material behavior and the relations with mechanical test properties.

Tensile tests were performed to analyze mechanical properties, fracture surface and compare the results with macro-indentation test.

An ad-hoc MatLab model was developed to estimate the temperature distribution of the powder during the build, including the thermal and physical properties of the bulk and powder material. These data were very helpful to both understand the behavior of the material and to find a correlation between the thermal history and the microstructure.

# 1. Introduction

Titanium alloy is considered an interesting material, when properties such as corrosion resistance, high strength/weight ratio, fatigue resistance and cracking are desired. The excessively high cost of these materials, however, limits their applications only for biomedical and aerospace purposes.

As reported in the document [2], compared to materials such as steel, the high cost of titanium does not originate from its rarity (being the ninth most abundant element on the earth's crust and the most abundant sixth metal [3]), but from its complex process of extraction and refining [ [4], [5]]. When the refining process is completed, an important goal is entrusted to find production processes that transform the raw material into a finished product. A multitude of methods are available for metal refining and manufacturing process [2], departing from conventional casting and extractive processes; to final shape using fusion, solid state welding, superplastic bonding, laser welding and recently the use of net shaping and near-net shaping technologies. This includes processes such as powder metallurgy, cold isostatic pressing, stamping and roll compaction, [6] vacuum plasma spray forming [7], friction stir welding and electron beam selective melting (EBSM), among others ( [8], [9]).

Electron beam selective melting (EBSM) “is a very interesting process in which the metal powder is melted, by the action of an electron beam, and rapidly cooled in a single step without any obstacle encountered in casting, forging and powder metallurgy, related with surface reactivity and allowing the segregation of the elements presented on titanium and its alloys” [ [2], [10] [11]]. This additive manufacturing process is very promising to increase the use of titanium and its alloys due to its fast processing, flexibility and non-reactive environmental requirements. Additionally, this technique offers a more efficient and economical way to manufacture titanium parts, by a continuous effort to improve the manufacturing practice itself delivering a higher-quality product and decreasing the cost on post-processing once the part is completed. Therefore the use of EBSM process for processing titanium alloys such as Ti6Al4V, represents a viable alternative to manufacture fully functional parts for aerospace and medical applications at lower cost and lead times. Furthermore, “this technique offers a more efficient and economical way to produce titanium

parts, trying to improve the manufacturing practice itself offering a higher quality product and reducing post-processing costs once the part has been completed. Therefore, the use of the EBSM process for processing titanium alloys such as Ti6Al4V represents a viable alternative to manufacture fully functional parts for aerospace and medical applications at lower costs and lead times” [2].

Reviewing the literature, several authors have studied the evolution of the microstructure and mechanical properties of the Ti6Al4V ([12], [13], [14], [15], [16], [17], [18], [19] [20] [21] [22]) according to different process parameters. Nevertheless, limited research has been focused on exploring and making comparisons about the microstructural and mechanical properties of Ti6Al4V products manufactured with the two EBM process build modality: the Manual Mode (MM) and Build theme mode (BTM)). There is only one research that studied the variation of mechanical and microstructural properties with the two build mode [23]. This study [23] has the goal to investigate the microstructure and mechanical properties variations as a function of distance from the build plate for the two normal EBM build methods. Other additive manufactured Ti-6Al-4V studies used only one of the two build methods ([24], [25] etc..).

With this purpose, an overall review of the two process modality were conducted here to understand which one gives best quality specimens.

In the present study, porosity development and microstructure variations in Ti-6Al-4V were examined for the both EBM process mode. A systematic changes of EBM process parameters (scan speed and beam current) for the MM and a set of pre-assigned parameters for the BTM were used. An optical microscopy (OM) (LEICA DMI 3000M microscope) has been used for metallographic inspection. A macro instrumented indentation test was performed for each process mode using a Vickers indenter (HV). Tensile test was also performed for each process mode and some comparisons were made with the macro instrumented indentation test.

Furthermore, to better understand the behavior of the material during the process and trying to find a correlation between process parameters and microstructural / mechanical properties, a refinement of a numerical model representing the temperature distribution during the built, including the thermal and physical properties of the material being processed, was developed.

## 2. Additive Manufacturing

Nowadays, additive manufacturing (AM) is recognized as a promising manufacturing technology for metal parts [1]. In the latest 30 years, AM technologies have been studied and some have been made commercially available [2], such as selective laser melting (SLM), laser metal deposition (LMD) and electron beam melting (EBM) (as presented in [26], [27], [28], [29]). AM technologies are very important for the development of new materials and parts, when design, process conditions and lead times are difficult to achieve by conventional methods such as casting or extraction methods ([2], [30]).

As reported in the following work [2]: “ Powder metallurgy made its appearance as an attractive option, to manufacture net shape custom parts in a short period of time through heating of and subsequent pressure application to the part by hot isostatic pressing process HIPS [31] to obtain minimum porosity values. For this purpose, a new series of processing methods consisting on an additive free-form principle made its appearance, enabling the processing of low and high melting temperature materials. These techniques were mainly classified according to the delivery method for the additive material, the source used for agglomeration, the state of the material prior to deposition and the material temperature process condition. When high melting point materials were to be processed, higher-heat sources were used, especially for metals and ceramic materials. For these reasons, two different methods were designed to deliver the material prior to processing.

The first method developed was direct-melt processing, consisting of selective delivery of metal and ceramic materials to the location of deposition (i.e. Laser Engineered Net Shaping – LENS) providing extensive flexibility for processing, tolerances and build time.

The second method designed was the powder bed process, where a layer of powder is placed on the build plate and a heat source such as a laser or an electron beam, selectively melts the area of the part, with the remaining powder material acting as a structural support, maintaining a stable built temperature thanks to the low thermal conductivity on the loosely sintered powder. Several manufacturing techniques using a powder bed as an initial process stage made their appearance in this arena, such as laser assisted additive manufacturing (LAAM). One of the most remarkable techniques is the selective laser sintering (SLS), in which the powder material is partially sintered below its melting temperature, followed by a high peak laser to melt the powder material. This process allowed the manufacturing of a

wide range of materials, from polymers to metals, using single or mixed composition powders. Even though this alternative seems effective for many applications, there are still limitations involving the use of a laser as a heat source such as:

- a) *High power requirement to melt metal powders:* As the power is increased, the penetration depth is decreased, requiring a higher laser dwell time disabling the control on adverse processes like recrystallization and annealing [32] .
- b) *Restricted thermal capacitance of the mirror galvanometer :* Together with a high inertia of the mirrors within the scanning system, prevents the laser track accuracy [ [33], [34].
- c) *Longer dwell times represent longer process time and higher costs.*
- d) *Material sensitivity to environmental contamination:* Corrosion or stress cracking is induced by atmospheric contamination as well as the gas shielding reacting with the processed material in the case of atmospheric or pressurized
- e) *Power efficiency:* Related with the limitations of processing materials with high laser reflectivity (i.e. native metal oxides)
- f) *Low beam quality of high beam lasers*

These delivered power and scan speeds limitations on SLS technologies led to the development of a new technology emerged from a conventional method in which an electron beam was initially used to melt and refine materials highly susceptible to corrosion and environmental contamination ( [35], [36]). This gave birth to the Electron Beam Selective Melting process (EBSM) first designed by ARCAM AB, consisting of a focused, high-energy electron beam, deflected by magnetic lens, melting the powder material in a layer-by-layer fashion to build a physical part”.

## 2.1 Electron Beam Selective Melting Process (EBSM)

Electron beam melting (EBM), as laser engineering net shape (LENS) , direct laser deposition (DLD) and direct laser fabrication (DLF) respectively, is one of additive manufacturing techniques. In this method, metallic objects are produced directly from

computer aided design (CAD) files by melting the metallic powder utilizing focused high energy beam [37]. “EBM has been successfully used in AM with various metals. For example, Murr et al. [38] produced titanium aluminide alloy components via EBM. Cormier et al. [39] fabricated parts made of tool steel. Murr et al. ([40] , [41]) manufactured EBM parts made of nickel-base superalloy. Ramirez et al. [42] and Frigola et al. [43] also fabricated copper components by EBM” [1].

One of the disadvantages of the EBM process is the inability to manufacture parts avoiding machining and welding. “Koike et al. [12] and Suard et al. [13] showed that the surface produced by EBM has a significant roughness, containing a ridged structure with visible sintered powder grains. Therefore, the surface roughness produced by EBM can be unfavorable, especially for products where a smooth surface is required” [1].

The main advantages of using the electron beam systems for the fabrication of 3D metal structures include [37]:

- 1) The purity of the deposit due to the controlled atmosphere
- 2) Reduced segregation due to rapid quench rates
- 3) Reduced heat affected zone due to small melt pools
- 4) Verifiable deposition conditions due to imaging and feedback process control, and possible five-axis control [45]. The five controllable axes are beam energy, scanning speed, offset focusing and 2D scanning on the powder bed. These controllable parameters are defined as system processing parameters.

Because quality standards require an optimized set of processing conditions to ensure the quality and consistency of microstructures [46], the EBM or DLD process offers considerable potential for controlling the structure and metallurgical structure through the use of appropriate set of parameters [47].

## 2.1.1 Process description

The process is initiated by using a CAD software, drawing the part that has to be manufactured. After that, the 3D information is processed, discretizing the 3D model into a set of 2D level sections (x, y coordinates) and the z axis is set by the thickness of the single

layer, controlled by the build etch within the additive system. The part is then processed, layer by layer, until the final shape is obtained [2].

In this work an Arcam EBM ® A1 was used. The principle of the process is illustrated in [Figure 1 ]. This system consists of the **electron beam compartment** and the **build part compartment**.

To emit electrons, “a doped tungsten wire is heated to about 2600 °C, then an accelerating electric field is applied on the grid and an electron beam is formed. The beam power can ranges from 50-3000 W during the process and the width of the beam is fully adjustable within the different process steps (e.g. 0.1 - 0.8 mm). The electron beam passes the anode into a ceramic tube, where three different magnetic coils are located (The astigmatism coil, the focus coil and the deflection coil) [Figure 2]. The electron beam is accelerated to 60 kV and the maximum beam current can be 50 mA. The electron-magnetic deflection lenses allow the scan speed of electron beam to reach a maximum value of 8000 m/s” [48]. In order to use high quality electron beam as well as to reduce oxidation and contamination of titanium parts, the build environment is kept under a high vacuum  $10^{-5}$  mbar.

Below there is a schematization of the EBM column and the three magnetic coils [Figure 2].

- The upper part of the column contain an electrode unit (consisting of a filament and grid cup), an external air cooling coil and an internal oil system for cooling.
- The middle column contains the anode, a drift tube and the turbo-pump connection.
- The lower column contains the control coils for the beam and an internal water cooling system.

The energy density within the electron beam can amount to  $106 \frac{kW}{cm^2}$ . To actuate the electron beam, the electron beam gun uses electromagnetic lenses (referred to as deflection coils) enabling the electron beam to scan the metal powder surface from one side to the other and melt the powder at certain positions where required. The coils allow to govern the parameters that drive the electron beam, the functionalities of each coil are as follows:

- The **astigmatism coil** control the shape of the beam.
- The **focus coil** allows to change the focal angle of the beam (spot radius).
- The **deflection coil** control the position of the beam, changing the angle and the direction.

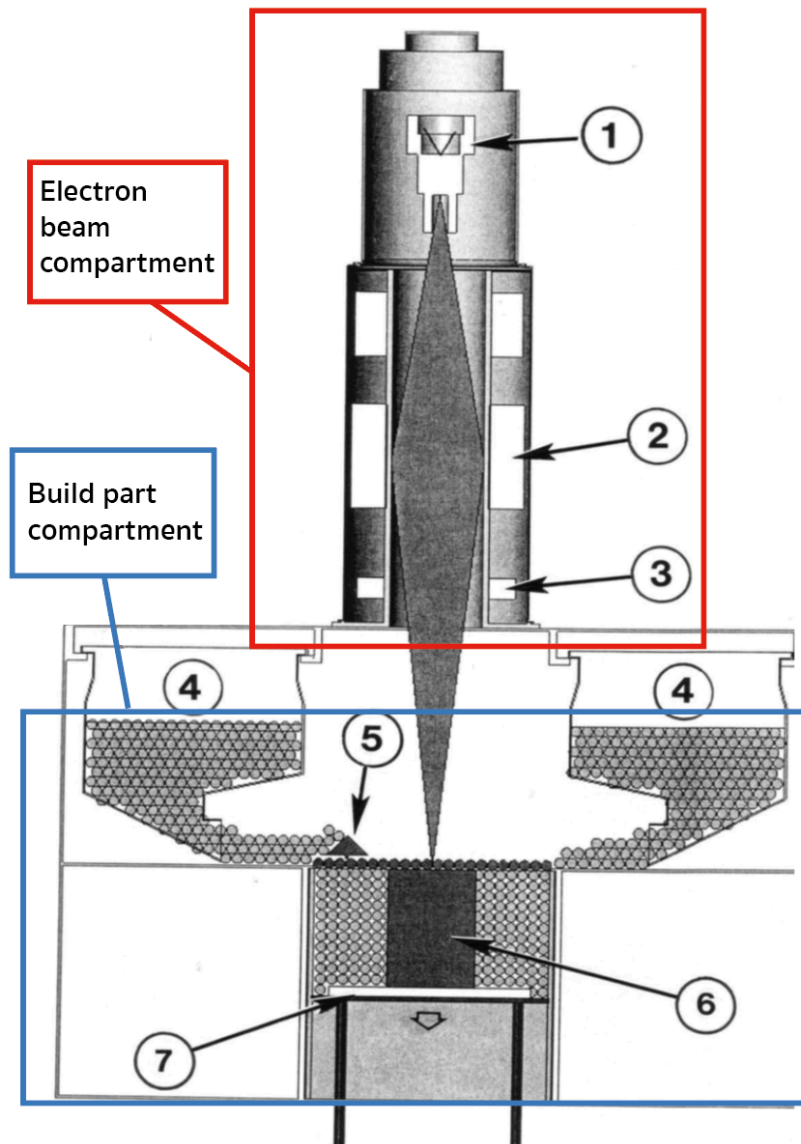


Figure 1 EBM system layout. Numbers denote the system components: (1) Electron gun, (2) Beam focus lens, (3) Beam deflection coils, (4) Powder hopper, (5) Powder layer rake, (6) Build product, (7) Build table. From Gaytan, et al. (2009) [49].

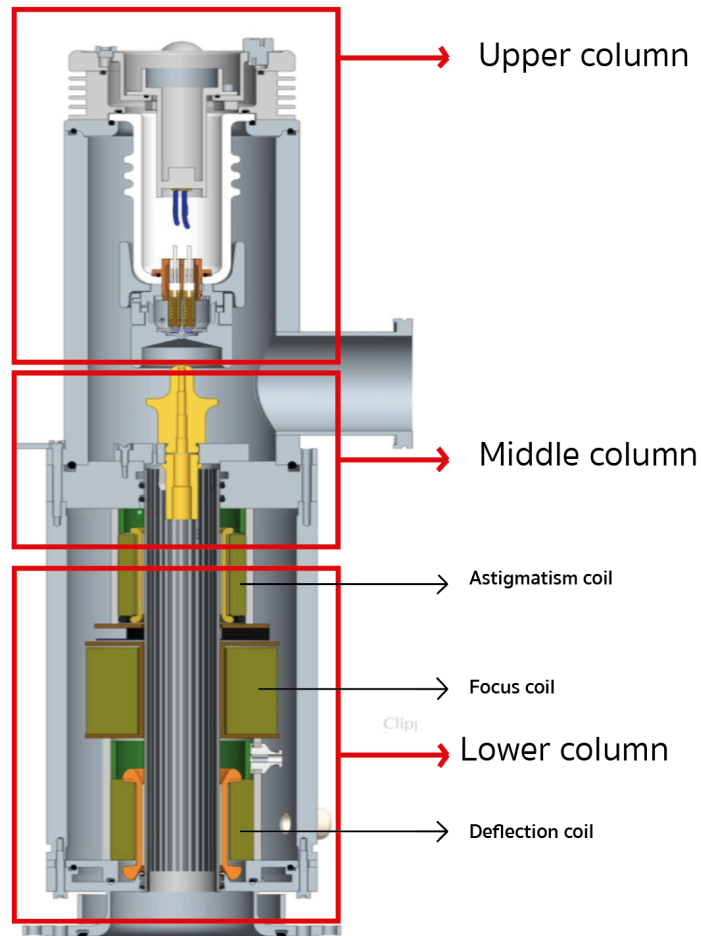


Figure 2 Schematization of the electron beam compartment from [48].

The **build part compartment** contains both two powder hoppers to supply metal powder and a rake to spread the powder during the layering process on a build table [1], [Figure 1]. The main part of the build compartment is the powder tank 250mm x 250mm x 350 mm. Initially the build start plate (210mm long by 210mm width and 10mm thickness stainless steel), is aligned with the plane of the machine through an adjustment screws wheel system [Figure 4]. The 4 supports shown in [Figure 4] allow both an alignment with the plane of the machine and a stability of the build plate, preventing it from vibrations or movements during the process. The plate plane is manually aligned with the plane of the machine adjusting the height of the screws wheel ensuring that the thickness of the powder spread is constant and uniform. For this reason, the plate alignment system turns out to be quite inaccurate and time consuming, in fact every time a new job has to be started, a re-align of the construction plate is needed and the procedure should be run all over again. It should be noted that, before

positioning the plate, the underlying space should be filled with powder, ensuring a good contact between the thermocouple and the build plate [Figure 3].

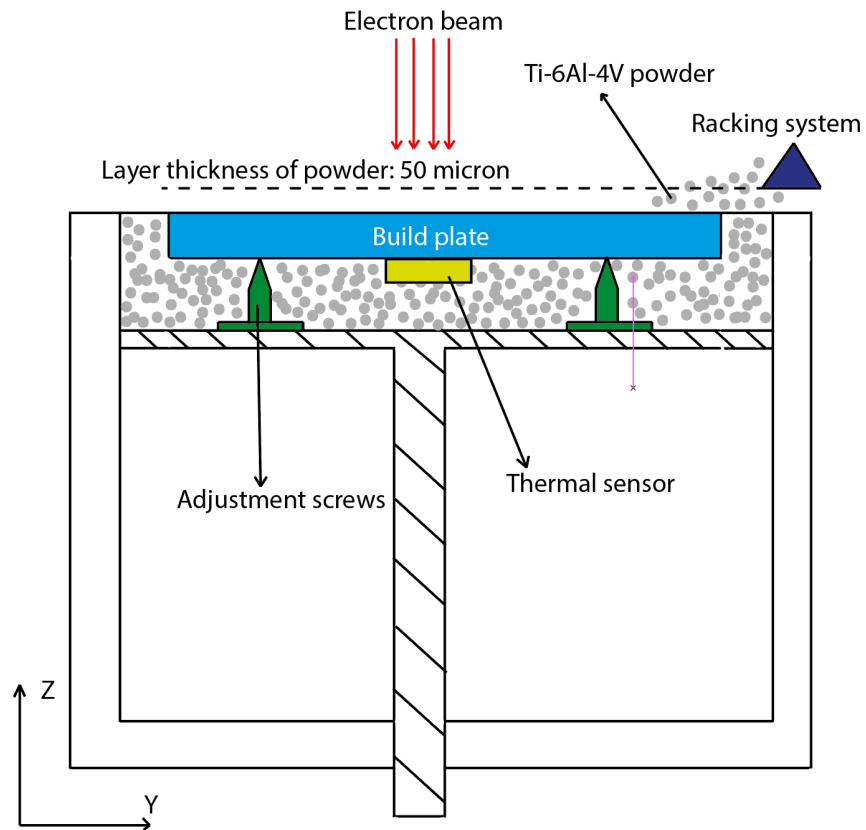


Figure 3 Building feature process.

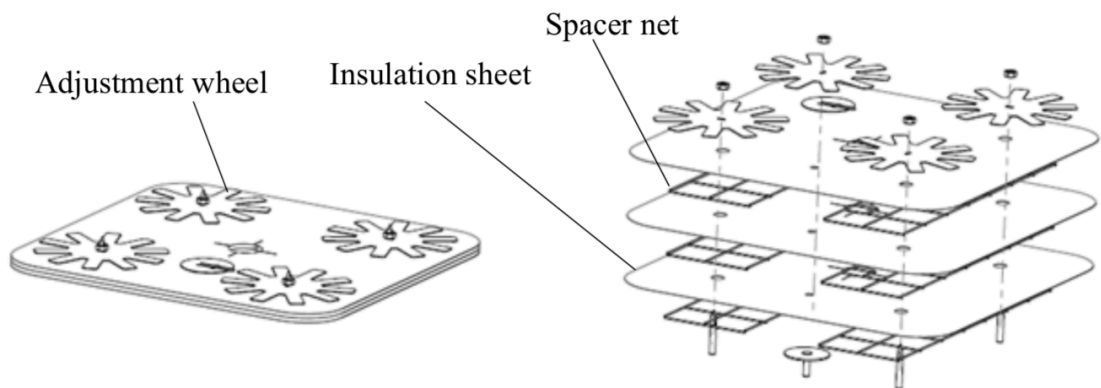


Figure 4 Adjustment screws wheel system, from [48].

“Once the build plate has been properly aligned within the metal powder, the EBSM process is initiated by closing the system and pumping down the chamber to  $\sim 10^{-5}$  mBar. When this base pressure is attained, the build plate is heated by the electron beam from room temperature to  $\sim 475^{\circ}\text{C}$ , using a defocused electron beam [Figure 3], with a relatively low

beam current and a relatively high scan speed. Afterwards, a degassing process takes place for 10 minutes, so species like water vapor can be desorbed from the surface of the plate. Once degassing is concluded, the temperature of the build plate is increased by the electron beam until it reaches 730 °C, corresponding to the initial build temperature. After the build plate pre-heating process is finished, the build plate moves 50 microns along the Z axis, and the first powder layer (with a powder thickness larger than 50 microns, considering the gap between the racking system and the racking surface seen in [Figure 3]) is placed by the racking system. Subsequently the powder layer has been preheated to induce a partial sintering, improving the thermal conductivity during the build, diminishing the possibility for particle charging and powder spreading and holding the powder in place during subsequent melting at higher beam powers” [2].

Afterwards, the outer part of the specimen is melted and is referred as ‘contour’. ”The contour provides an interface between the actual build and the surrounding powder, in particular, outer contouring should be more important than inner contour because it may determine the building of thin parts. A contour melting also provides an opportunity to have good surface structure. The second step of melting the actual part is build within the contours” [37].

As well described also in [2], once the first layer has been melted, the build plate is lowered by one layer thickness, additional powder is delivered from the powder dispensing hopper and raked over the previously solidified layer and the process will be repeated layer by layer, until the melting part is finished. After the building stage, the part is cooled down either under vacuum or helium flow until the sample part reaches 100°C. Cleaning of the parts from adherent partly molten powders is done by powder blasting with the same powders as used in the building process. The removed powders can be reused after sieving in a new process [5].

To sum up, some advantages of using the electron beam technology are reported below:

- High energy density during the entire process.
- Possibility to obtain very fast melting speed.
- Relatively low level of energy emitted to the ambience.
- High efficiency.
- Clean melt by virtue of using vacuum.

- Low energy consumption.
- Different combinations of materials could be used in the powder.

# 3. Ti-6Al-4V Powder Material

## 3.1 Microstructure

EBM is the AM technique typically used to manufacture Ti-6Al-4V parts because of titanium high affinity for oxygen. Several works ([50], [51]) have studied the possible Temperature / Time microstructure evolution of the Ti-6Al-4V alloy, and referring to some hypotheses and verifications, several conclusions have been obtained even if they all are quite similar to each other. The results of the studies ([50], [51]) about the processes transformation of the material are reported below, and they were compared with the following thesis work results in the chapter [5.6.2]. The microstructure that was usually found in Ti-6Al-4V products, made with EBM, was mainly composed of  $\alpha + \beta$  dual-phase alloy ([50], [51]). The addition of aluminum let the stabilization of the  $\alpha$  phase and the increasing of the strength of the alloy, the addition of vanadium stabilizes the  $\beta$  phase and increases the ductility of the material. According to [50] and [51], the microstructure consists of columnar prior  $\beta$  grains delineated by grain boundary  $\alpha$  and a transformed  $\alpha + \beta$  structure with both colony and or Widmanstätten morphology within the prior  $\beta$  grains ([52], [53]). The columnar  $\beta$ -grains formed due to the extreme solidification conditions and the strong partitioning behavior of the main alloying elements in Ti-6Al-4V [50]. Because the material is subjected to rapid cooling, solidification and very long maintenance at the temperature of  $\sim 650^\circ\text{C}$  (annealing), the resulting structure is a consequence of non-equilibrium processes that give life to a "graded microstructure" [50].

It should be pointed out that the existence of  $\alpha'$  martensite in EBM-built Ti-6Al-4V samples is still debatable. "It is known that a full martensite microstructure forms when untransformed  $\beta$  is rapidly cooled down below the martensite start temperature ( $M_s$ ) with a sufficiently high cooling rate. However, a variety of  $M_s$  and critical cooling rates for martensite formation in Ti-6Al-4V were reported in ([54], [55], [56]). As it is shown in the previous documents the accurate cooling rate of EBM process is unknown, but it is confirmed to exceed at least  $410^\circ\text{C s}^{-1}$ . Similarly, the surface temperature of the build should be below  $800^\circ\text{C}$ . Therefore, martensite is supposed to form during EBM-built Ti-6Al-4V process" [50]. Based on the work of ([57], [50], [51]), the microstructural

evolution of EBM-built Ti-6Al-4V could be simplified as the following processes illustrated in [Figure 5] [50]: “(i) starting from the liquid state ( $T > T_{\beta \text{ Transus}}$ ) [Figure 5], rapid solidification occurs (up to temperatures slightly lower than  $T_{\beta \text{ Transus}}$ ) leading to the formation of prior  $\beta$  grains [Figure 6 (i)]; (ii) The rapid cooling from temperatures above  $\beta$  transus (1000 ° C at 4% of vanadium) up to the temperature of 600-650 ° C leads to the formation of martensite,  $\alpha'$  phase [Figure 6 (ii)]; (iii) the near-isothermal annealing at 650 ° C allows the transformation of martensite into an  $\alpha$  Colony & Basket-weave +  $\beta$  Rod structure at the build temperature [Figure 6 (iii)]. In particular, by observing the [Figure 6] of the document [51], discrete  $\beta$  particles will first form along  $\alpha'$  martensite plate boundaries and then continuously grow at expense of vanadium (ii  $\rightarrow$  iii).  $\alpha$  phase continuously grows at the expense of  $\alpha'$  and  $\beta$  rods due to the ejecting vanadium from growing  $\alpha$  [51]. The discrete  $\beta$  particles may be connected and  $\beta$  rods would eventually form at the fully decomposed  $\alpha$  plate boundaries (iii  $\rightarrow$  iv)” [50] [Figure 6].

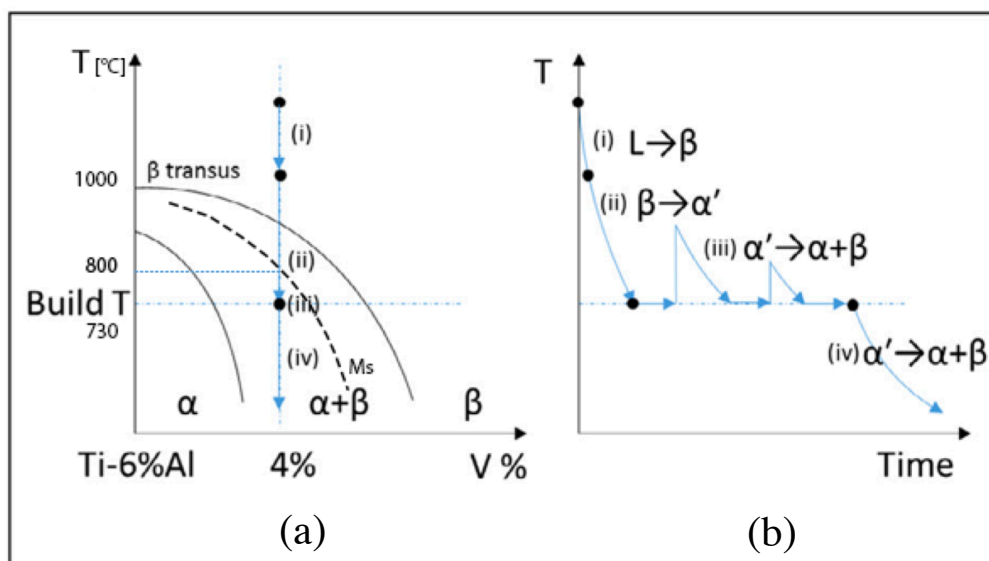


Figure 5 (a) Schematic phase diagram of Ti-6Al-4V and (b) simplified thermal process showing the four main phase transformation processes involved in EBM-built Ti-6Al-4V. From [50].

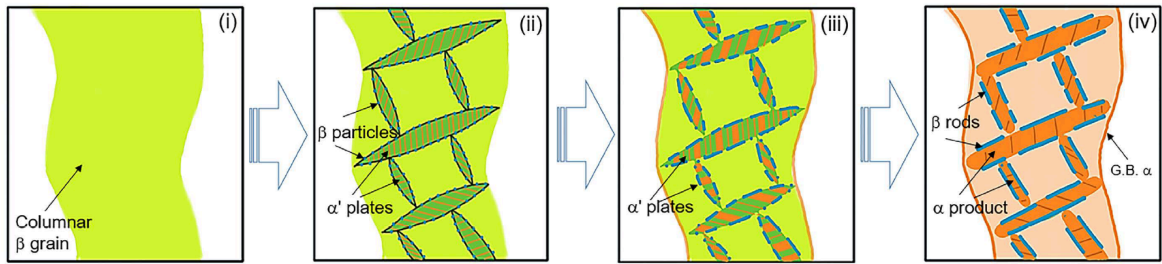


Figure 6 General microstructural evolution of EBM printed Ti-6Al-4V. From [51].

“Ti-6Al-4V undergoes a near-isothermal heat treatment at the build temperature during the overall process. The previously built layers undergo a longer annealing compared to the subsequent layers and cooling rate will constantly change with the increasing build height, which would significantly impact on the length scale of microstructure “ [50]. The following picture [Figure 7] shows an overall scheme of EBM-built Ti-6Al-4V, given by the results of [50].

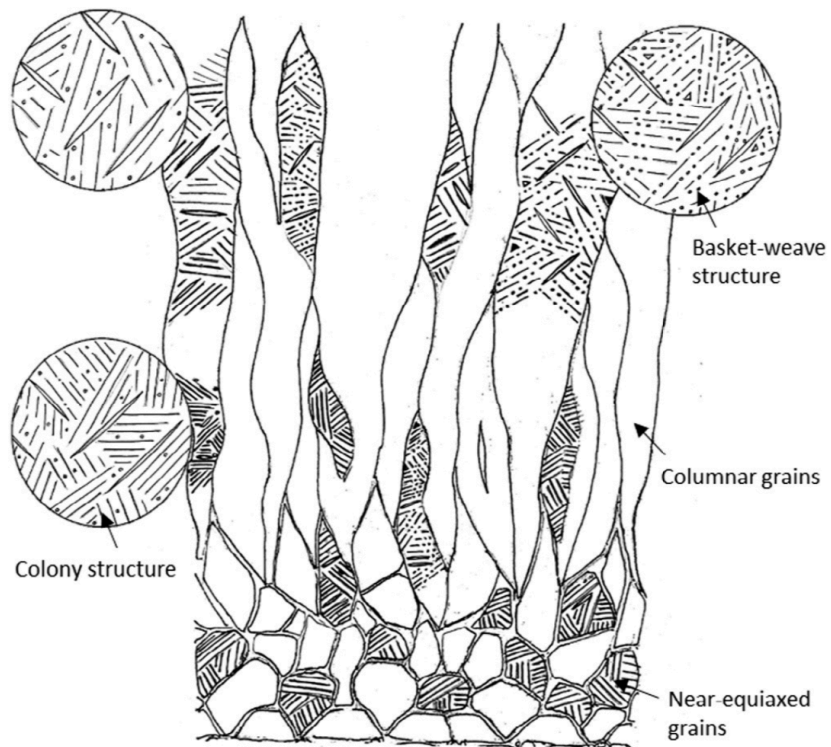


Figure 7 Schematic microstructure of EBM-built Ti-6Al-4V on X-Z plane. The bottom part is closer to the start build plate, the top part correspond to the last deposited layers. From [50].

# 4. Macro instrumented indentation test

Macro instrumented indentation test is an unconventional mechanical test, classified as a non-destructive test, for the determination of the mechanical properties (typically obtained with the tensile test) of small and simple samples. The study [57] was carried out at the Department of Materials of the Polytechnic of Turin, where the following thesis work was also carried out, and it reports a comprehensive analysis of the macro instrumented indentation test from which some results and reflections were taken. As already outlined in [57]: “The conventional hardness tests are typically performed as a quality control and to roughly estimate the yield stress of metallic materials. The disadvantage is that many mechanical characteristics of the material are taken into account and the method is ineffective in the extraction of the single effects. To overcome these limits the IIT has been developed, with continuous recording of forces and displacements during an indentation cycle allowing to obtain the so-called indentation curves (ICs). According to an elastic contact model proposed from Sneddon in 1965 [59], the discharge portion of the IC provides sufficient information to extract the elastic modulus and the indentation hardness. These parameters can be exploited effectively for a universal mechanical test. The IIT is currently widespread and widely exploited in the nanometer and micro-hardness range (i.e. load less than 2 N). These allow to determine the mechanical properties of very small samples but they are not always representative of the bulk mechanical behavior. The macro hardness range (load between 2 N and 30 kN) is considered the most suitable to characterize the elastic and plastic behavior of structural materials and to establish a possible correlation between indentation and tensile properties, as suggested by ISO / TR 29381: 2008 (E) [60]. The macro range is not limited to bulk materials but may be suitable for the study of layers, multilayers and coated material if the influence of the substrate on the elastic measurements and the thickness effect can be properly evaluated ([61] [62] [63] [64] [65]). Interestingly, the macro range is considered the most likely to establish a possible correlation between indentation and tensile properties [60]. According to Mayer definition, the hardness is an actual contact pressure independent on the indenter geometry or on the imposed load [66]. The indentation

hardness HIT available from IIT exploits Meyer definition. The IIT attempts to extract and evaluate the effect of individual characteristics from a complex measure, such as conventional hardness. In fact, unlike conventional Vickers, Brinell and Rockwell hardness tests, IIT hardness testing is not performed when plastic deformation is completed, but is based on a large number of simultaneous measurements of the force applied by the penetrator and the corresponding indentation depth in the tested material. The resulting indentation curves (ICs) contain information on both elastic and plastic behavior and are post-processed to extract the equivalent conventional hardness (Vickers or spherical) but also the elastic properties and many indentation parameters, such as the HIT indentation hardness” [57].

## 4.1 Macro indenter prototype

As described in the document [57], “instrumented indentation tests are performed on the macro-indenter prototype OMAG SR HU 09 [Figure 8] under force control [67]. It essentially consists of an electric Sanyo Denki AC motor (power 100W, 0.353 Nm torque, 3000 rpm rotation speed) which drives the indenter connected to a force transducer. A gear box allows a controlled speed of approach (from 5 to 40  $\mu\text{m/s}$ ) of the indenter to the sample during the initial stage. In the approaching stage, the position and velocity of the indenter are thus transmitted by an encoder balanced by a pair of springs (as detailed in Figure 5.1 (b)).

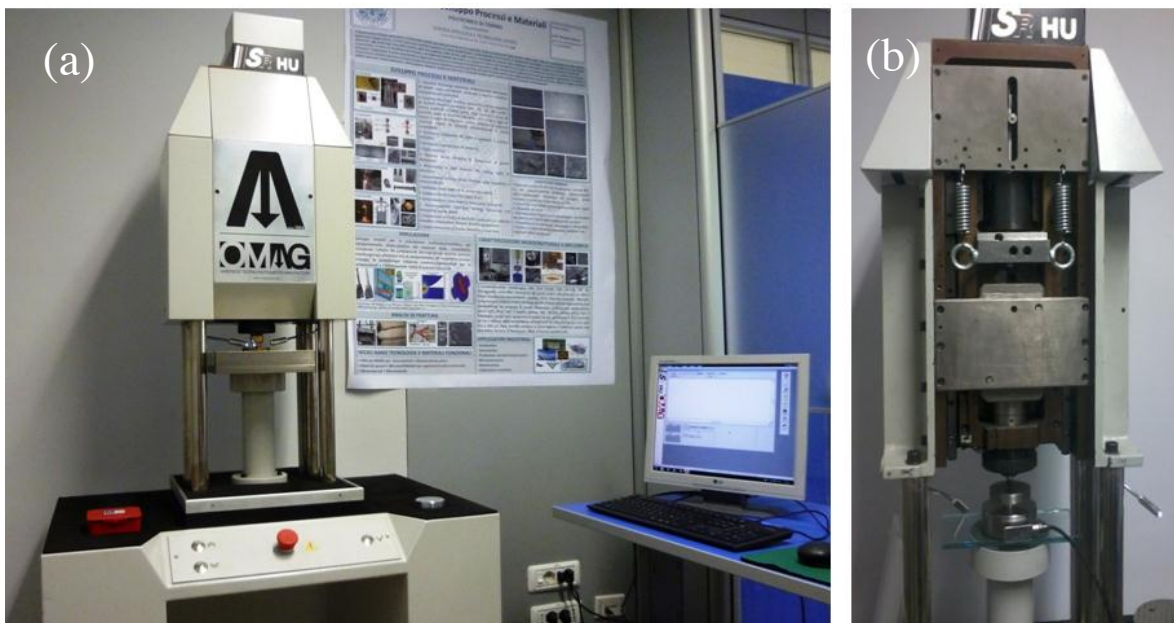


Figure 8 (a) OMAG SR HU 09 macro-indenter prototype; (b) detail on the measuring head balanced by spring, From document [57].

Load and displacement are measured with a load cell and a linear variable differential transformer (LVDT), respectively. The load cell (measuring range from 0 N to 2500 N) gives a relative error of 0.008% and a repeatability of 0.1% of full scale value. The technical specification of the LVDT (measuring range from -0.63 mm to 0.63 mm) gives only the repeatability, which is 0.01% of the full scale value. The sampling frequency is 1000 Hz. The imposed indentation force-time cycle usually consists of 60 s loading time, 60 s holding time and 40 s unloading time. As suggested by ISO 14577-4 [68], the force removal rate has been set higher than the loading rate to minimize the influence of creep. During IIT, the specimen is held in place by a special ratchet that provides a reference point for the displacement transducer, as shown in [Figure 9] ([69], [67]).

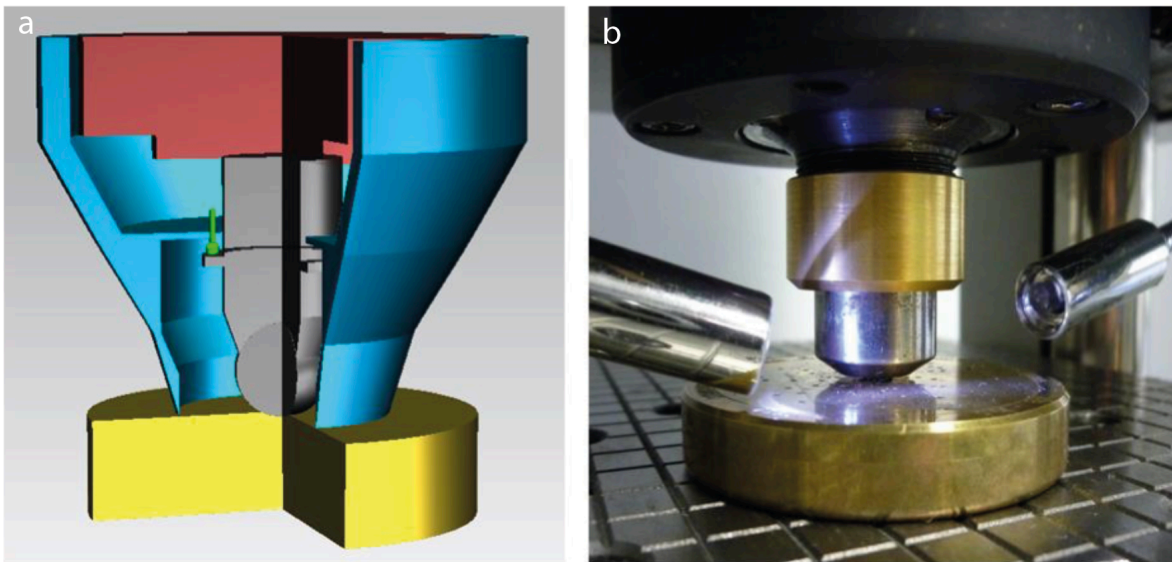


Figure 9 (a) Schematic of the core of the OMAG SR HU 09 (force transducer/fuchsia, reference ratchet/blue, LVDT/green, indenter/grey, sample/yellow); (b) Detail of the reference ratchet. From [57].

The displacement transducer measures the indentation depth between the surface of the tested material by means of the reference ratchet and the indenter tip by the indenter holder, thus reducing to a minimum the path common to both force and displacement, as shown in [Figure 10]” [57].

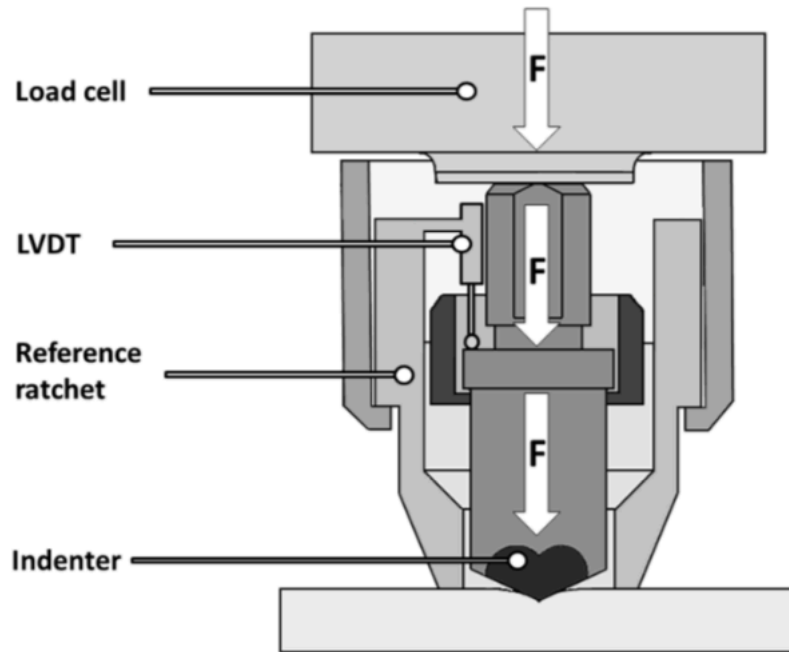


Figure 10 Schematic representation of the path common to force and displacement. From [57].

### 4.2.1 Vickers indenter

In this work, the same Vickers indenter of reference [57] was used. “The Vickers indenter was calibrated with reference to BS EN ISO 6507-2 [70], ASTM E92- 82 [71] and ASTM E384-10 [72]. The calibration report quotes a mean apex angle of  $136.11^\circ$  with an expanded uncertainty of  $0.05^\circ$ . The expanded uncertainty on the line of the junction between opposite faces (i.e. offset) is equal to  $0.25\ \mu\text{m}$ . [Figure 11] shows the actual Vickers indenter” [57].

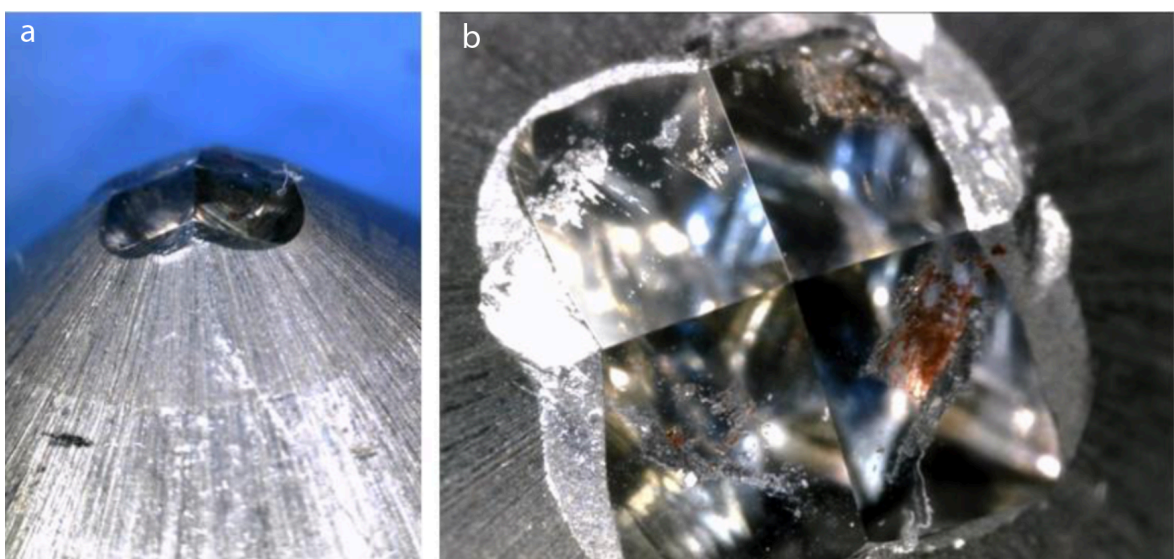


Figure 11 (a) Actual geometry of a Vickers indenter; (b) detail of the indenter tip. Note that some metallic contaminants, deposited on the edge of the square, may distort the test results [73]. From [57].

## 4.2 Procedure

The Macro indentation test procedure was the same used in [57]. “Instrumented indentation test records the loads and the displacements of an indenter during a controlled loading-holding-unloading indentation cycle by means of specific sensors. The quantities measured at the same time are the applied force  $F$  and the indentation depth  $h$ . The results deduced from indentation curves (ICs) are depicted in [Figure 12]” [57].

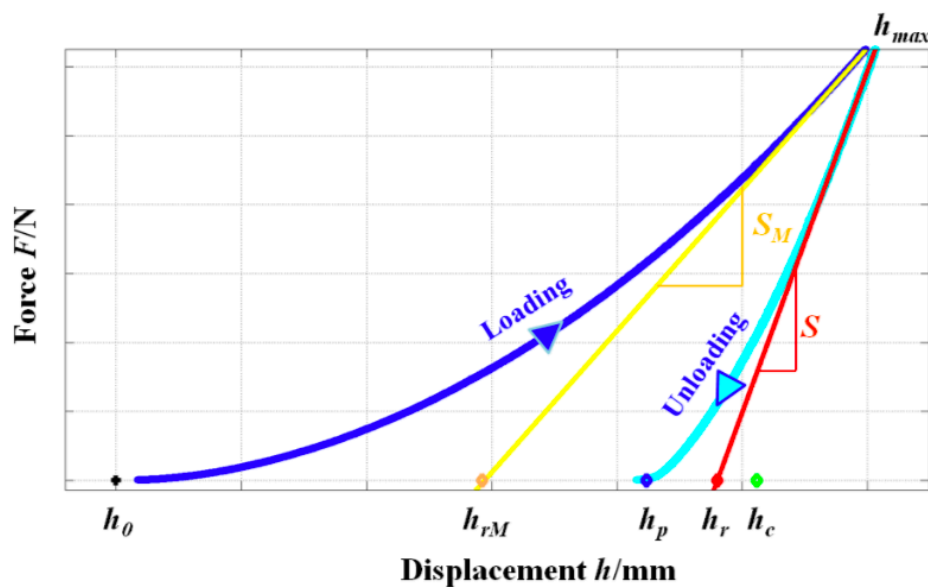


Figure 12 Schematic of an indentation curve. From [57].

The ICs allow to extract many relevant indentation parameters:

- $h_0$ : the zero point, i.e. the first point of contact
- $h_{max}$ : the maximum depth of penetration of the tip into the sample
- $F_{max}$ : the maximum applied load
- $S_M$ : the tangent to the loading curve at  $h_{max}$
- $h_{rM}$ : the intercept of the tangent to the loading curve at  $h_{max}$
- $S$ : the tangent to the unloading curve at  $h_{max}$
- $h_r$ : the intercept of the tangent to the unloading curve at  $h_{max}$
- $h_c$ : the contact depth

-  $h_p$ : the plastic depth, i.e. the last contact point corresponding to the result of the plastic deformation of the residual indentation when the elastic deformation is fully recovered.

Indentation parameters enable to evaluate, without any optical microscope and operator dependency [74], the contact area  $A_c$  involved in the IIT definition of hardness. Following the procedure reported in the reference [57] and in the ISO 14577, “ for the Vickers indenter geometry [Figure 13], the superficial area and the contact area are:

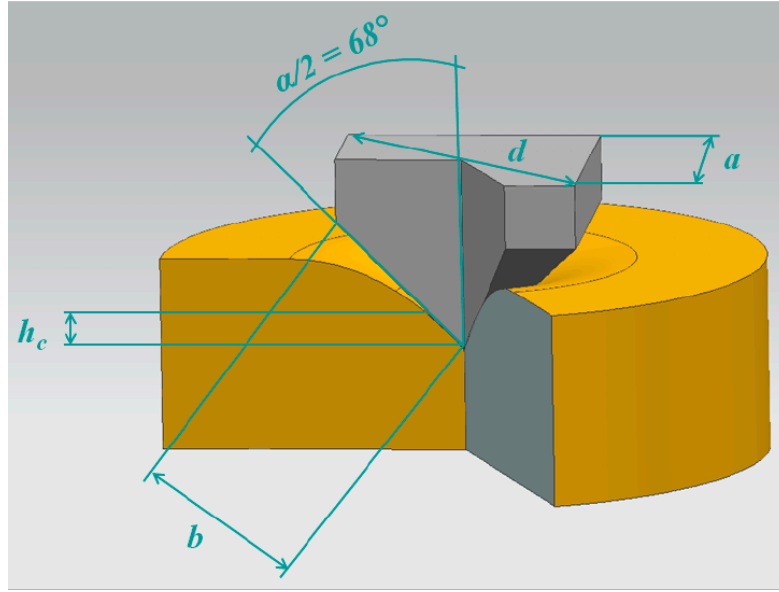


Figure 13 Schematic of the contact between a Vickers indenter and a flat sample. From [57].

$$A_p = \frac{d^2}{2} = a^2 = \left(2 \cdot h \cdot \tan \frac{\alpha}{2}\right)^2 \approx 24.5 \cdot h^2$$

Equation 1 Contact area equation for a Vickers indenter.

$$A_s = 4 \frac{a \cdot b}{2} = 4 \frac{a \cdot \frac{a}{2 \sin\left(\frac{\alpha}{2}\right)}}{2} = \frac{a^2}{\sin\left(\frac{\alpha}{2}\right)} = \frac{\left[2h \tan\left(\frac{\alpha}{2}\right)\right]^2}{\sin\left(\frac{\alpha}{2}\right)} = \frac{d^2}{2 \sin\left(\frac{\alpha}{2}\right)} \approx 26.43 \cdot h^2$$

Equation 2 Superficial area equation for a Vickers indenter.

where  $d$  is the mean diagonal of the indentation,  $\alpha$  is the Apex angle of the Vickers indenter,  $h$  is equal to  $h_c$  if the previous formulae are used to characterize the shape of the indentation when the load is still applied. In IIT the contact area  $A_c$  is tightly related to the contact depth

$h_c$  and hence to the fact that, after the withdrawal of the indenter, the change in the indentation depth due to the elastic recovery may be not negligible, unlike what happens with Brinell and Vickers hardness tests. ISO 14577 [75] establishes the method for subtracting the elastic contribution to the total displacement, thus obtaining the plastic displacements involved in the hardness definition. The cross section of the residual indentation provided in [Figure 14] outlines this feature, introducing the physical meaning of the main displacement parameters:

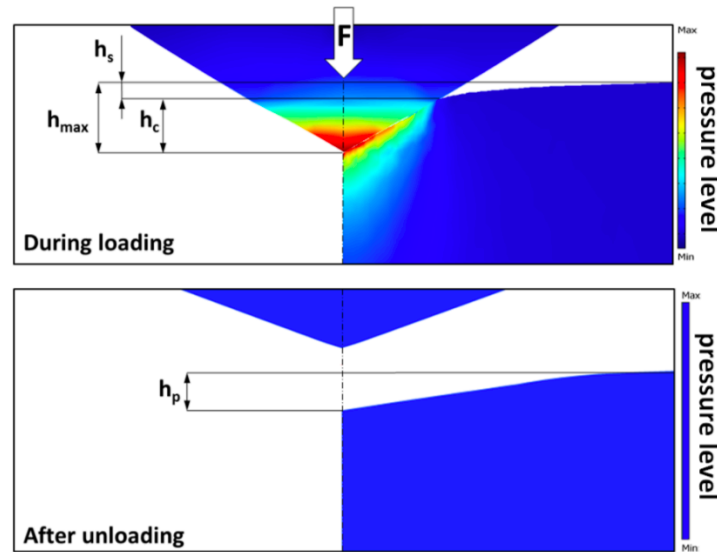


Figure 14 Cross section of an elasto-plastic indentation.  $h_s$  is the displacement of the surface at the perimeter of the contact in case of sink in [67]. From [57].

Many relevant indentation parameters can be evaluated by IIT in addition to those showed in Figure 14, these are: indentation hardness  $H_{IT}$ , Martens hardness  $HM$ , indentation modulus  $E_{it}$ , indentation creep  $CIT$ , indentation relaxation  $RIT$ , elastic and plastic contributions of the total indentation work” [57].

“IIT allows the definition of different kind of hardness. In particular, Martens hardness is measured under the applied test force (thus including the elastic and the plastic deformations), during the loading portion of the IC and preferably at the maximum load [73].

It is defined as the test force  $F$  divided by the superficial area  $A_s$ :

$$HM = \frac{F}{A_s}$$

Equation 3

Analogously to HM, also the indentation hardness  $H_{IT}$  is calculated as a mean contact pressure when the tested material is still under load [76], but with respect to the contact area  $A_c$ :

$$H_{IT} = \frac{F_{\max}}{A_c}$$

*Equation 4*

$H_{IT}$  is thus defined in agreement with the principle proposed by Meyer. ISO 14577 exploits indentation hardness to define also an equivalent Vickers hardness [73]:

$$HV_{eq} = K \frac{A_p}{A_s} H_{IT}$$

*Equation 5*

where  $K$  is the conversion factor from kgf to N. Explaining the factors it become:

$$HV_{eq} = 0,0945 H_{IT}$$

*Equation 6*

Nevertheless, ISO 14577 suggests that  $HV_{eq}$  should not be used as a substitute for HV. Young's modulus is one of the most important parameters evaluated by instrumented indentation test and used to verify the IIT performance [77]. For the specific measurement of the Young's modulus, many methods are currently available (e.g. tensile test, impulse excitation of vibration [78], atomic force microscopy) but they all show some practical drawbacks related to sample cost preparation, geometrical critical sizes or poor extraction of the elastic properties. The indentation modulus  $E_{IT}$  measured by IIT is a quite close estimate of Young modulus [79]. ISO 14577-1 describes the method to extract Young modulus from the elastic displacements through the analysis of the unloading ICs. The use of the unloading portion of the indentation curves is justified assuming that a purely elastic recovery is produced when an indenter is withdrawn, at least at the beginning of the unloading (i.e. at the maximum indentation depth)." [57].

"Several researches have tried to implement Sneddon's solution [59] about his elastic contact model ( [80] [81] [82] ). "Doerner and Nix [81] evaluated the contact depth by fitting the first one third of the unloading curves by a straight line. The resulting line is tangent to the unloading curve and its intercept locates the contact depth  $h_c$  by definition:

$$h_c = h_{\max} - \frac{F_{\max}}{S}$$

Equation 7

The contact depth is in fact evaluated considering that the distance  $h_s$  between the surface of the material and the limit of contact zone depends on sinking-in (see Figure 14):

$$h_c = h_{\max} - h_s$$

Equation 8

In particular, reminding Sneddon's solution [59] for the deflection of an elastic surface at the contact perimeter, Pharr et al. [76] showed that:

$$h_s = \varepsilon \frac{F_{\max}}{S}$$

Equation 9

where  $\varepsilon$  is equal to

$$\varepsilon = m \frac{h_s}{h_{\max}}$$

Equation 10

The so called epsilon factor depends on the indenter geometry. So, it is obtained:

$$h_c = h_{\max} - \varepsilon \frac{F_{\max}}{S}$$

Equation 11

The contact depth allows to finally estimate the projected contact area  $A_p$  by means of [Equation 1]. ISO 14577-1 describes the procedure for Eit measurement providing tabulated values for the elastic modulus  $E_i$  and the Poisson's ratio  $\nu_i$  of the indenter :

$$E_{\pi} = \frac{1 - \nu_s^2}{\frac{2\sqrt{A_p}}{S\sqrt{\pi}} - \frac{1 - \nu_i^2}{E_i}}$$

Equation 12

Where  $\nu_s$  is the Poisson's ratio of the sample,  $S$  the Elastic contact stiffness,  $A_p$  the Contact area. Differences between indentation modulus and Young's modulus may occur in case of pile up [73] or if the sample under test has anisotropic mechanical properties due to crystallographic orientation or microstructural inhomogeneity or to the presence of superficial thin films" [57].

# 5. Experimental work

## 5.1 Objectives

The evolution of the microstructure and mechanical properties of the Ti6Al4V according to different process parameters during the EBM process have been studied from many authors ([12] - [22]). Nevertheless, limited researches have been focused on exploring and making comparisons about the microstructural and mechanical properties of Ti6Al4V products realized with the two EBM process build mode: The Manual mode (MM) and Build theme mode (BTM). Furthermore, it was not found any article that used macro-indentation test on EBM products to analyze mechanical properties and make comparisons with tensile test data.

There is only one research that studied the variation of mechanical and microstructural properties with the two build modality [23]. The study [23] has the goal to investigate the microstructure and mechanical properties variations as a function of distance from the build plate for the two normal EBM build methods. Other additive manufactured Ti-6Al-4V studies used only one of the two build methods ([12] - [25], [50]etc.).

With this purpose, an overall review of the two process mode were conducted here.

The main aims of the study are to give more clarity on the behavior of the EBM process with the two process mode, analyzing the quality of the products in terms of mechanical and microstructural properties. The goal is to understand whether is better to use an automatic or manual process mode, based on the results obtained from the microstructure and mechanical properties. Results and studies have been carried out regarding the variation of the microstructure according to the distance from the build plate. These results were compared for the two process modalities and with those obtained in the article [23]. The macro-instrumented indentation tests were performed and comparisons with the tensile tests were made to verify the reliability of the results. Finally, a simplified analytical model was developed on MatLab® to predict the distribution of temperature on the surface of the powder, considering the sintering and melting phases.

## 5.2 Manual mode (MM) vs. Build theme mode (BTM)

As is reported in ([23], [24])“ The ‘standard’ Arcam build theme mode (BTM) for Ti-6Al-4V varies electron beam parameters in a controlled sequence throughout the build according to algorithms developed by the manufacturer in an effort to achieve fully dense as-built parts with consistent microstructure and properties. This process modality require the definition of the ‘speed factor’. Speed factor is a manufacturer-specific variable that describes the more generic electron beam parameters such as beam current and beam speed as they relate to a given manufacturer-specific build theme. Therefore, specific values of beam current and beam speed cannot be known from the speed factor because they are constantly being varied by the build theme throughout the build. One of the algorithms of this build mode adjusts beam speed or manage the beam current near the edge of a part to prevent overheating. To understand the benefit of this algorithm, it is necessary to describe the path of the beam during melting [Figure 15]. The beam scans in one direction for each layer (either the x- or y-direction), and this direction alternates for each subsequent layer. The beam scans across all parts on a given line before turning around and scanning along the adjacent line. With this electron beam path, the heat will be greater near the edge of a part where the beam turns around and might lead to undesirable effects such as porosity from overheating or inconsistent micro- structure and mechanical properties (hot-spot phenomenon)”.

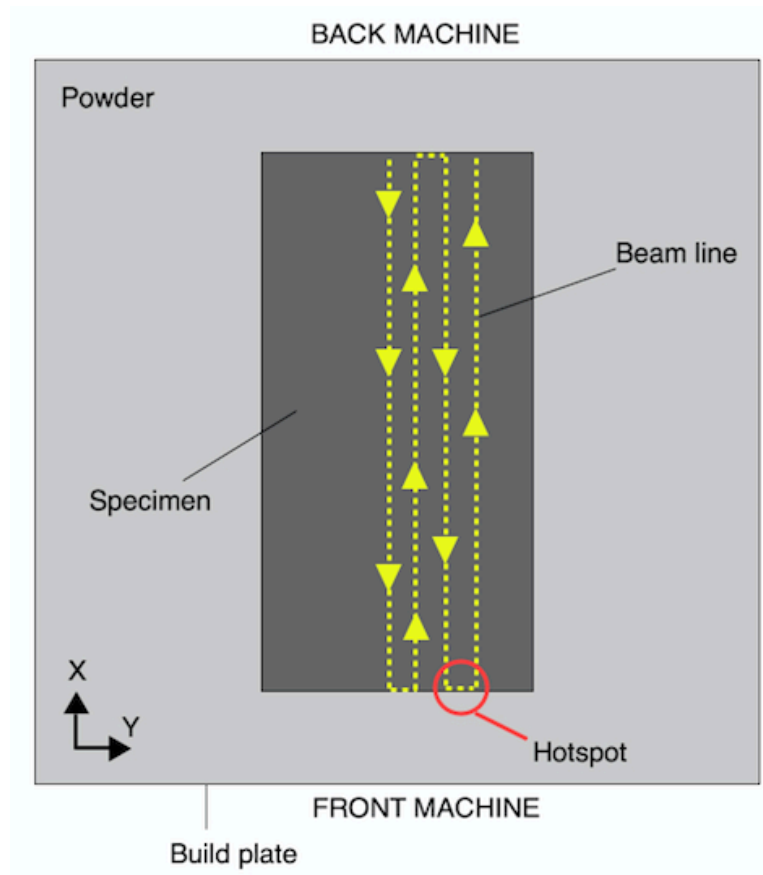


Figure 15 Top schematic view of the beam scan.

The standard Arcam build theme for Ti-6Al-4V increases beam speed or manage beam current as the beam approaches a turnaround point in an effort to achieve fully dense parts and consistent microstructure. This function is one of the several control algorithms included in the build theme mode. Although this modality seems to have great advantages, it also has some disadvantages:

- 1) Specific values of beam current and beam speed cannot be known from the speed factor, then would be difficult perform simulations to predict the process and material behavior.
- 2) A wrong choice of the current limits range can cause bad results in terms of porosity, swelling and deformations.

The manual mode is characterized by the use of a steady beam speed and beam current values. Unlike the previous method, it could lead to more problems due to the hot spot phenomenon because the static parameters. However, a correct selection of the process parameters could lead to very good results, even better than the previous case. Moreover, the predicting of the temperature generated on the powder surface, using software simulations, would be easier having constant parameters. Generally, this method is used to

build fine lattice structures and it is rarely used for the realization of bulk parts [23]. In this study, the consequences that the static parameters had on the bulk material were analyzed and discussed, and comparisons in terms of microstructure and mechanical properties with the BTM were carried out.

## 5.3 Methods

### 5.3.1 Parameters utilized

- The Ti-6Al-4V powder with a nominal particle size distribution of 45 - 105  $\mu\text{m}$  supplied by Arcam AB was used in this work. The analysis of the unfused powder was provided by the University of Rostock, Fluid Technology and Microfluidics, where the work was carried out [Figure 16, Figure 17]. All the powder involved in the process was subjected to several recovery cycles in the PRS (powder recovery system), so the oxygen content within the material was slightly higher than that of virgin material ([83], [84]).

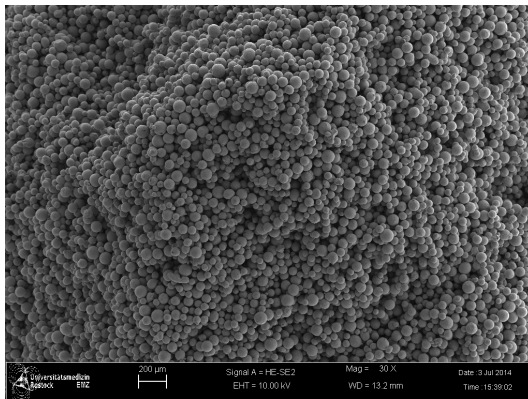


Figure 16 SEM image provided by Universität Rostock.

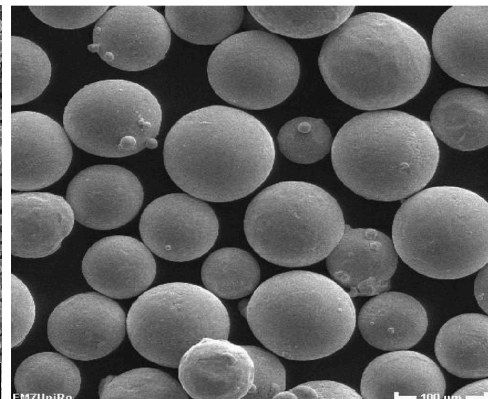


Figure 17 Un-melted Ti-6Al-4V powder. 100x Magnification. From [82].

- A 10 mm-thick stainless steel start plate was used. This plate was heated by the electron beam under a vacuum of  $5\text{e-}4$  mBar.
- The start plate temperature was  $730^\circ\text{C}$ .
- The powder layer thickness was  $50 \mu\text{m}$ .
- All the process was kept under a controlled vacuum in the temperature range of  $600\text{--}650^\circ\text{C}$ .
- Entire the building process was kept under a vacuum of  $2 * 10^{-3}$  mBar and an acceleration voltage of 60 kV.
- The process was controlled by using high-purity helium to prevent powder charging.

## 5.3.2 Work Procedure

At the beginning of the work a specify procedure was established to analyze the differences between the two process modalities and to evaluate the variations of the properties as the process parameters changed. The procedure followed is that shown in the [Figure 18].

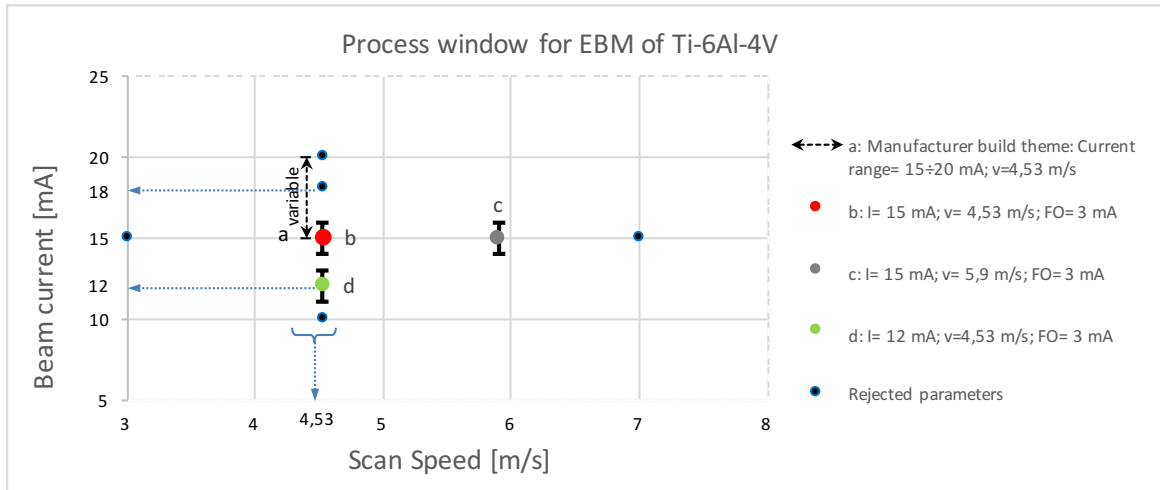


Figure 18 Process window for EBM of Ti-6Al-4V. Black points represents the samples that were rejected because marked defects. Sample 'a' (obtained with the BTM). Samples 'b', 'c' and 'd' are obtained with the MM.

Initially, specimens were built using the "standard" Arcam build theme mode (BTM) represented in [Figure 18] by the dotted black line (sample a). In this mode the current value is controlled by some algorithms developed by the manufacturer and takes on values between two limits set by the user, in this case between 15 and 20 mA. Regarding the beam speed, a value of 4,53 m / s was set, although this value varies slightly according to the pre-set algorithms in the machine and reaches values that cannot be known beforehand. The choice of current and speed variation limits was made on studies previously performed on the same machine. ([84], [83]).

After that, it was decided to make samples in manual mode (MM). In this mode the "speed factor" and static values of speed and current were used. Eight tests were performed in total, each of which uses a different pair of process parameters. The first set of steady parameters were marked with letter 'b' [Figure 18], where a current of  $I = 15$  mA and beam speed of  $v = 4.53$  m / s were set. These starting parameters were chosen referring to the BTM mode, maintaining a constant value of beam current and speed throughout the

process. Starting from this initial configuration, it was decided to make other specimens maintaining a constant speed equal to  $v = 4.53 \text{ m / s}$  and assuming constant current values, but different from the initial configuration, of  $I = 10 \text{ mA}$ ,  $I = 12 \text{ mA}$ ,  $I = 18 \text{ mA}$ ,  $I = 20 \text{ mA}$ . The same but reverse reasoning was followed with other samples, keeping a constant current value equal to  $I = 15 \text{ mA}$  and assuming constant speed values of  $v = 3 \text{ m / s}$ ,  $v = 4.53 \text{ m / s}$ ,  $v = 5.9 \text{ m / s}$ ,  $v = 7 \text{ m / s}$ . The points highlighted in black in [Figure 18] are those referred to the rejected samples, due to the presence of pronounced defects like swelling, deformations and inappropriate shapes. The colored points a, b, c, d are the set of process parameters that gave specimens with less visual defects, and they are also the samples analyzed in this thesis.

Once this initial phase was defined, the results were analyzed and discussed as follow.

## 5.4 Specimens

### 5.4.1 Procedure

Once the Cad files of the specimens were created, they have been loaded onto the Magics software. This software was mainly used for fixing the part and creating supports if they were necessary.

The reason for using supports are:

- 1) To prevent over heating at areas where the z-thickness is small.
- 2) The samples, even more if they are very small, undergo a very fast cooling, causing shrinkage by deformations that tend to drag the layers previously deposited. If the supports had not been provided, the final product would not have been completely deformed and would not have met the required specifications. The supports create a connection between the build plate and the samples and compensates the deformations due to the shrinkage. Obviously, an incorrect choice of the process parameters could lead to the detachment of the supports from the built plate, giving equally defects of shrinkage.
- 3) Process stability. If the products had been made directly on the powder bed, there would have been instabilities due to vibrations, rake movements, fluid dynamic turbulence.

The first steps of the EBM process are the less stable, because the cleaning of the machine, the geometric and dimensional tolerances of the construction plate, the centering and alignment of the build plate, are manual operations performed by the user, so they are affected by errors. To make a stable support step process, it is necessary to ensure a build plate with flat surfaces, parallel to the machine plane, smooth, polished and free of powder granules. Each of these measures are essential to ensure a fair and homogeneous deposition of the first layers of material on which the supports will be built.

A moderate degree of over heating will lead to icicle formation on down facing surfaces, whereas a more pronounced over heating may lead to an additional geometry deformation in terms of swelling and curling.

There are two different kinds of supports used in the EBM process, namely volume and wafer supports.

Volume supports: have a bulky and box like geometry. In the EBM process they are sintered only and can be easily removed in the subsequent powder recovery process.

Wafer supports: They complement volume supports by preventing swelling and curling. These supports are created within the Support Generation Module in Magics. Wafer supports consists of Line, Block and Contour elements which form solid supports in point wise contact with the supported area, enabling easy removal.

In this work, 5 mm high wafer supports were provided. Three tensile test specimens and three microstructure inspection specimens were made for each pair of parameters. The specimens have been positioned in the central area of the construction volume to avoid problems of instability of the electron beam. Figure [incollare figure] shows the STL file of the specimens exported from Magics. The procedure used on the software was the same reported in the article [85]: “The STL file was sliced into a 2D compressed layer file (ABF file) with a thickness of 0.05 mm using the EBM Build Assembler software. Only the ABF file can be imported into the embedded EBM Control software for additive manufacturing in the Arcam A1 machine. It is noted that each prepared build file should be simulated by using EBM Control before starting a job. EBM Control simulation could indicate the approximate build time”. To better understand the dimensions of the manufactured specimens, the technical drawing are shown below [Figure 19 ]. The drawing is not in scale and the units are in mm.

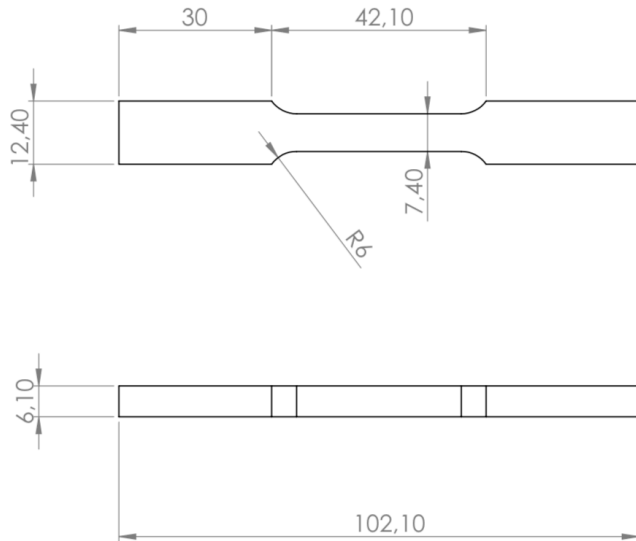


Figure 19 Tensile test specimen made with EBM. Dimensions according to ASTM E8 / E8M – 09.

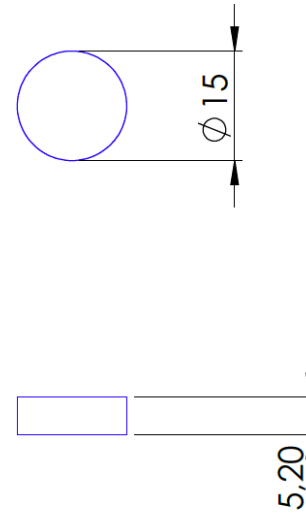
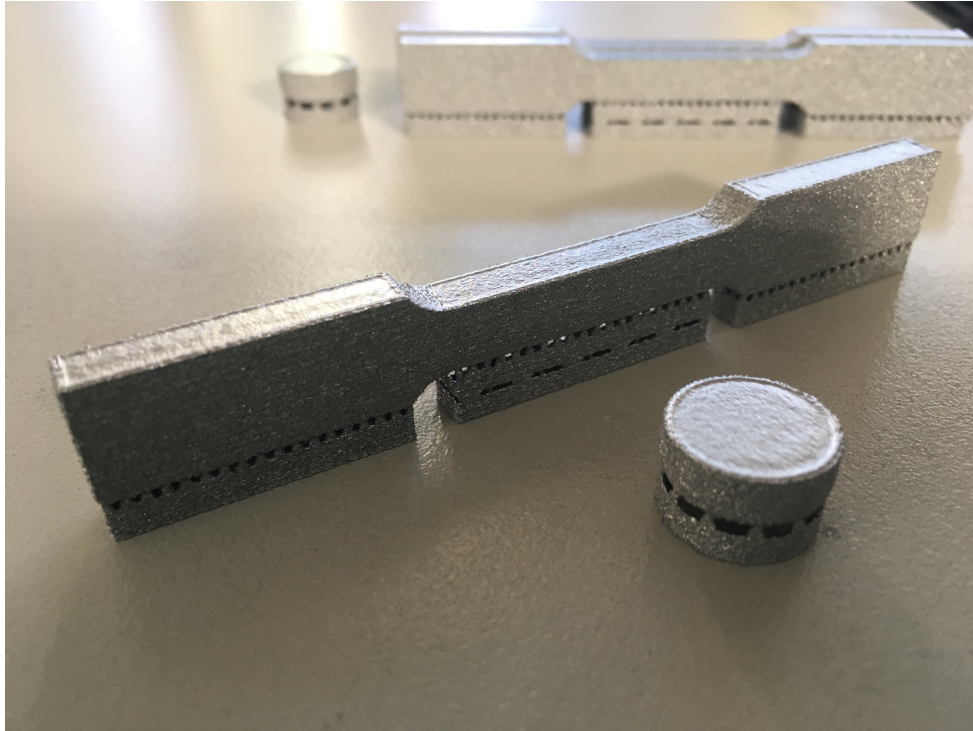


Figure 20 Specimen for microstructural analysis.

The tensile specimens were provided of additional material so that, after the machining process (ASTM E 466 - 96), it was possible to obtain unified dimensions valid for the tensile test.

The specimens for microstructural analysis had a cylindrical shape. The choice of this form rather than the rectangular one is due to evaluate the deformations generated by the process on non-rectilinear edges. Strains on straight edges were analyzed on tensile specimens. About the microstructural analysis, the specimens were machined to obtain two flat, parallel and perpendicular faces to the supporting build plane. After having polished the two faces until reaching a mirror surface, it was possible to evaluate the microstructure and the macro instrumented indentation tests as the distance from the build plate changed.

An example of the specimens built during the process are shown in the [Figure 21].



*Figure 21 Specimens cleaned in the PRS system.*

## 5.4.2 Results and comparisons

Before analyzing the specimens obtained with different process parameters, it has to be pointed out that in the "standard" process mode (BTM), the tensile specimen was not built because the mechanical results were already been studied from the research group of the Fluid Technology and Microfluidics, University of Rostock. For this reason, only the experimental results of the tensile test were reported.

Referring to [Figure 18], the completed parts are shown below.

- **Samples a:**



*Figure 22 Sample "a" after removing supports..*

The specimen had clear deformations both on the lower part and on the upper part. When the specimens were cleaned in the PRS, the supports were perfectly attached to the surface of the build plate. These deformations may be due to a non-optimal choice of the parameters (limits of the variability range of current and speed) for which too high temperatures was generated causing over-heating and deformations by shrinkage. It must be said that, compared to the work [83], the type of supports were different, so it is likely that this factor also affects the results obtained.

- **Samples b:**

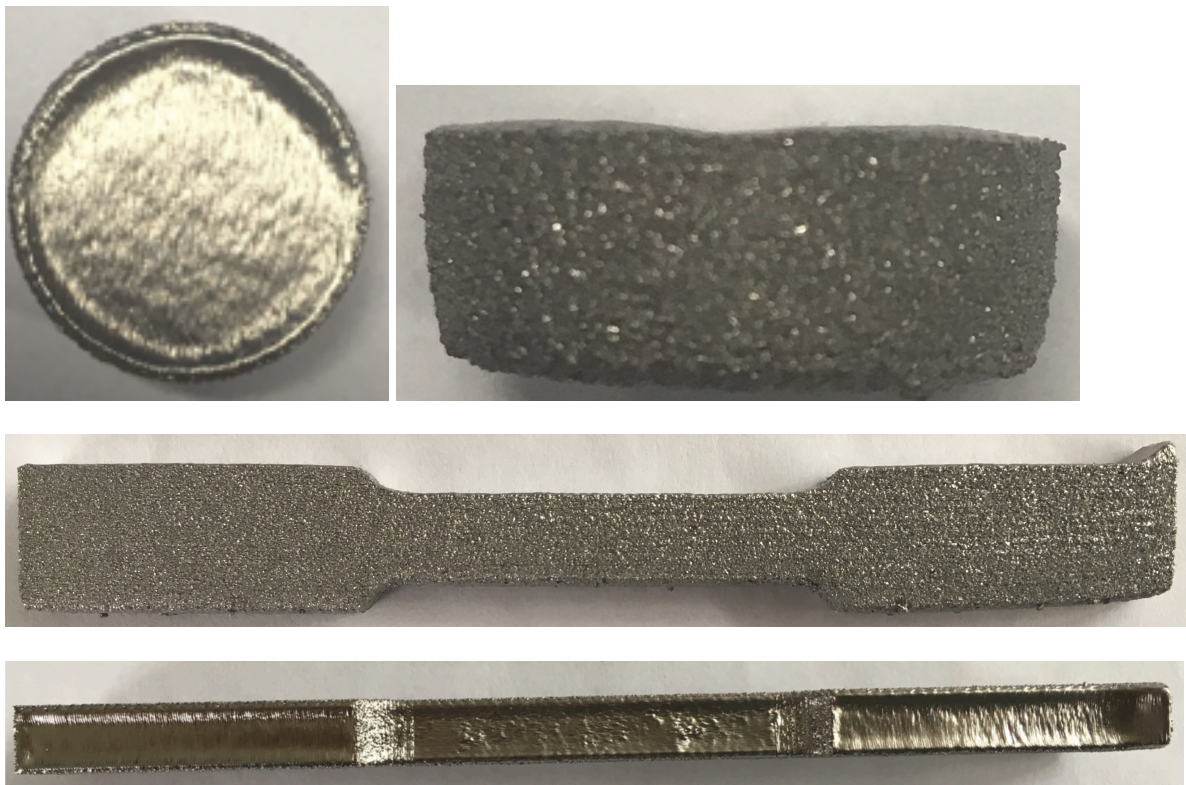


*Figure 23 Samples "b" after removing supports.*

Remarkable deformations of the material could be noted. This may be due to several aspects:

The combination of current and speed causes very high temperatures that leads to high deformations of the material during the cooling step. The right part of the tensile specimen was more deformed than the left side and when the samples were removed from the build plate, the supports were not well attached to the build plate. Also in this case, there was a very likelihood that high temperatures were reached causing a very pronounced shrinkage with consequent detachment of the supports. It should be noted that compared to the

previous case, a fixed current value and a fixed speed value were used, therefore the problem due to the hot-spot was amplified.

- **Samples c:**

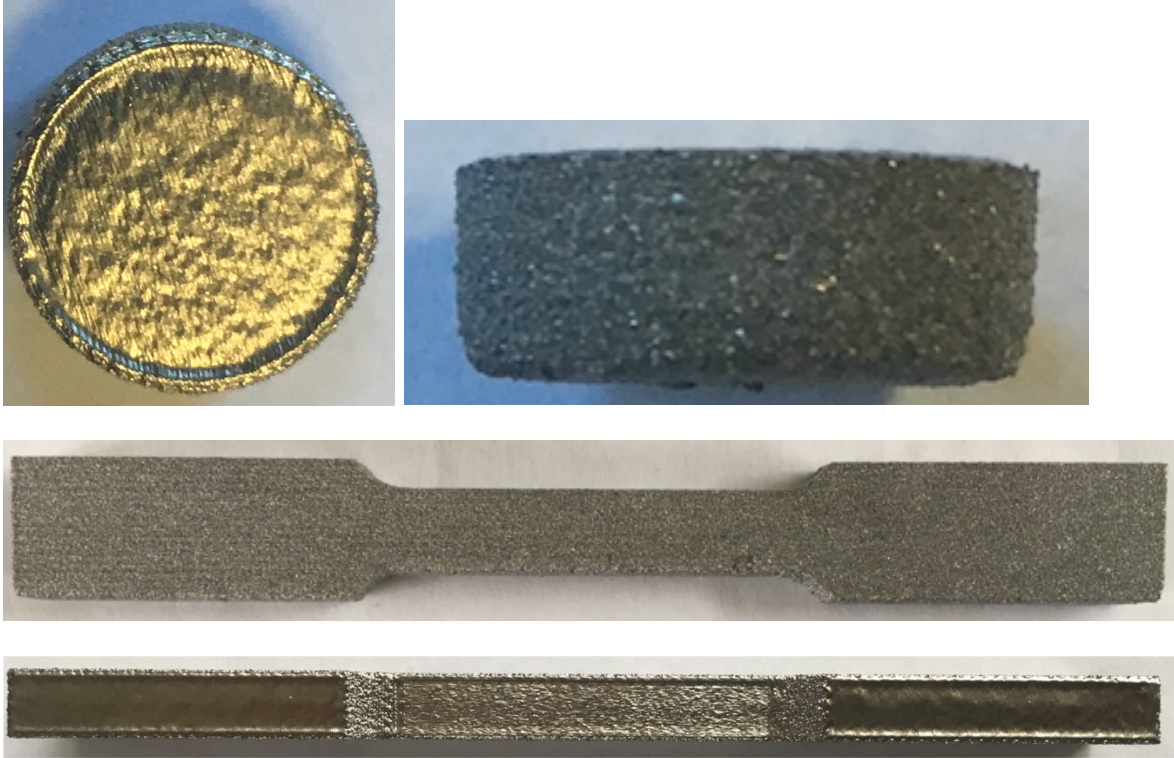


*Figure 24 Samples "c" after removing supports.*

In this case, from the point of view of form and geometry, there were considerable improvements. The cylinders had a slight deformation on the upper edge, while the tensile specimens seemed to comply with the required specifications.

- **Samples d:**

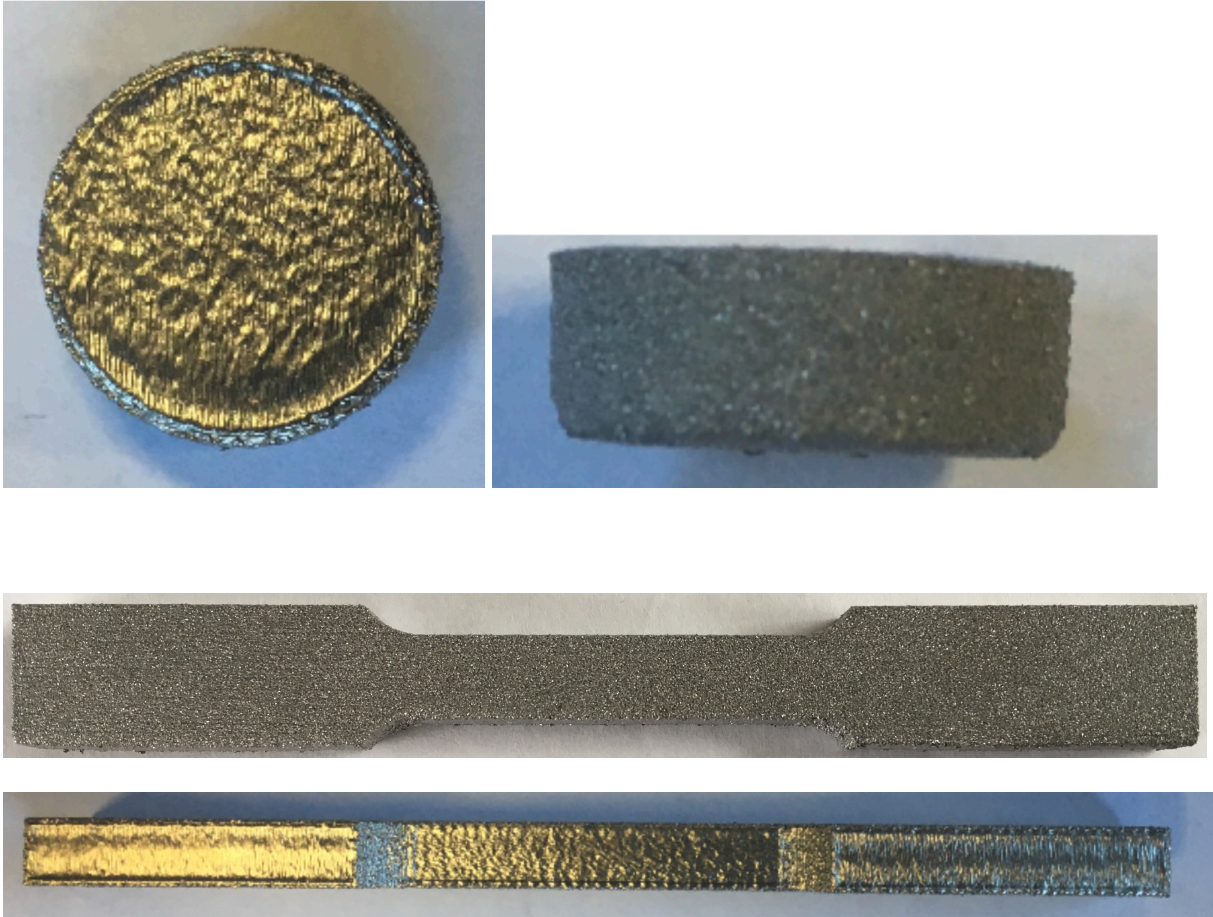


*Figure 25 Samples "d" after removing supports.*

These specimens appeared to have less aesthetic deformations than the others. The edges of the specimens were clearer and the dimensions respected the required tolerances.

All the specimens represented in [Figure 18] with black circles, were not considered in this analysis because they showed much more defects (deformations or porosity) than those just analyzed.

## 5.5 Porosity and density

### 5.5.1 Procedure

It is necessary to mention again the reference system adopted. The Z axis represents the build direction, so the ZX plane is the build plane and the XY plane is that perpendicular to the construction plane. The analysis of the porosity and density was carried out on the machined cylindrical specimens. Each specimen was cut on two sides so as to identify two flat faces parallel to the Z axis [Figure 26]. To analyze the porosity and the microstructure, the surface was polished with 1  $\mu\text{m}$  diamond paste.

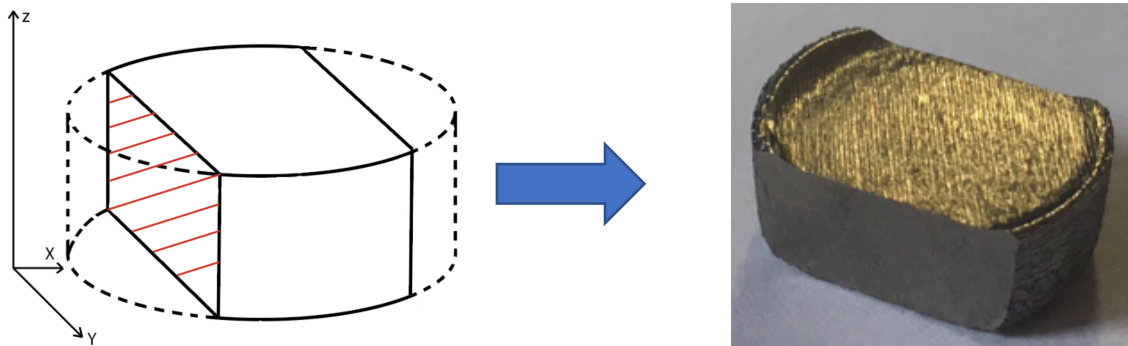


*Figure 26 Cylindrical machined specimen. The dashed volume represents the removed material.*

First of all, the sections of each specimen were analyzed using an electron microscope with a magnification of 25x in DIC mode. The studied section is that one represented with the letter 'A' in [Figure 27]. The area of the section 'A' is identified by the microscope lens, and measure 30 mm <sup>2</sup> taking the whole width 'b' of the specimen [Figure 27].

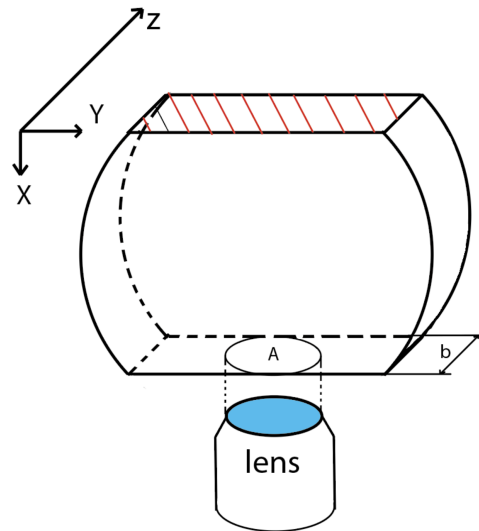


Figure 27 Representation of the section analyzed.

## 5.5.2 Results and comparisons

In This study, only the near-spherical pores after polishing [Figure 28 - Figure 31] were analyzed. Their presence of the pores is attributed to the Argon gas trapped during the gas-atomized titanium alloy powder [49]. The non-fusion defects, e.g. unmelted powder and layer gaps, as revealed in [Figure 34 - Figure 37] were also seen, but they were neglected because they are due to inconsistent raking or a non-optimised melting process parameter.

The following images [Figure 28 - Figure 31] show the sections 'A' at a magnification of 25x in DIC mode. The lower part of each image corresponds to the closest zone to the build plate, the upper part corresponds to the last deposited layers. Subsequently, a more accurate analysis of the sections was performed, observing the number of pores, in the same area, at a magnification of 200x in DIC mode. The following measurement were done at 200x magnification.

It is important to note that, the analyzed sections represent a part of the infinite sections present in the workpiece volume, therefore, this inspection has not to be considered as a reliable methodology to measure the porosity. For this reason, density measurements were carried out through the Archimedes' principle, to guarantee the effective pore value throughout the workpiece volume [Figure 33].

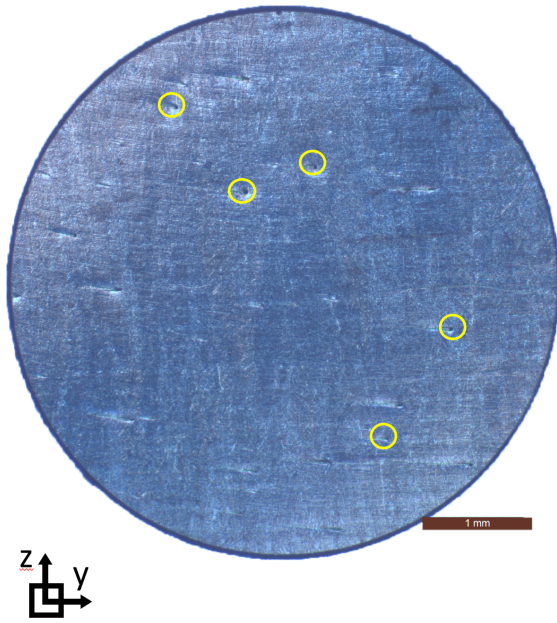


Figure 28 Sample "a":  $I = 15 \pm 20 \text{ mA}$ ,  $v = 4,53 \text{ m/s}$

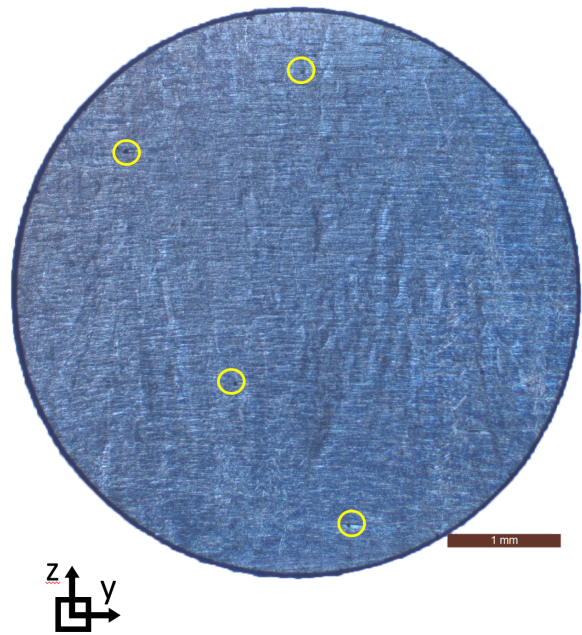


Figure 29 Sample "b":  $I = 15 \text{ mA}$ ;  $v = 5,9 \text{ m/s}$ ;  $FO = 3 \text{ mA}$

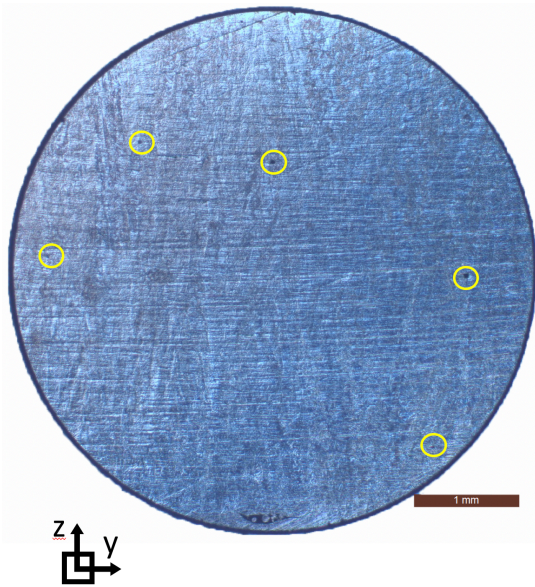


Figure 30 Sample "c"  $I = 15 \text{ mA}$ ;  $v = 5,9 \text{ m/s}$

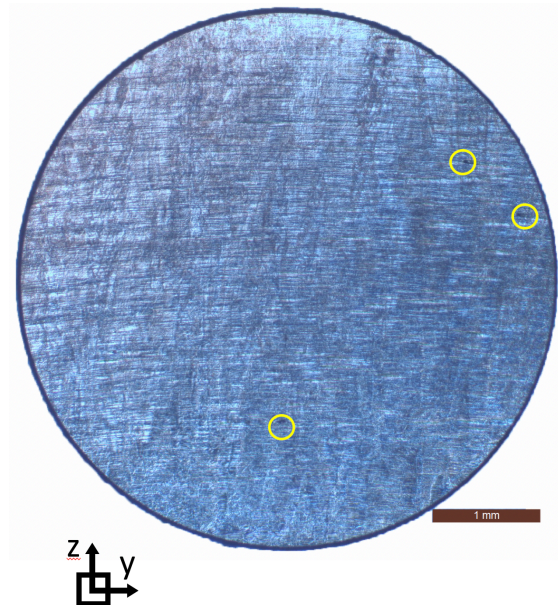


Figure 31 Sample "d"  $I = 12 \text{ mA}$ ;  $v = 4,53 \text{ m/s}$

The specimen 'a' has many non-fused areas [Figure 34 - Figure 36], that were not highlighted in the [Figure 28]. The number of pores is among the highest identified compared to other samples and have sizes ranging from a minimum of  $15 \mu\text{m}$  to a maximum of  $37 \mu\text{m}$  [Figure 32].

The specimen 'b' has the highest number of pores compared to other specimens analyzed at 200x magnification, but they have very small dimensions ranging between a minimum of 11  $\mu\text{m}$  and a maximum of 29  $\mu\text{m}$  [Figure 32].

The specimen 'c' has a smaller number of pores than the specimen 'a' and 'b', with sizes ranging between 12  $\mu\text{m}$  and 44  $\mu\text{m}$  [Figure 32], but showed some areas in which the layers were not fused together [Figure 37].

The specimen 'd' has the minimum number of pores, with dimensions ranging between 18  $\mu\text{m}$  and 34  $\mu\text{m}$  [Figure 32].

The following diagram [Figure 32] represents the number of pores detected in an area of 30  $\text{mm}^2$ , with its average size and standard deviation.

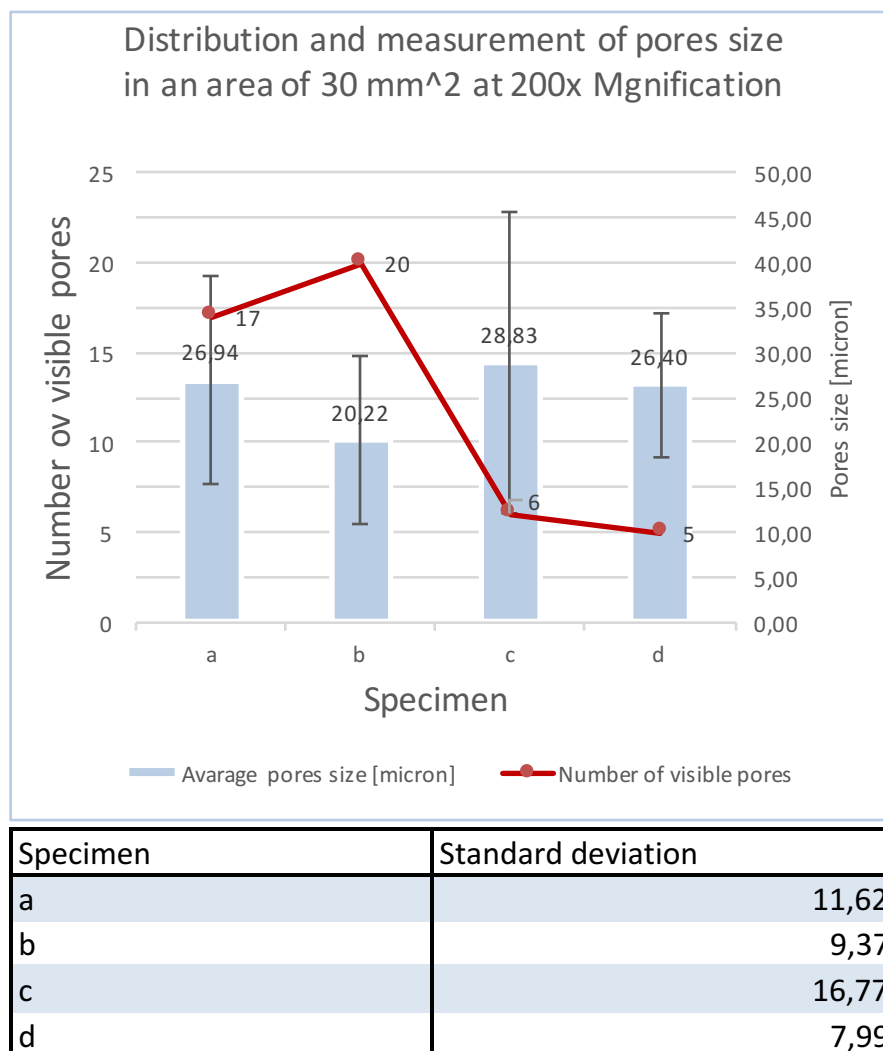


Figure 32 Measurement of the number of pores and pores size detected in an area of 30  $\text{mm}^2$  at 200x magnification.

In the [Figure 33], the density measurement with the Archimedes' principle is reported.

It can be noted that the density remains almost constant at  $4.39 \frac{g}{cm^3}$  for all the specimens, about 1% lower than the ideal one ( $4.43 \frac{g}{cm^3}$ ). The density and porosity values can be observed in [Figure 33]. This indicates that the presence of pores does not generate an exaggerated reduction of the weight of the specimens, moreover the documents ([57], [86], [87]) say that the pores can be easily eliminated with the HIP process (Hot isostatic pressing).

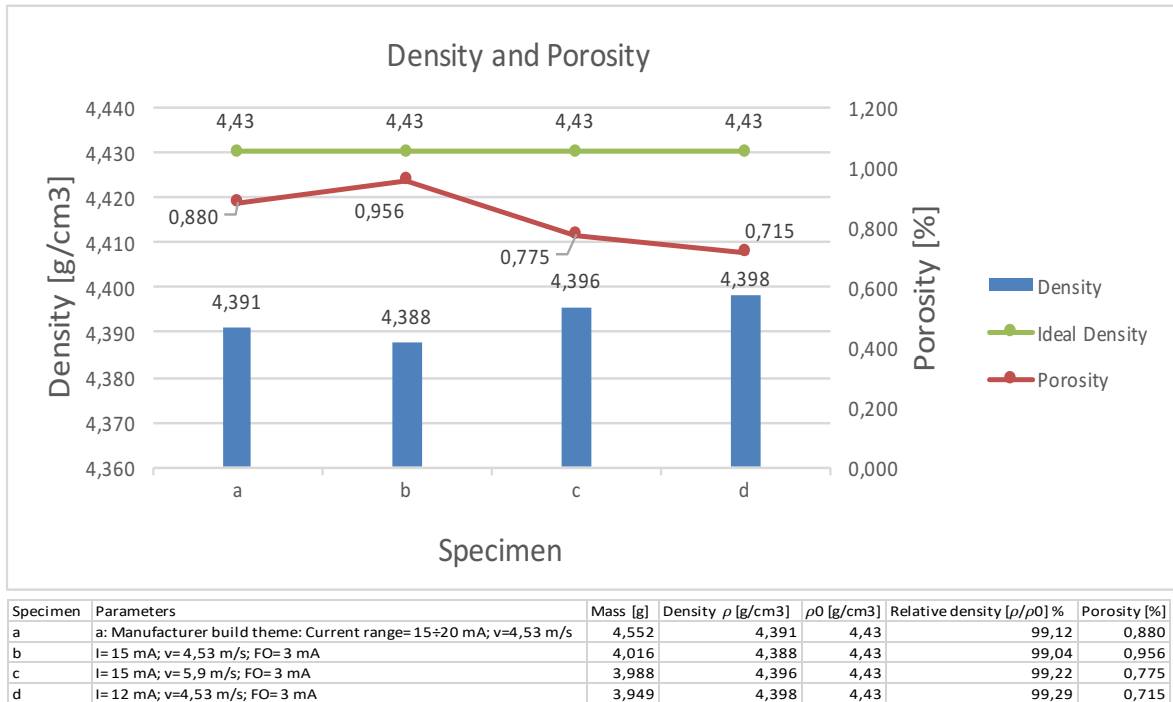


Figure 33 Density and porosity values measured with the Archimedes' principle.

The following images [Figure 34 - Figure 37] show some defects found in the specimens. These lack of fusion layers were identified on the whole height of the samples, mostly in the lower part. The defects size ranges from 100  $\mu\text{m}$  up to more than 500  $\mu\text{m}$ . The [Figure 34 - Figure 36] refer to the sample 'a', while the [Figure 37] refers to the sample 'c' and showed non-fused areas exclusively in the first deposited layers. All other samples did not showed any such defects.



Figure 34 Unmelted zones at the bottom part of the sample "a"

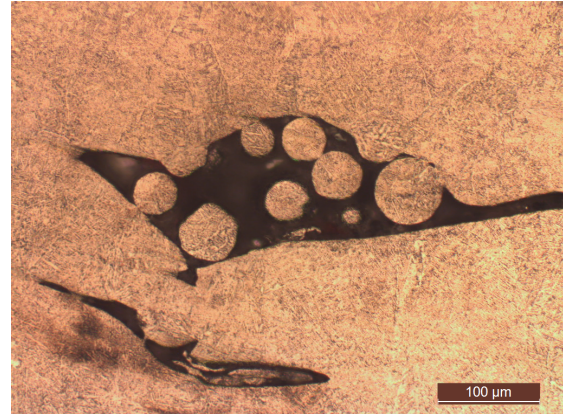


Figure 35 Unmelted zones at the bottom part of the sample "a"

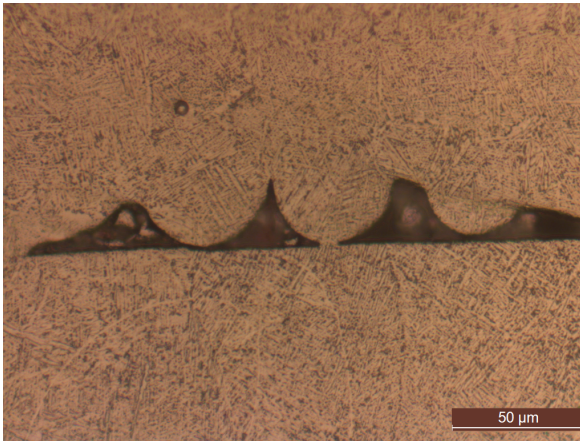


Figure 36 Unmelted zones at the core part of the sample "a"

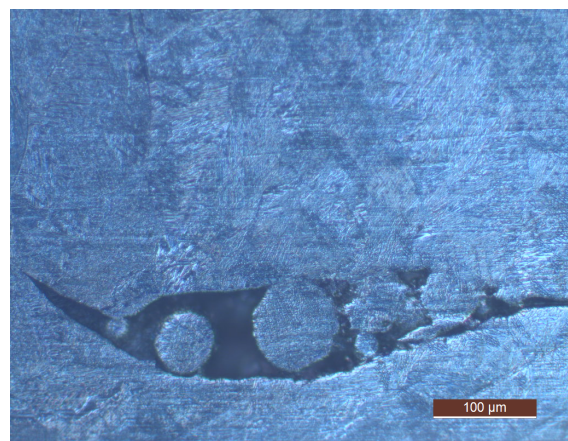


Figure 37 Unmelted zones at the bottom part of the sample "c"

## 5.6 Microstructure analysis

### 5.6.1 Procedure

As mentioned in the previous chapter, the samples were polished until reaching a mirror surface with 1  $\mu\text{m}$  diamond paste and etched out by Kroll's reagent.

The adopted procedure involves the analysis of the specimens in 3 specific areas: TOP, CORE and BOTTOM zones. This subdivision was necessary both to analyze the different microstructures when the distance from the build plate changed and to compare the results of the macro instrumented indentation tests.

Starting from the stitch images that affects the entire height of the samples [Figure 38 - Figure 41] the three areas were analyzed individually [Results and comparisons, 5.6.2 ]. The lower part of each image corresponds to the closest zone to the build plate, the upper part corresponds to the last deposited layers.

Making a quick preliminary analysis, it was noted a predominantly columnar structure in all the samples, parallel to the build direction. This means that the heat dispersion took place along the build direction. The sample 'a' showed much more defects than others, especially at the lower part. The melted layers of the sample 'a' are more evident than the others and the marks that the sample 'd' showed were due to the Kroll's reagent. The two cyan lines divide the height of the specimen into 3 zones, which are studied in the following paragraph.



TOP

CORE

BOTTOM

Figure 38 Sample "a":

$I = 15 \pm 20 \text{ mA}$ ,  $v = 4,53 \text{ m/s}$

Figure 39 Sample "b":

$I = 15 \text{ mA}$ ;  $v = 4,53 \text{ m/s}$

Figure 40 Sample "c":

$I = 15 \text{ mA}$ ;  $v = 5,9 \text{ m/s}$

Figure 41 Sample "d":

$I = 12 \text{ mA}$ ;  $v = 4,53 \text{ m/s}$

## 5.6.2 Results and comparisons

- **BOTTOM PART**

The first part analyzed was the zone closest to the build plate, the "Bottom part". The images show lighter areas constituting the  $\alpha$  phase, and darker areas which surround the  $\alpha$  lamellae, constituting the  $\beta$  phase.

At the bottom of the samples there is a near-equiaxed prior  $\beta$  grain structure. These grains are those delineated by wavy and wider grain boundary  $\alpha$ . Within the prior  $\beta$  grains there is a coarse  $\alpha + \beta$  microstructure consisting of  $\alpha$  lamellar colony and widmanstätten pattern and  $\beta$  rods.

The images below [Figure 42 - Figure 46] show that the primary  $\beta$  grains have a slightly elongated shape surrounded by closed grain boundaries  $\alpha$ . During the EBM process, because the previously melted layers undergo a continuous supply of heat by the subsequent new layers, the temperature is kept at about 630°C, which allows the formation of a balanced and coarser structure than the overlying layers. Under these conditions, the heat is dispersed uniformly in all directions, giving rise to prior equiaxed  $\beta$  grains and thicker  $\alpha$  lamellae. This behavior is common for all the specimen and is in agreement with the article [50].

The sample 'a' has smaller prior  $\beta$  grain size than the other cases, with thinner and more closed contours (thickness of grain boundary  $\alpha = 2 \div 4 \mu\text{m}$ ) than the specimens made in MM. The samples 'b', 'c' and 'd' show the dimensions of grain boundaries  $\alpha$  that far exceeds the previous case (from 4 to 10  $\mu\text{m}$ ). In all the specimens analyzed, the size of the prior  $\beta$  grains is greater than the thickness of the deposited layers. The rest of the microstructure is a mix of  $\alpha$ -phase lamellae ( $\alpha$  colony or basket wave pattern) surrounded by  $\beta$  phase, as described in [50]. It can be noted that the alpha lamellae formation is almost similar to the dendritic morphology formation, in fact there is a main branch (in this case grain boundary  $\alpha$ ), from which grow side branches, from which grow smaller side branches, and so on [Figure 42 - Figure 46]. In some cases the presence of the Widmanstätten structure was found [Figure 46]

During the analysis, 10 measurements of the  $\alpha$  lamellae widths were carried out for each specimen, neglecting the width of the grain boundary  $\alpha$ . Results of the  $\alpha$  lamellae widths average size are shown in [Figure 57]. It came out that the  $\alpha$  lamellae average width was higher in the sample 'b' (about 3  $\mu\text{m}$ ) with a standard deviation of about 0.8  $\mu\text{m}$ . The lower

average width was found in the sample 'a' (just under 2  $\mu\text{m}$ ) with a standard deviation of about 0.45  $\mu\text{m}$ . The sample 'c' showed  $\alpha$  lamellae average width just over 2  $\mu\text{m}$  with a lower standard deviation than the other cases, and the sample "d" exhibited an  $\alpha$  lamellae average width little bit lower 3  $\mu\text{m}$  with a standard deviation that exceeds the previous cases (1.15  $\mu\text{m}$ ).

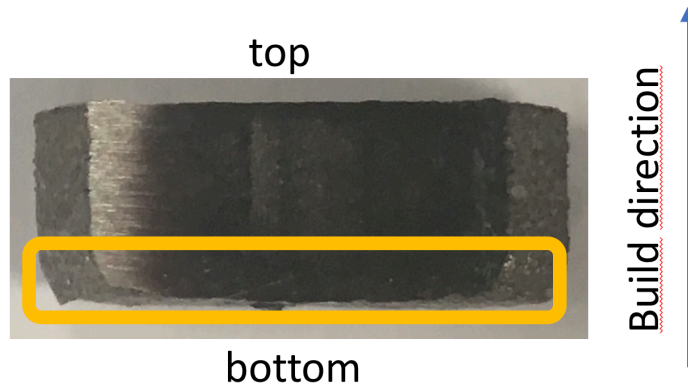


Figure 42 Macro-Scheme of the analyzed part.

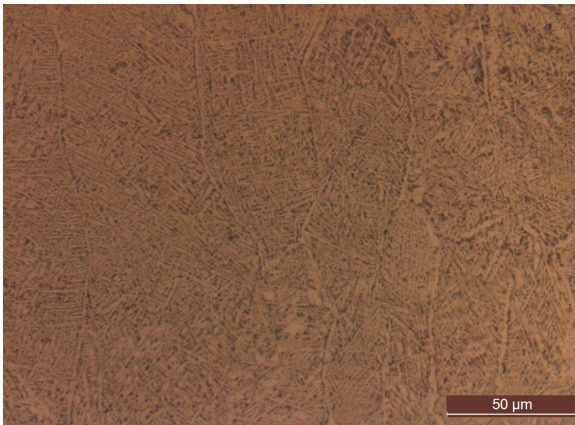


Figure 43 Sample "a":  $I= 15\div 20\text{ mA}$ ,  $v=4,53\text{ m/s}$

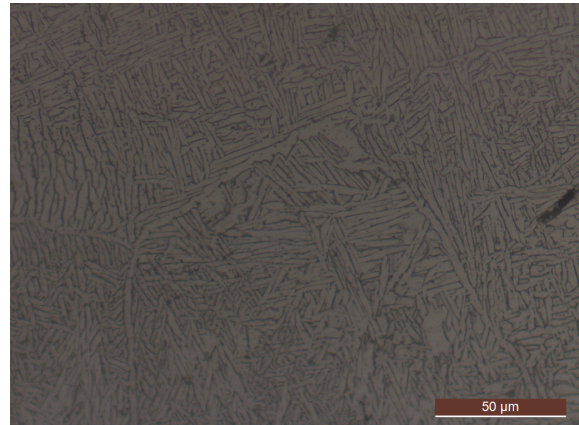


Figure 44 Sample "b":  $I= 15\text{ mA}$ ;  $v= 4,53\text{ m/s}$

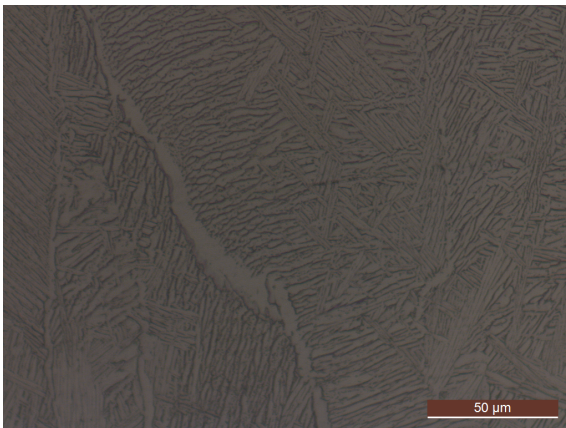


Figure 45 Sample "c":  $I= 15\text{ mA}$ ;  $v= 5,9\text{ m/s}$

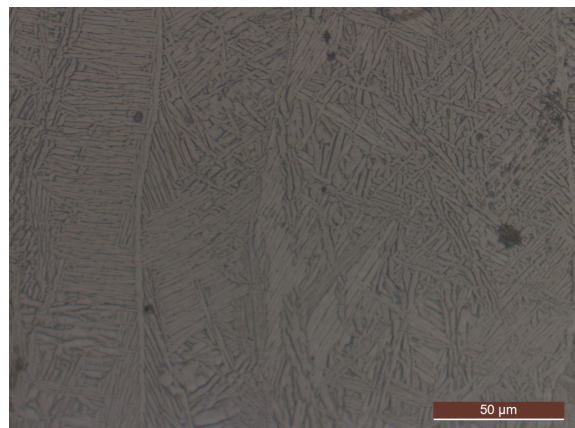


Figure 46 Sample "d":  $I= 12\text{ mA}$ ;  $v=4,53\text{ m/s}$

- **CORE PART**

The second analyzed zone is the core part. As the distance from the build plate increases, the prior  $\beta$  grains have an increasingly lengthened and less closed conformation than the previous case. This means that non-equilibrium processes of heat dissipation occurred due to variation of solidification conditions (e.g. thermal gradient and solidification rate) of melt pool. Therefore an equiaxed-to-columnar transition region for the prior  $\beta$  grains occurred due to the hindered atomic diffusion by rapid cooling.

In this central area, the specimens showed a mixed microstructure of  $\alpha$  lamellae and  $\beta$  phase with a prevalence of  $\alpha$  lamellar colony and widmanstätten pattern. Also in this case, 10 measurements were made [Figure 57] on the width of the  $\alpha$  lamellae, and it was found that on average the dimensions decreased by 20-30%.

It came out that the average size of the  $\alpha$  lamellae was higher in the sample 'b' (about 2,4  $\mu\text{m}$ ) with a standard deviation of about 0,6  $\mu\text{m}$ . The lower  $\alpha$  lamellae average width was seen in sample 'a' (just under 1.15  $\mu\text{m}$ ) with a standard deviation of about 0.35  $\mu\text{m}$ . The sample 'c' had  $\alpha$  lamellae width of about 2  $\mu\text{m}$  with a standard deviation of 0.7  $\mu\text{m}$ , and the sample 'd' exhibited an  $\alpha$  lamellae average width of about 1.3  $\mu\text{m}$  with a standard deviation of 0,33  $\mu\text{m}$ .

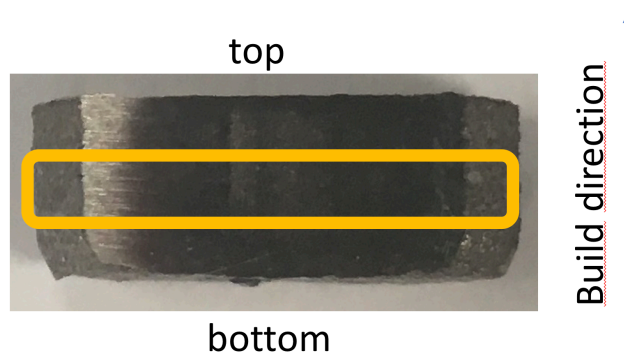


Figure 47 Macro-Scheme of the analyzed part.

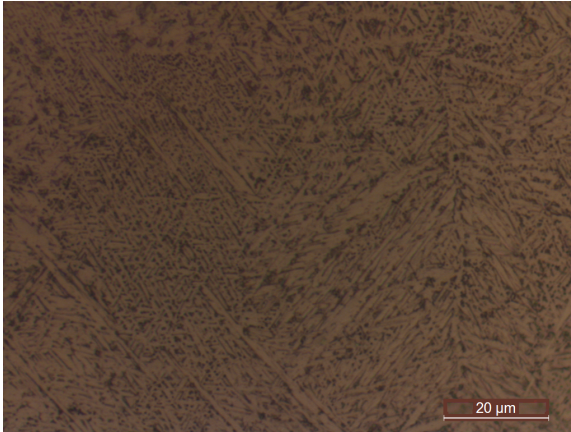


Figura 48 Sample "a":  $I= 15\div 20$  mA,  $v=4,53$  m/s

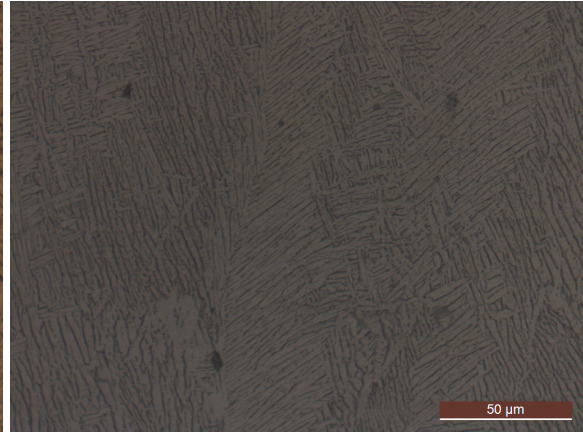


Figura 49 Sample "b":  $I= 15$  mA;  $v= 4,53$  m/s



Figura 50 Sample "c":  $I= 15$  mA;  $v= 5,9$  m/s

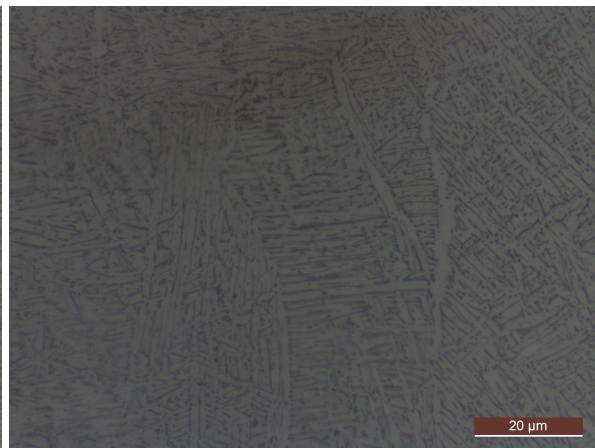


Figura 51 Sample "d":  $I= 12$  mA;  $v=4,53$  m/s

- **TOP PART**

The third analyzed zone is the upper part, related to the last deposited layers. In this area the microstructure is so fine to not distinguish the passage between two adjacent prior beta grains. The grain boundary  $\alpha$  do not have a prevalent size compared to the rest of the microstructure and the length of the  $\alpha$  lamellae results to be longer and thinner than the previous cases. The refinement of the microstructure of the last layers was due to the less accumulation of heat and less annealing time exposure, nevertheless there was not any presence of martensite.

The formation of martensitic phase is a well-discussed topic in the articles ([50], [51]). Its formation takes place by fast cooling from the liquid temperature to a temperature below the martensite start. Since the annealing temperature for the Ti-6Al-4V is between  $700 \div 840$  ° C and because during the EBM process a temperature of around  $600 \div 700$  ° C is kept, the material cannot maintain a martensitic structure (assumed that the martensitic phase appear) and decomposes completely, giving form to a mixed  $\alpha + \beta$  structure. In this work, the presence of martensitic phase was not found, even on the most superficial layers.

Regarding the width of the  $\alpha$  lamellae, these were smaller than those found in first deposited layers of about 70% [Figure 57]. It was found that the average size of the  $\alpha$  lamellae was greater in the sample "b" (about 1.1  $\mu\text{m}$ ) with a standard deviation of about 0.37  $\mu\text{m}$ . The smallest average width was found in the sample 'a' (just under 0.55  $\mu\text{m}$ ) with a standard deviation of about 0.23  $\mu\text{m}$ . The sample 'c' had  $\alpha$  lamellae width of about about 1  $\mu\text{m}$  with a standard deviation of 0.43  $\mu\text{m}$  and the sample 'd' had an  $\alpha$  lamellae average width of about 0.65  $\mu\text{m}$  with a standard deviation of 0.3  $\mu\text{m}$ .

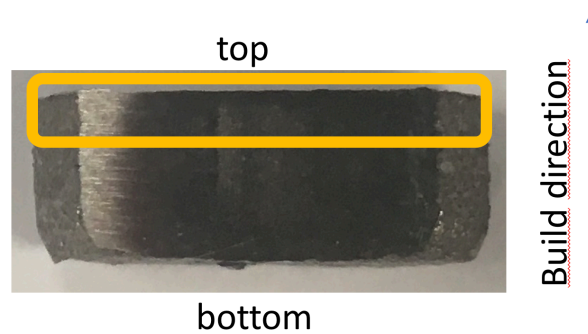


Figure 52 Macro-Scheme of the analyzed part.

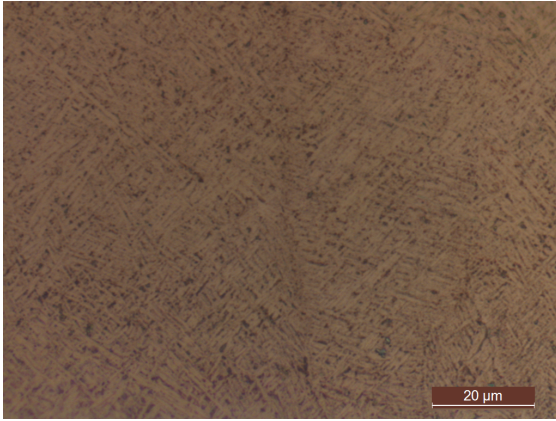


Figure 53 Sample "a":  $I = 15 \pm 20 \text{ mA}$ ,  $v = 4,53 \text{ m/s}$

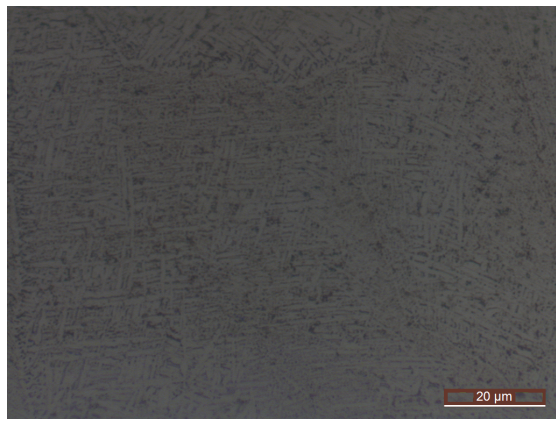


Figure 54 Sample "b":  $I = 15 \text{ mA}$ ;  $v = 4,53 \text{ m/s}$

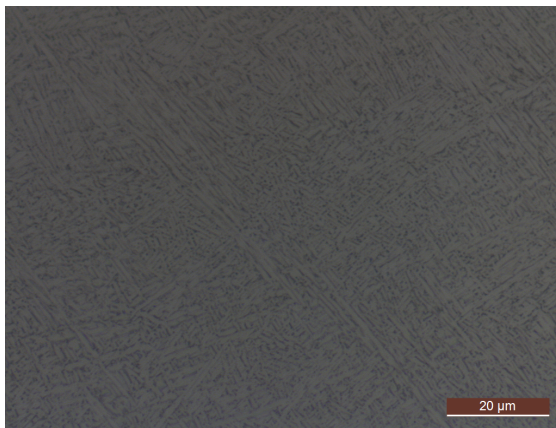


Figure 55 Sample "c":  $I = 15 \text{ mA}$ ;  $v = 5,9 \text{ m/s}$

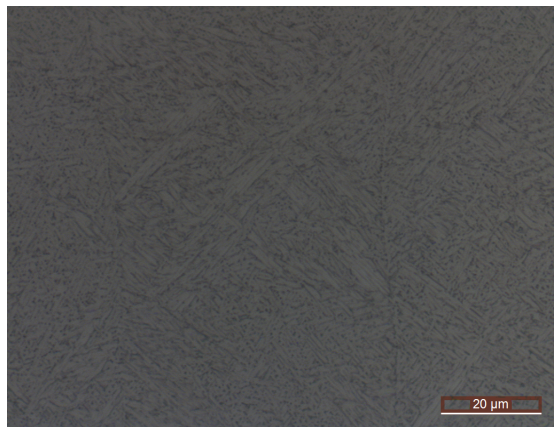
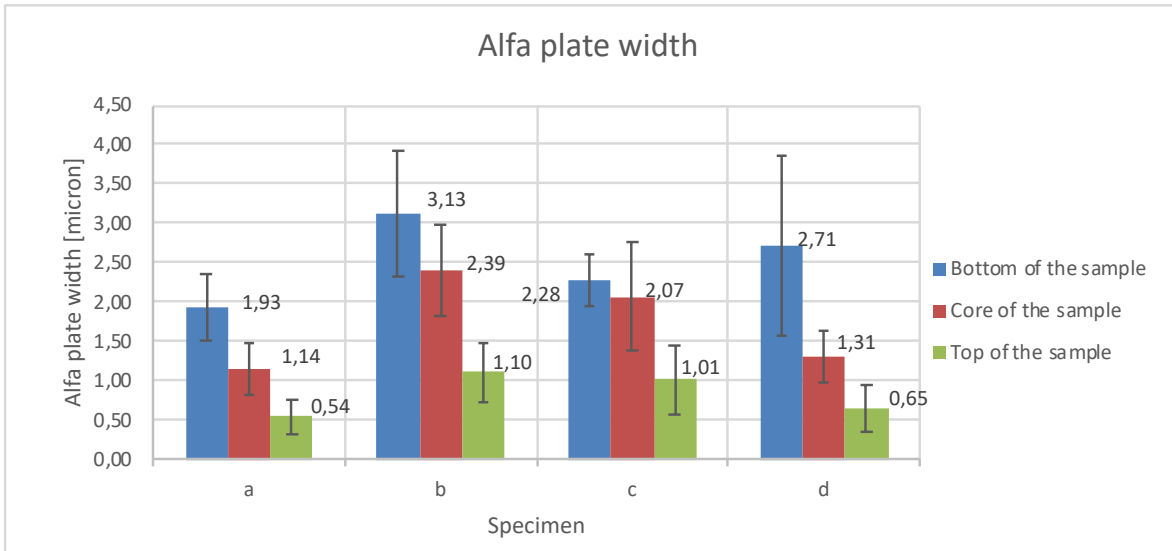


Figure 56 Sample "d":  $I = 12 \text{ mA}$ ;  $v = 4,53 \text{ m/s}$



Specimen	Parameters	Standard deviation		
		Bottom	Core	Top
a	Manufacturer build theme: l variable between 15+20 mA	0,44	0,34	0,23
b	l= 15 mA; v= 4,53 m/s; FO= 3 mA	0,8	0,58	0,37
c	l= 15 mA; v= 5,9 m/s; FO= 3 mA	0,33	0,69	0,43
d	l= 12 mA; v=4,53 m/s; FO= 3 mA	1,15	0,33	0,3

Figure 57  $\alpha$  lamellae widths at different distance from the build plate.

## 5.7 Tensile test

### 5.7.1 Procedure

It is recalled that the tensile test of the sample 'a' was not carried out because previous works were already performed with this process mode, thus, only the numerical results were reported. About the samples built in MM, both graphics and numerical results were shown. The tests were performed at room temperature (20 °C) on tensile samples with a functional area of 36 mm<sup>2</sup> and strain rate of 1 mm / min.

The [Figure 58, Figure 60] show the specimens with the respective fracture surfaces after having undergone the tensile test.



Figure 58 Sample “b”:

$I= 15 \text{ mA}$ ;  $v= 4,53 \text{ m/s}$



Figure 59 Sample “c”:

$I= 15 \text{ mA}$ ;  $v= 5,9 \text{ m/s}$



Figure 60 Sample “d”:

$I= 12 \text{ mA}$ ;  $v=4,53 \text{ m/s}$

## 5.7.2 Results and comparisons

It can be noted that the tests were successful carried out because the break occurred around the center of the length  $L_0$  (initial length of the useful stretch). The fracture surface was characterized by ductile tears resulting from the coalescence of microvoids [16].

In the document [1], comparisons regarding the mechanical properties of Ti-6Al-4V were reported. By comparing the results exhibited in the document [1] with those obtained in the following work, it can be seen that the actual UTS (ranging from 1045 to 1065 MPa) and YTS (899 - 991 MPa) values were generally higher than those found in ([12] (UTS ~775 MPa), [16] (UTS~928 MPa), [17] (UTS~915 MPa), [26] (UTS~959 ÷ 990MPa)) except for the sample ‘b’ which had a UTS~ 991 MPa, similar to ([26], [19]). The documents ([12], [16]) compared the properties of EBM samples with those of SLM samples. These papers showed that the strength of EBM-built specimens were slightly lower than those of SLM specimens, and these results were also confirmed in this work. The outcomes of the following work were in agreement with those found in [17], for which UTS and YS of Ti-6Al-4V EBM-built specimens were higher than those of wrought and annealed material. The

elongation of EBM-built specimens obtained in this work were higher than those of SLM-built specimens reported in [16] [18] and those EBM specimens made in [12] [16], but were slightly lower than the EBM samples values showed in the papers [26] [18] [19].

Comparing only the results of the following study, the UTS values are 1047 Mpa for the specimen made with BTM and vary between 992 and 1065 Mpa for the specimens made in MM [Figure 62, Figure 63]. As it can be clearly seen in [Figure 62], the defects shown in the sample ‘a’ do not greatly influence the mechanical properties as they are quite similar to those of the other samples . The specimen ‘b’ is the one that shows the minimum value of UTS (992 Mpa) while the specimens ‘a’, ‘c’ and ‘d’ show 1065 Mpa, 1052 Mpa and 1047 Mpa respectively. It is worth noting that there is a good agreement between mechanical properties and the microstructures, particularly between the average  $\alpha$ -width dimensions and the hardness values. Referring to the diagram [Figure 62], the higher UTS values correspond to the specimens that on average have a finer microstructure (sample a, c and d) [Figure 57], the sample ‘b’ which has a coarser microstructure shows lower values. The same reasoning is followed for the analysis of the yield stress, for which the sample ‘b’ has the minimum value (900 MPa) and the maximum value is given by the sample ‘d’ (991 MPa) [Figure 63]. The Young's module is minimal in the sample ‘a’ (107 GPa) and is maximum in the sample ‘d’ (116 GPa) while the other two specimens have intermediate values. The lowest elongation is given by the sample ‘c’ (11.7%) and it is little higher in the other cases (12 ÷ 12.6)%. The UTS for MM test specimens, as well as the YS, Young modulus and the elongation values for overall samples are listed in [Figure 62 - Figure 65].

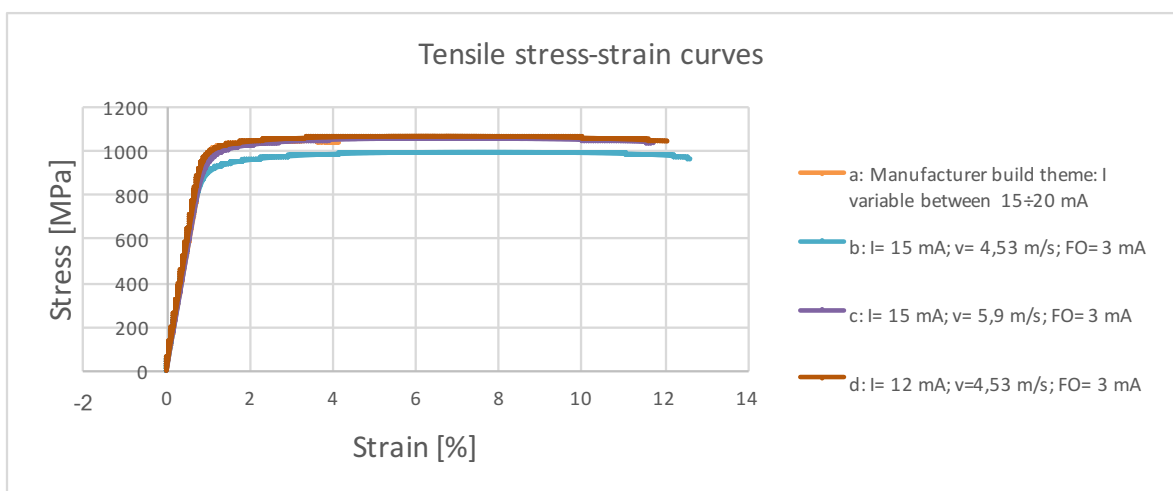


Figure 61 Stress-strain curves of the tested specimens.

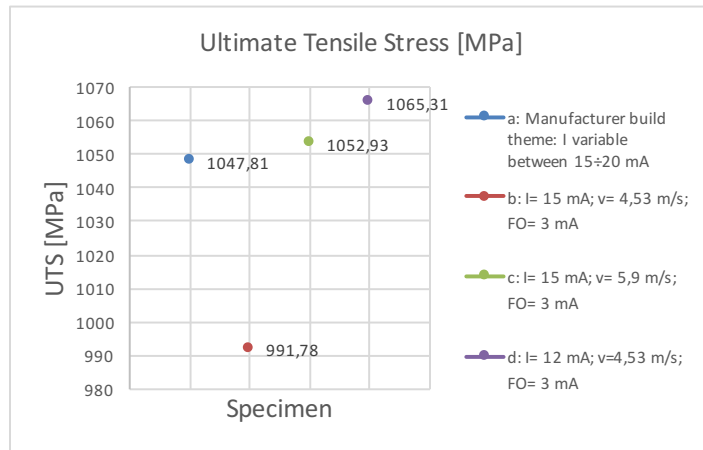


Figure 62 Ultimate Tensile stress of the tested specimens.

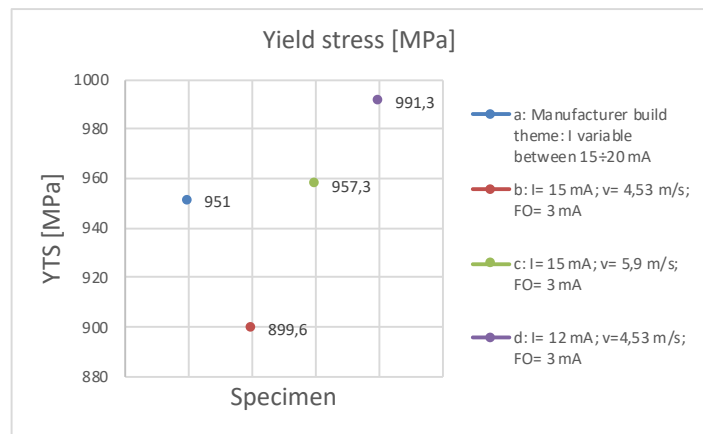


Figure 63 Yield stress of the tested specimens.

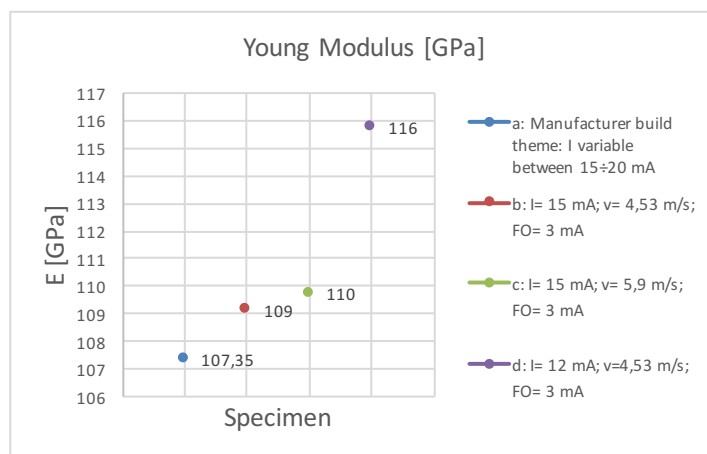


Figure 64 Young modulus of the tested specimens.

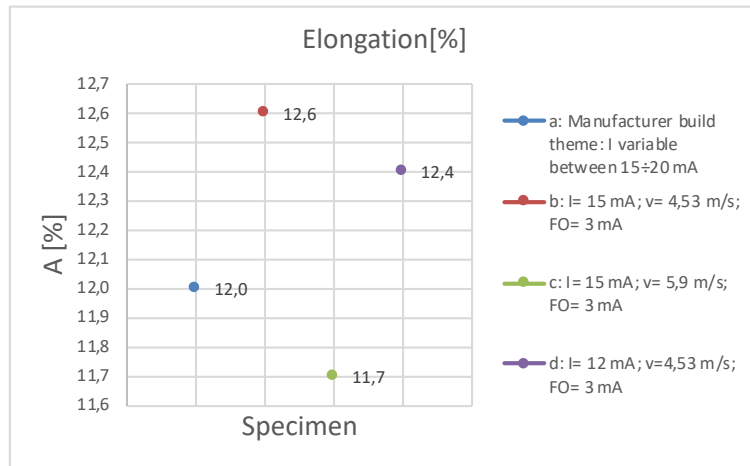


Figure 65 Elongation of the tested specimens.

## 5.8 Macro-instrumented indentation test

### 5.8.1 Procedure

For each specimen, three macro instrumented indentation tests were performed to a given load, following the standard UNI EN ISO 14577-1. The tests were carried out on the flat surface of the cylindrical specimens by applying a load at half width of them, respecting the appropriate distances from the edges and between the respective impressions [Figure 66].

Initially a reference specimen was taken, on which several first-attempt loads (100, 300, 400, 600, 700, 800, 1000) N were applied with different cycles and application times. 4 loading / unloading cycles were applied for each type of load, and each test was repeated 3 times. Once every single test load was applied, the results of the macro instrumented indentation test were analyzed through a MatLab post-processing program and they were compared with the mechanical reference properties of the material, taken from the literature. It was chosen the definitive applied load that would have given better results in terms of repeatability and congruence with the standard mechanical properties of the material. In this study, the load that gave the best results was 300 N.

Once the load was established (300N), all the specimens were subjected to 3 indentation tests [Figure 66], each one with 4 load cycles and with application times equal to 60s (loading), 60s (holding), 40 (unloading) respectively.

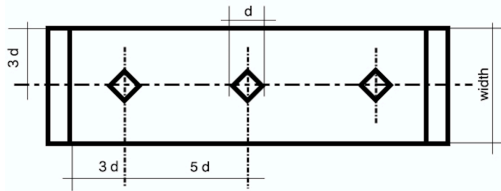


Figure 66 Macro indentation test: procedure scheme.



Figure 67 Three Macro indentation tests at 300 N on the real specimen .

## 5.8.2 Results and comparisons

In the [Errore. L'origine riferimento non è stata trovata. - Figure 73] the results of the 3 macro instrumented indentation tests are reported for each specimen, obtained with the pairs of process parameter described above [Figure 18].

In [Errore. L'origine riferimento non è stata trovata.] an average trend of the Loading, Holding and Unloading cycles of the samples 'a' – 'd' is reported, applying a load of 300 N. From the graph [Errore. L'origine riferimento non è stata trovata.], some main information such as the maximum displacement ( $h_{max}$ ) and plastic depth ( $h_p$ ) are illustrated. Analyzing the results in detail, the maximum penetration depth was obtained by the samples 'b' and 'c' with average values around  $66.5 \mu\text{m}$ , the specimen 'd' with an average depth of  $66 \mu\text{m}$  and the specimen 'a' with the minimum average value of  $61 \mu\text{m}$  [Figure 69].

The plastic penetration depth ( $h_p$ ) is a significant parameter to analyze. This is very low for the samples 'a' and 'd' ( $\sim 50 \mu\text{m}$ ), instead it is greater for the samples 'b' and 'c' (average values between  $52$  and  $53 \mu\text{m}$ ) [Figure 70].

In the [Figure 73] the projected area is shown ( $A_p$ ), which is a function of the contact depth ( $h_c$ ) when there is contact between indenter and material. The  $h_c$  parameter is smaller for the samples 'a' and 'd' ( $\sim 56 \div 59 \mu\text{m}$ ) and is higher for the samples 'b' and 'c' ( $\sim 60 \mu\text{m}$ ), and the projected area is proportional to the results obtained for  $h_c$ ; ( $\sim 0.08 \div 0.085 \text{ mm}^2$ ) for the samples 'a' and 'd', ( $\sim 0.09 \text{ mm}^2$ ) for samples 'b' and 'c', see [Figure 73].

The indentation modulus is one of the reference parameters used to validate the macro indentation test, through the comparisons of its values with the Young modulus values found in the standard tensile test. Based on average values, lower "Eit" values were obtained for the samples 'c' and 'd', 102 GPa and 100 GPa, and higher values for the samples 'a' and 'b', 127 and 114 GPa, were observed [Figure 71]. On average, the values in [Figure 71] are fairly in agreement with those found in the tensile test [Figure 64], allowing a comparison between the two mechanical inspection techniques.

Regarding the indentation hardness (Hit), the samples 'a' and 'd' obtained higher values, 3839 MPa and 3564 MPa, than the other two specimens 'b' and 'c', 3366 MPa and 3458 MPa respectively [Figure 72]. These values were converted to equivalent Vickers hardness values [Figure 74] and they were fairly in agreement with those of the Vickers hardness found in the literature ( [26] [16] [17] ). As it is well known from the theory [88], the hardness should decrease with increasing dimensions of the microstructure. In this study, the equivalent Vickers hardness was compared with the width of the alpha lamellae at half height of the sample, and from the results analyzed, the previous statement seems to be satisfied. It was seen that the hardness was greater where the microstructure was finer, with values of 362 MPa for the sample 'a', 336 MPa for the sample 'd', 326 MPa for the sample 'c' and 318 MPa for the sample 'b' [Figure 74]. It should be noted that these results seem to be in agreement with the microstructure analyzed previously in the paragraph [5.6.2]. In this case, since the indentation tests were carried out at half height of the samples, the "CORE PART" microstructure was chosen as the reference analyzed zone. In the [Figure 57] it can be observed that the microstructure of the samples 'b' and 'c' were slightly coarser than that of the samples 'a' and 'd', this leads to more pronounced deformations for the samples 'b' and 'c' (because the penetration depth  $h_p$  and  $h_c$  was greater) [Figure 69, Figure 70, Figure 73], showing lower indentation hardness (Hit) than the other cases [Figure 72] and exhibiting an indentation modulus (Eit) lower than the other samples [Figure 71].

Referring to the following legend, the results of macro indentation tests were reported in the following figures [Figure 68- Figure 73].

- a: Manufacturer build theme:  
Current range= 15÷20 mA; v=4,53 m/s
- b: I= 15 mA; v= 4,53 m/s; FO= 3 mA
- c: I= 15 mA; v= 5,9 m/s; FO= 3 mA
- d: I= 12 mA; v=4,53 m/s; FO= 3 mA

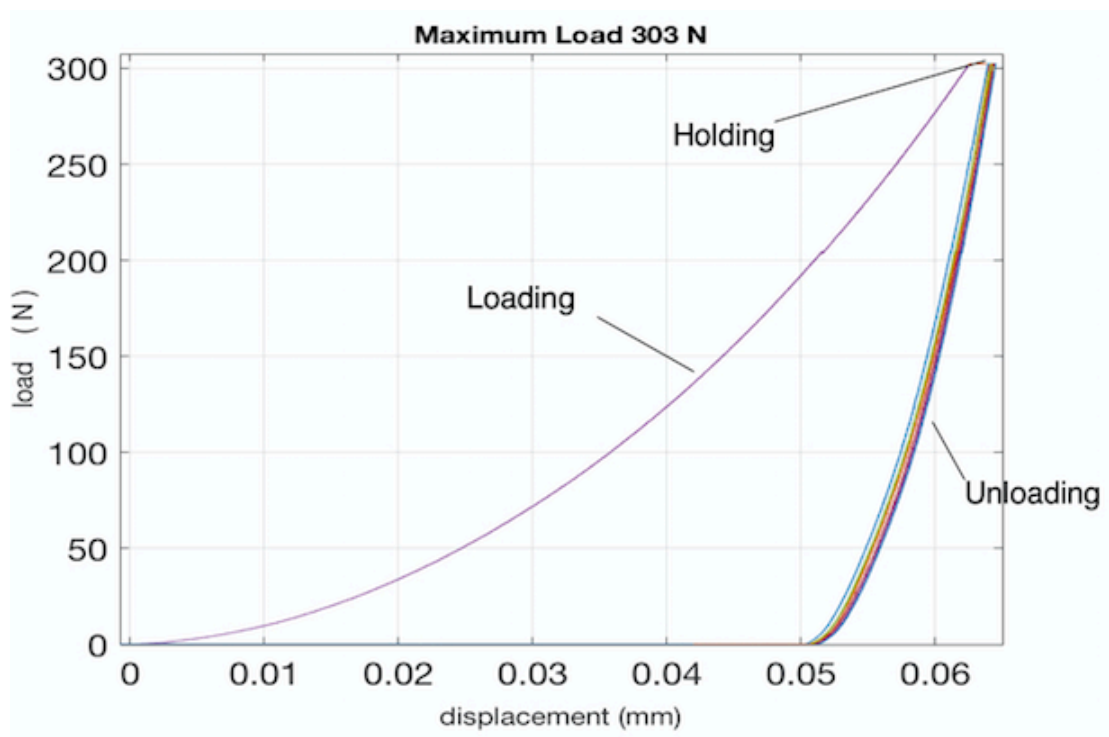


Figure 68 Load- displacement Graph of Macro instrumented indentation test.

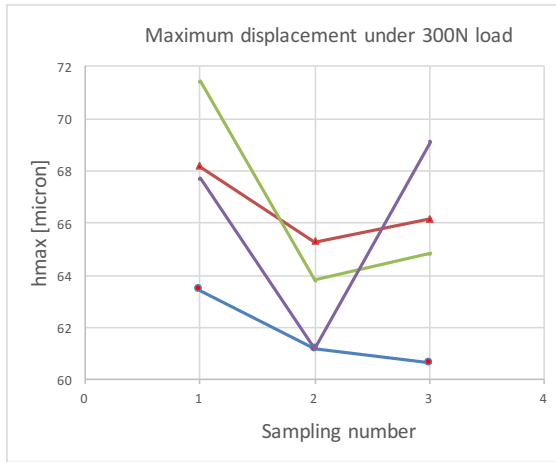


Figure 69 Maximum displacement under 300 N load. Blue/(sample a), red/(sample b), yellow/(sample c), purple (sample d)

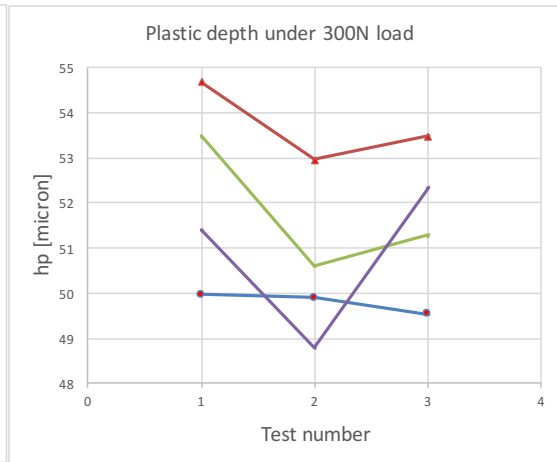


Figure 70 Plastic depth under 300 N load. Blue/(sample a), red/(sample b), yellow/(sample c), purple (sample d)

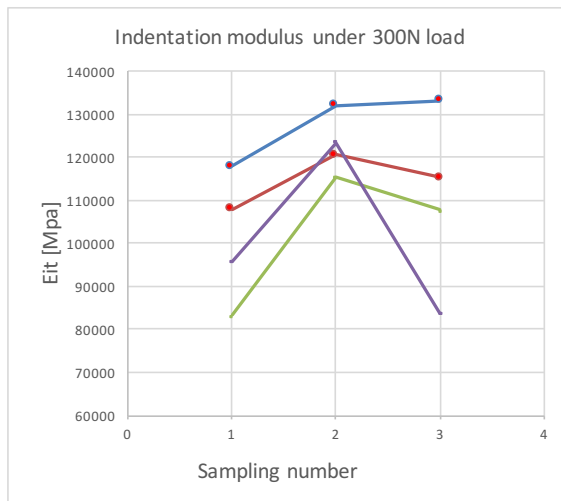


Figure 71 Indentation modulus under 300 N load. Blue/(sample a), red/(sample b), yellow/(sample c), purple (sample d)

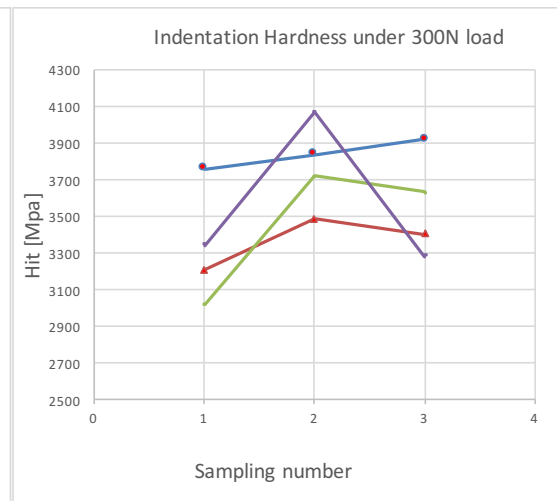


Figure 72 Indentation Hardness (Hit) under 300 N load. Blue/(sample a), red/(sample b), yellow/(sample c), purple (sample d)

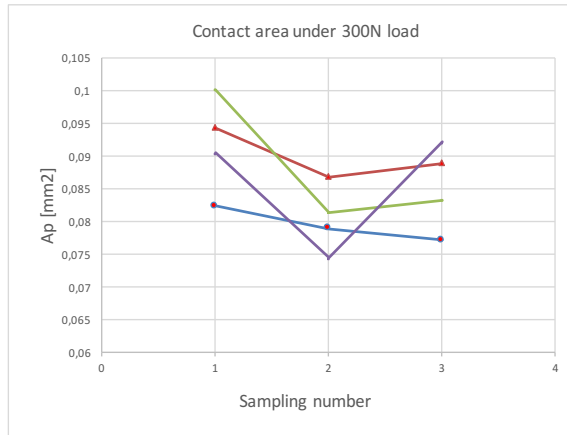


Figure 73 Contact area under 300 N load. Blue/(sample a), red/(sample b), yellow/(sample c), purple (sample d).

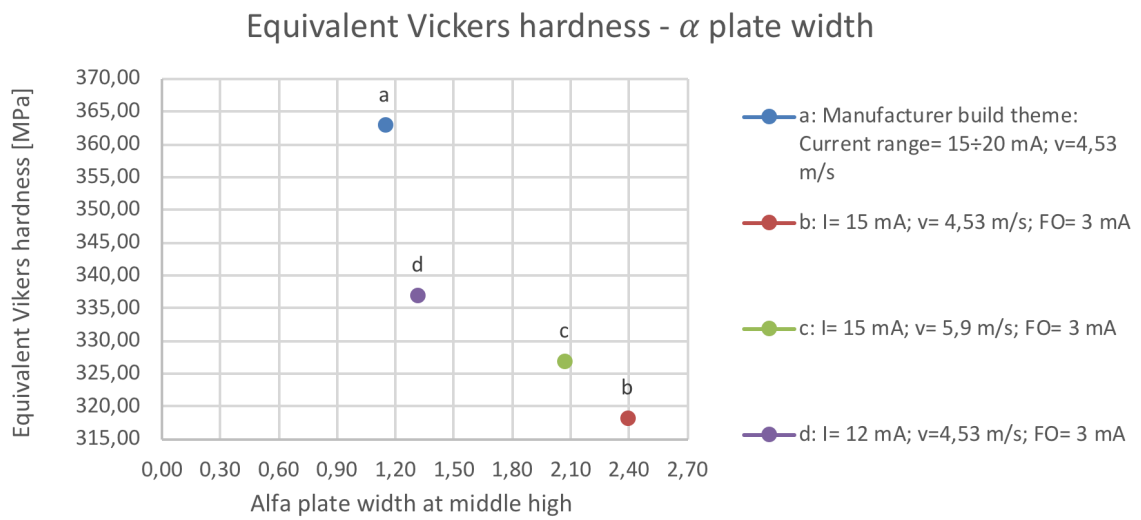


Figure 74 Equivalent Vickers hardness vs alfa plate width.

## 5.9 Comparisons between Macro-instrumented indentation test and Tensile test

In this chapter the results obtained from the tensile test and those obtained from the macro instrumented indentation test were compared.

In the [Figure 75] the Young Modulus and the indentation modulus were compared. The red, green and gray bars represent the indentation modulus values obtained for each of the three indentation tests on each specimen, while the blue bar represents the Young modulus obtained with the standard tensile test. The comparison must be made between the average indentation modulus, represented by the points connected by the cyan line, with the Young modulus obtained from the tensile test [Figure 75]. The sample 'a' showed an indentation modulus of 127 GPa, about 18% higher than the Young modulus found with the tensile test. The samples 'b', 'c' and 'd' exhibited values of 114 GPa, 102 GPa and 100 GPa, about 5%, 7% and 13% different from the Young modulus. These results allow to assert that there is a good agreement between the Young Modulus and the Eit, with an estimate error less than 20%.

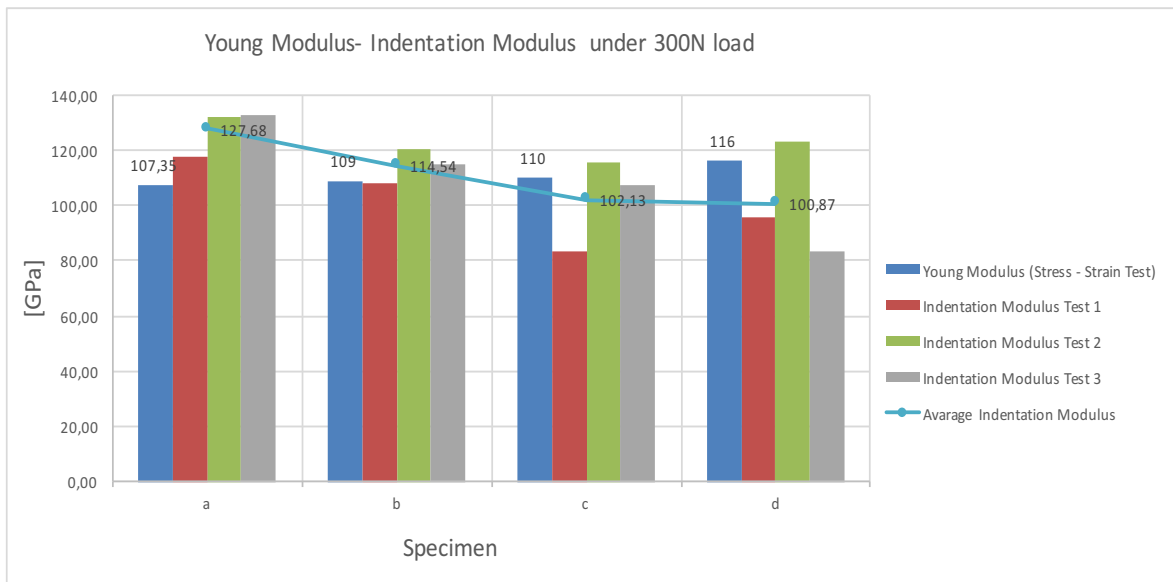


Figure 75 Comparison between Young modulus and Indentation Modulus (Eit).

The same reasoning was followed by comparing the average equivalent tensile strength (Hit/3), from Tabor ([89] [90], [91], [92]), with the UTS of the tensile test [Figure 76]. It was observed that, in all the cases, the average Hit/3 overestimated the UTS of the tensile tests with an error less than 20%. This results allowed a fair comparison between the two

inspection techniques and showed the efficiency of the macro instrumented indentation test as a non-destructive technique for the analysis of the mechanical properties of the material.

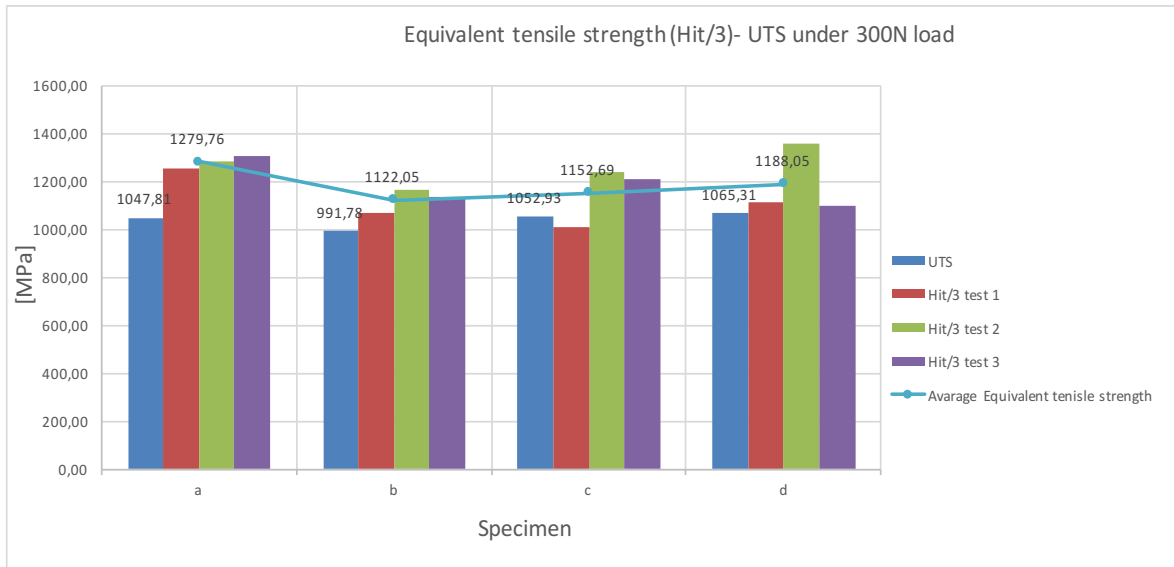


Figure 76 Comparison between Hit/3 and UTS.

As a last analysis, the values of the Equivalent Vickers hardness , calculated with [Equation 6], and the values of the theoretical Vikers hardness, found in literature for this alloy between 345 and 360 HV [23], were compared. Obviously it must be taken into account that the hardness varies with the variation of the build distance from the build plate as indicated in [25], even if this change in hardness has not been detected in the article [23]. However, the [Figure 77] showed that the equivalent Vickers hardness values, at half height of the sample, were found to be in the theoretical Vickers hardness range , 345 ÷ 360 HV.



Figure 77 Scheme of the equivalent Vickers Hardness.

## 6. Simplified EBM model

The last step to discuss is the development of the mathematical model that allowed to estimate the distribution of temperature on the powder during the EBM process. The complex physical process of the EBM has been studied by many authors ([93], [94], [95], [96]), trying to simulate as much as possible the real behavior of the material, obtaining useful information about the process parameters. Performing simulations of the process allows to have wide knowledges about the physical phenomena, leading to advantages in terms of time, cost and interfacing with the machine. As already mentioned in the chapter [2.1.1], the process is made up of several steps, which allow to understand the involved phenomena and the system complexity. Initially, the powder was spread on the surface of the build plate and after reaching the temperature of 730 ° C, the preheating and selectively melting steps (first making the contours of the part and subsequently the inner part) were repeated layer by layer. These repeated cycles lead non-equilibrium phenomena into the material (as seen in the previous chapter) generating very complex structures, difficult to predict during the design step, containing some defects such as melt ball formations, porosity, and layer delaminations [97]. The knowledge of the process temperature would allow to check the defects, facilitating the understanding and the guide of the process itself. As a rule, the EBM machine does not have any internal thermal imaging camera to directly detect the temperature into the system, there is only a thermocouple at the bottom of the build plate. The thermocouple gives only information about the bottom temperature of the build plate and it is insensitive to the variation of beam parameters, and then temperatures [50], for this reason, a temperature simulation model is required, which would allow to extrapolate this information. Several studies have been carried out on the 3D FEM analysis of the EBM process ([93], [94], [95], [96]) all focused on the determination and validation of the temperature generated by the interaction between electron beam and Ti-6Al-4V powder varying process parameters (beam current and beam speed). In all the documents steady process parameters were analyzed (MM), while the (BTM) was not simulated in any document. Also in the following work, the BTM process was not simulated because its automatic functions (developed by the manufacturer) that made it difficult to study.

In this work, a simplified temperature distribution MatLab model was developed, which consisted in: study the distribution of temperature of an infinite plate (Ti-6Al-4V powder as a continuum) that is quickly exposed to a uniform flow of energy considering the sintering

and melting phases. As reported in [93], "the process physics of EBAM is complex and many models are developed, which involve mass and heat transport, phase changes and interactions between thermal, mechanical, and metallurgical phenomena. On the other hand, there is a large scale of process modeling literature for processes similar to EBM, to some extent, such as electron beam welding (EBW) ([98], [99], [100], [101], [102]), laser deposition or melting ([103], [104]) and laser welding (LW) ([105], [106])".

In this thesis work, a one-dimensional model was developed following the study of [107] e [108], where an analytical model of the thermal field for one scan line during SLS and laser surface treatment was developed. This model considered conduction as the only mechanism of heat transfer. It was assumed that the thermal properties of the body were constant and the heat of melting was negligible. This means that the sintering zone and the powder are considered to have the same thermal properties regardless of temperature. In this study instead, the heat source of the documents [107] e [108] was modified, taking into account the heat lost by radiation, the heat lost by the evaporation of aluminum and temperature dependent material properties. Thermophysical properties, mechanical properties and the radiation term make this type of analysis highly nonlinear. The following paragraphs illustrate the equations used, with the appropriate assumptions and discussions.

## 6.1 Assumptions

1. The material is one -dimensional semi-infinite solid. This assumption is valid if the width of the melt zone is large compared to the melt depth.
2. All thermophysical properties of the material are considered to be temperature dependent. These properties are shown in the paragraph [6.3]: thermal conductivity according to [109] and [110], specific heat and heat capacity according to [109] and emissivity according to [110] and [111].
3. Initially the system is at a constant temperature of 730 ° C (preheating temperature)
4. The material is melted and rapidly cooled down by the exposition to a pulsed uniform flow of energy.
5. The model is valid only for very short interaction times, order of  $10^{-3}$ seconds; once this time have elapsed, convective motions are established in the molten pool, which are not taken into account in the presented model.

6. Since the EBM involves very rapid melting and solidification of the material, convective effect within the molten pool is not significant, therefore convective flow of heat was neglected.
7. The latent heat of melting was neglected
8. il flusso di calore sia normale alla superficie
9. The laser beam diameter is defined by the “focus offset” parameter imposed on the machine. In this case is equal to 200  $\mu\text{m}$ .

## 6.2 Equations

Since the EBM powder deposition is a thermal process, its understanding is driven by the heat conduction equation [112]. The heat conduction equation of a definite chosen volume, consists of the diffusive heat flows, the convective heat flows, and the possible sources of heat [113].

$$k \left( \frac{\partial^2 T}{\partial x^2} + \frac{\partial^2 T}{\partial y^2} + \frac{\partial^2 T}{\partial z^2} \right) + q = \rho * C_p * \frac{\partial T}{\partial t} + \frac{v \partial T}{\partial z}$$

*Equation 13*

A well-known approach to solve the heat conduction equation is by the use of Green's functions ( [108], [113] ) and the above assumptions. The simplified equation is then:

$$\frac{\partial T}{\partial t} = \frac{q}{\rho * C_p} + \frac{k}{\rho * C_p} \nabla^2 T$$

*Equation 14*

where  $q$  is the power generation per unit volume in the domain  $D$  ( $\frac{W}{m^3}$ ),  $\rho$  is the density ( $kg/m^3$ ),  $C_p$  is the specific heat capacity ( $\frac{J}{kg K}$ ),  $k$  is the thermal conductivity in the  $x$ ,  $y$  and  $z$  directions ( $\frac{W}{m K}$ ). Because the material is one -dimensional semi-infinite solid:

$$\nabla^2 T = \frac{\partial^2 T}{\partial x^2}$$

*Equation 15*

The heat input to the material is defined by the Lambert's law:

$$q = q_0 e^{(-\delta x)}$$

Equation 16

Where  $\delta$  is the Dirac delta function (extinction coefficient that expresses the attenuation of intensity at a certain distance),  $q_0$  is the net heat flux and 'x' represents the depth from the surface.

The boundary conditions are:

$$\frac{\partial T}{\partial x_{x=0}} = 0$$

$$T(\infty, t) = T_0$$

$$T(x, 0) = T_0$$

Equation 17

Where  $T_0$  is the pre-heating temperature, equal to 730°C.

As reported in [108], to solve the differential equation, an integral transform technique was used [114], yielding the following closed form solution of the distribution of temperature during heating and cooling step. Defining (t) as the time and ( $\tau$ ) as the interaction time:

$$\tau = \frac{\text{beam spot radius}}{\text{beam speed}}$$

Equation 18

It follows that:

- During the heating step, for  $t \leq \tau$

$$T(x, t) = T_0 + \frac{q_0}{k} * \left[ \sqrt{\frac{4\alpha t}{\pi}} e^{-\left(\frac{x}{\sqrt{4\alpha t}}\right)^2} - x \operatorname{erfc}\left(\frac{x}{\sqrt{4\alpha t}}\right) \right]$$

Equation 19

- During the cooling step, for  $t > \tau$

$$T(x, t) = T_0 + \frac{q_0}{k} \left[ \sqrt{\frac{4\alpha t}{\pi}} * e^{-\left(\frac{x}{\sqrt{4\alpha t}}\right)^2} - \sqrt{\frac{4\alpha\gamma}{\pi}} * e^{-\left(\frac{x}{\sqrt{4\alpha\gamma}}\right)^2} - x \operatorname{erfc}\left(\frac{x}{\sqrt{4\alpha t}}\right) + x \operatorname{erfc}\left(\frac{x}{\sqrt{4\alpha\gamma}}\right) \right]$$

Equation 20

where  $\alpha$  is the thermal diffusivity  $\left[\frac{m^2}{s}\right]$  equal to  $\left(\frac{k}{\rho * C_P}\right) = \left[\frac{m^2}{s}\right]$ ,  $T_0$  is the preheating temperature of 730 °C and  $\gamma$  is defined as:

$$\gamma = (t - \tau)$$

At the top surface of the material ( $x=0$ ) the [Equation 19] reduces to

$$T(t) = T_0 + \frac{q_0}{k} \left( \sqrt{\frac{4\alpha t}{\pi}} \right)$$

Equation 21

And [Equation 20] becomes

$$T(t) = T_0 + \frac{q_0}{k} \left( \sqrt{\frac{4\alpha t}{\pi}} - \sqrt{\frac{4\alpha\gamma}{\pi}} \right)$$

Equation 22

With this distribution, the temperature of any point placed at coordinate  $x(t)$  below the surface is possible to know. On the top surface ( $x=0$ ), net heat flux is given by the difference between beam heating and losses due to radiation and evaporation of alluminum. Assuming a Gaussian flux profile [96], for a beam power of  $P= V * I$ , the heat flux equation is given by [96]:

$$q_0 = \frac{V * I}{\pi R^2} - \varepsilon \sigma (T_{Ti-6Al-4V}^4 - T_{730^\circ C}^4) - J * \Delta H_v$$

Equation 23

$V$  is the acceleration voltage [kV],  $I$  is the beam current [mA],  $\varepsilon$  and  $\sigma$  are the radiative emissivity and Stefan-Boltzmann constant for radiation ( $5.67 \times 10^{-8} \left[\frac{W}{m^2 * K^4}\right]$ ),  $J$  is the flux of evaporating metal from the surface assumed to follow Langmuir's formula [96], and  $H_v$

is the latent heat of vaporization of aluminum equal to  $1,053 \cdot 10^7 \frac{J}{Kg}$ . Sih and Barlow [115] developed and validated a porosity dependent emissivity model for a metallic powder bed:

$$\varepsilon = A_H \varepsilon_H + (1 - A_H) \varepsilon_s$$

*Equation 24*

where  $A_H$  is the area fraction of the surface that is occupied by the radiation-emitting holes,  $\varepsilon_s$  is the emissivity of the solid particle and  $\varepsilon_H$  is that of the hole. The emissivity of the liquid state ( $T > 1650^\circ\text{C}$ ) is given by [111], and it is equal to:

$$0,425 - 1,05 \cdot 10^{-5} \cdot T$$

*Equation 25*

Once the equations used in the study have been defined, the thermophysical properties of the material have been established as the temperature changes, which are reported in the following paragraph.

## 6.3 Powder, solid and liquid material properties

It is important to remember that the Ti-6Al-4V alloy has a melting temperature  $T_{liquidus}$  equal to  $1665^\circ\text{C}$  and a  $T_{solidus}$  equal to  $1605^\circ\text{C}$ . The properties of the powder were calculated and modeled with reference to the bulk material. Regarding the density, at temperatures between  $730^\circ\text{C}$  and  $1600^\circ\text{C}$  the material begins a partial sintering and the values slightly increase with a linear law. From this point, the sintering step continues up to temperatures slightly above  $1665^\circ\text{C}$ , following an exponential law, until reaching the density value of the liquid material shown in the tables [109] ( $3800 \text{ kg} / \text{m}^3$ ). The figure below [Figure 78] shows the density trend of Ti-6Al-4V powder as a function of the temperature, taking into account the sintering phase. Otherwise the [Figure 79] shows the density trend of the liquid and solid phases as a function of the temperature ([109], [116]).

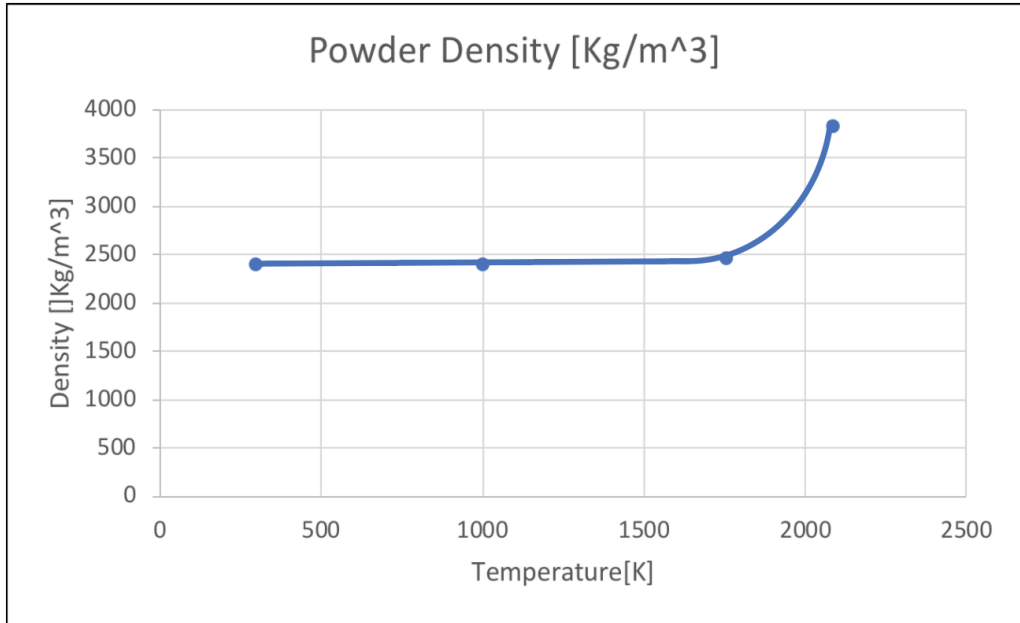


Figure 78 Density of Ti-6Al-4V powder as a function of temperature.

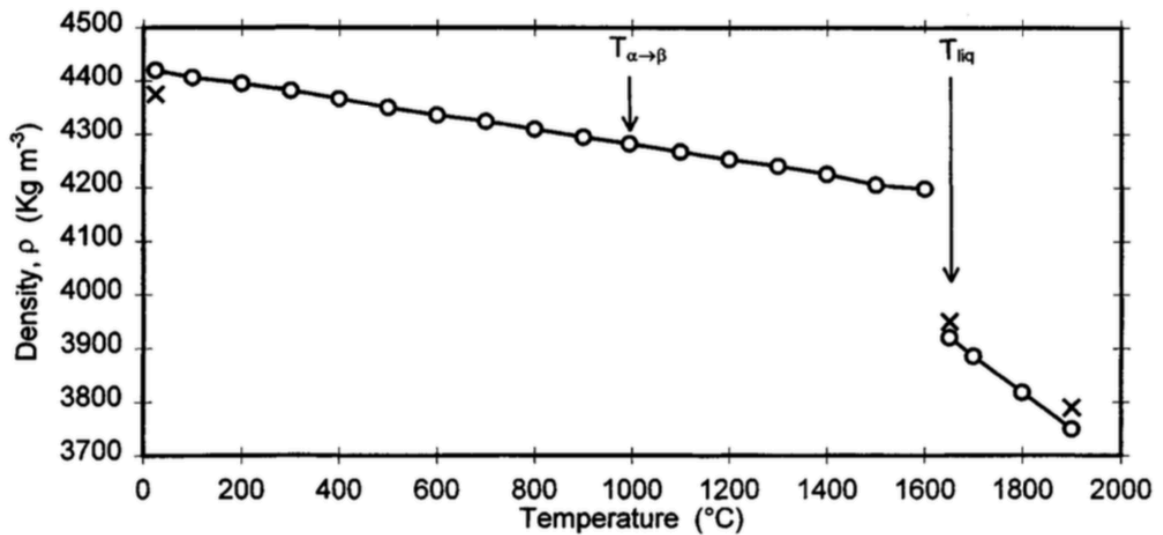


Figure 79 Density of Ti-6Al-4V as a function of temperature from [109]. Recommended values from [116].

Regarding the Thermal conductivity of the powder, the reasoning made by [114] was followed. Generally, “ the principal mechanisms of heat transfer that influence the Thermal conductivity are [117]: thermal conduction in gas filling the pores, radiative thermal conduction through the pores, and contact thermal conduction between the particles. Because in this case the powder bed is held under vacuum, only the radiative and contact mechanisms are expected to effect the thermal conductivity ‘k’:

$$k = k_r + k_c$$

Equation 26

where  $k_r$  is the effective thermal conductivity due to thermal radiation and  $k_c$  is due to the heat transfer through necks. The radiative conductivity term is estimated by ([118], [110]) :

$$k_r = \frac{16}{3} * l\sigma T^3$$

*Equation 27*

where  $l$  is the mean photon free path between the scattering events,  $\sigma$  is the Stefan-Boltzmann constant, and  $T$  the temperature. In the case of powder, ' $l$ ' is of the order of the pore size which, in its turn, is about the particle size. In the present study, the mean free path ' $l$ ' is set to the particle diameter ( $55 \mu\text{m}$ ). The contact conductivity ( $k_c$ ) is proportional to the linear size of the contact between the two particles [119]. To estimate the effective contact thermal conductivity, the powder is considered as a packed bed of equal spheres connected by small circular necks [110]. The thermal conductivity is given by the general equation :

$$K_c = \Lambda\lambda_0x$$

*Equation 28*

where  $\Lambda$  is the normalised contact conductivity equal to  $\sqrt{3}$  for the Ti-6Al-4V alloy; ' $x$ ' is the relative size ( $x=b/R$ ), the ratio between the neck radius ( $b$ ) and the radius of the particle ( $R$ );  $\lambda_0$  is the theoretical thermal conductivity of the solid material taken from [109]. For what has been said, the behavior of the thermal conductivity of the Ti-6Al-4V powder as a function of temperature is that shown in [Figure 80]. In the [Figure 81], the trend of the thermal conductivity, for the liquid and solid alloy, taken from document [109], is reported" [110].

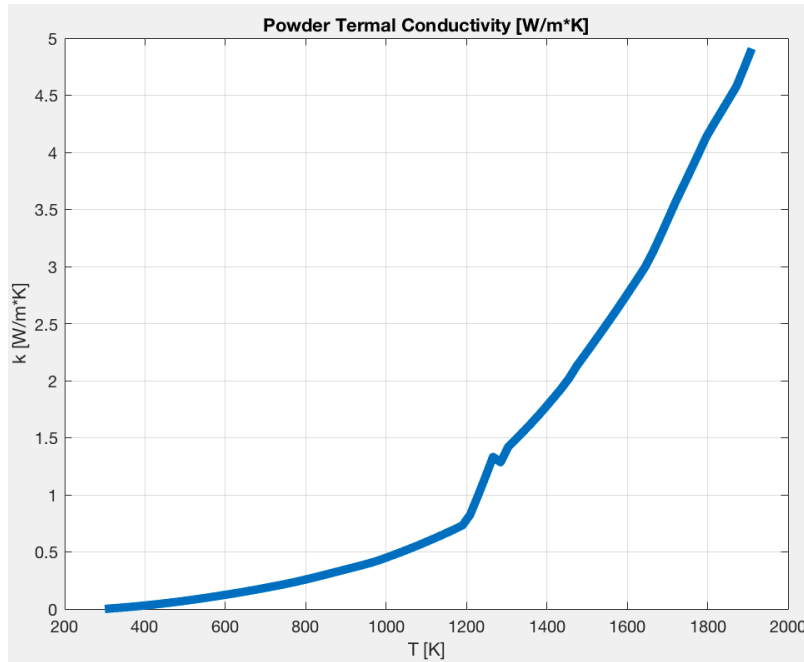


Figure 80 Thermal conductivity of Ti-6Al-4V powder as a function of temperature.

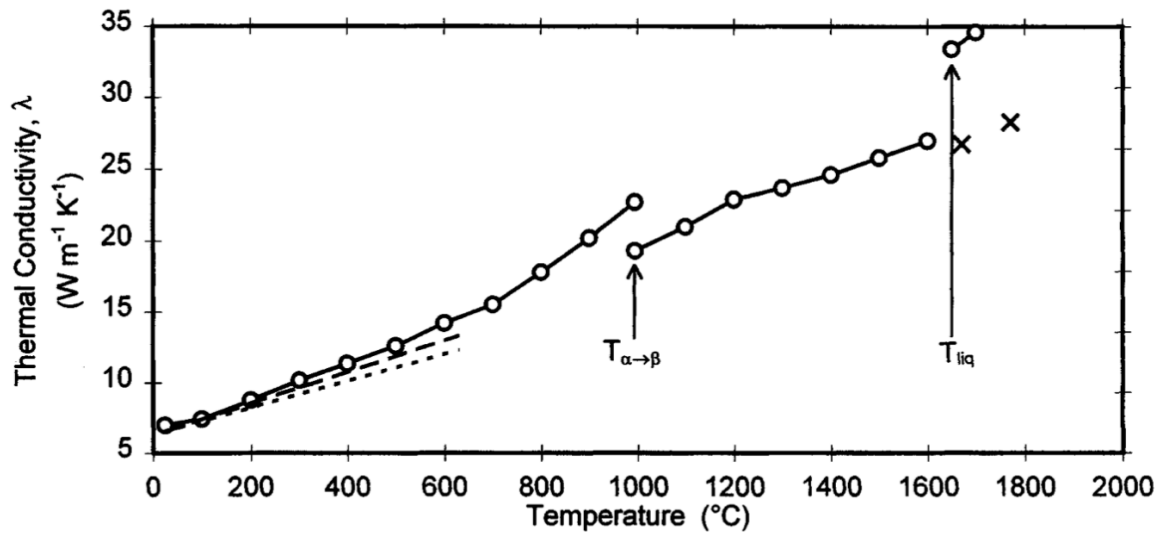


Figure 81 The Thermal conductivity of Ti-6Al-4V as a function of temperature, from [109].

The specific heat capacity of the powder is equal to that of its respective bulk material. The following image shows the trend of the heat capacity, taken from the document [109].

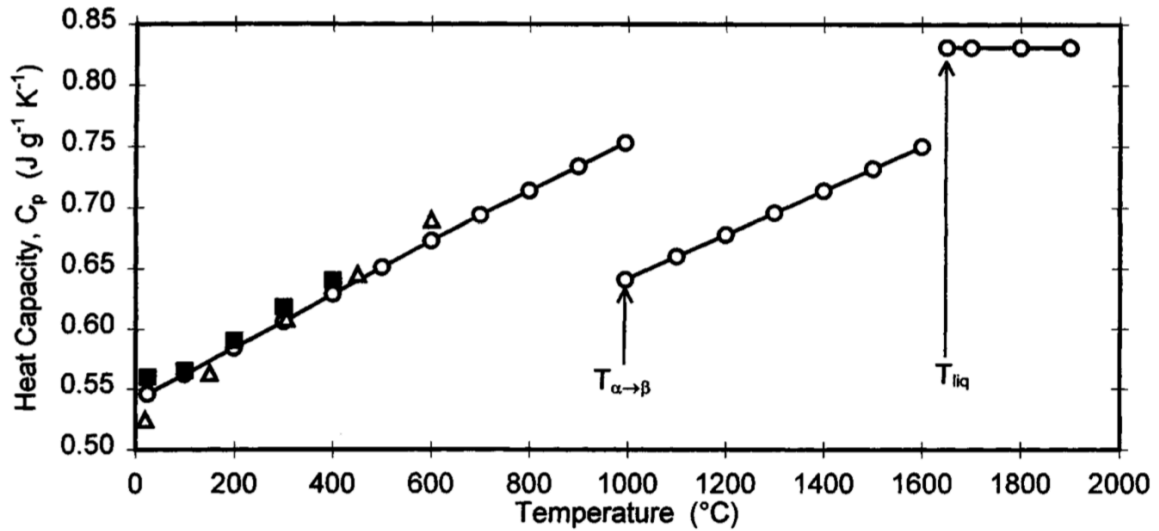


Figure 82 The heat capacity of powder, liquid and solidus Ti-6Al-4V as a function of temperature, from [109].

## 6.4 Model structure

The developed MatLab model, based on [107] e [108], is an algorithm that works by successive steps, calculating each time the temperature value on the surface of the material. As the first step, all the thermophysical properties were loaded [paragrafo 6.3] and were used by the algorithm through an interpolation with the temperature. Initially, a control parameter (CP) was set to associate the actual thermophysical properties, powder / solid or liquid, to the material, as a function of the temperature calculated at the previous time step.

Referring to [Figure 83], the analytic model follows the described procedure:

- 1) First of all, the thermophysical properties are calculated at the time  $t = 0$  and  $T = T_0$ , which will be used to derive the temperature at the initial step  $t_1$ , namely  $T_1$ .
- 2) After that, the  $T_1$  temperature is used to calculate the thermophysical properties for the subsequent instant  $t_2$ , used to determine the temperature value at that time and so on.
- 3) The process continues step by step, determining the thermophysical properties at the instant ( $t$ ) through the temperatures calculated at the previous time step ( $t-1$ ).
- 4) The CP parameter represent the border line beyond wich the calculated properties no longer refer to the powder or solid material, but to the liquid material. As regards the heating phase, if the temperatures  $T(t-1)$  are below the melting point (1665 °C) then the properties refer to the powder phase, instead for  $T(t-1) > 1665$ , the temperatures

$T(t)$  are calculated referring to the liquid properties. During the cooling steps the same processes happens; the liquid properties are attributed to the material if the temperature of the previous time step  $T(t-1)$  is higher than the solidus temperature and those of the solidus state are used if the temperature  $T(t-1)$  is lower than the solidus temperature.

- 5) For each subsequent step, the progress time is checked to ensure it is lower than the validity limit of the model ( $10^{-3}$ s). Once this value is exceeded, the simulation will be terminated.
- 6) Through this procedure, the following graphs are obtained [Figure 84 - Figure 86], for different pairs of parameter ( beam current and beam speed).

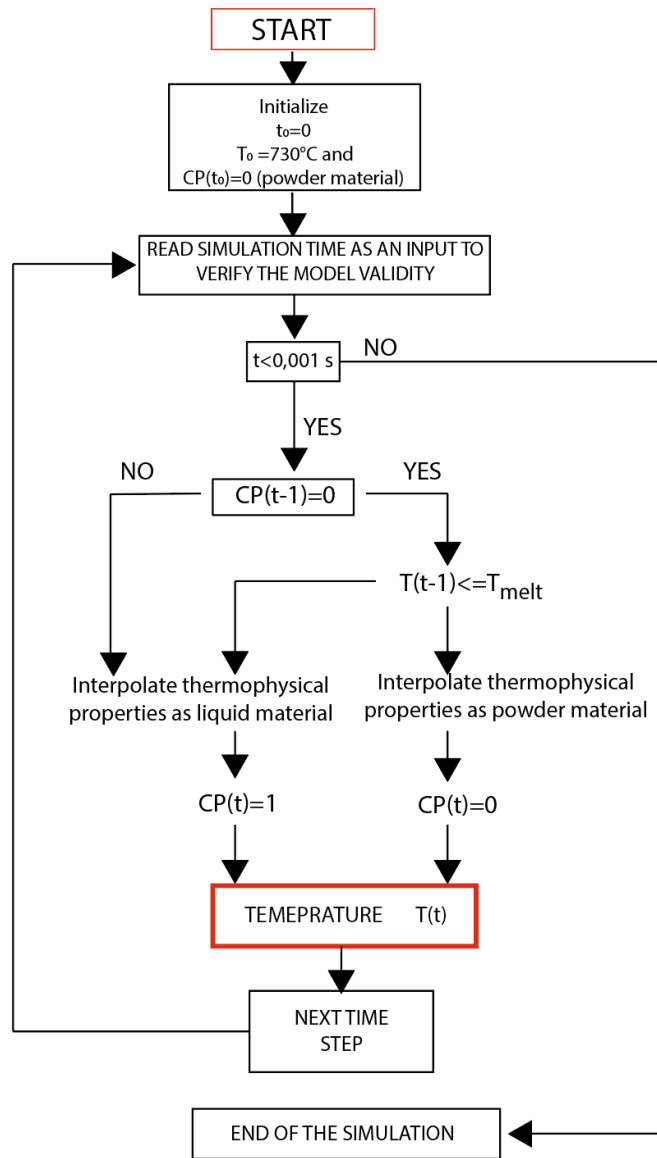


Figure 83 Flow chart for subroutine used in MatLab.

Three simulations were carried out: the first related to the sample ‘b’ ( $I = 15 \text{ mA}$ ,  $v = 4.53 \text{ m / s}$ ) [Figure 84]; the second related to the sample ‘c’ ( $I = 15 \text{ mA}$ ,  $v = 5.9 \text{ m / s}$ ) [Figure 85]; the third one related to the sample ‘d’ ( $I = 12 \text{ mA}$ ,  $v = 4.53 \text{ m / s}$ ) [Figure 86]. Regarding the sample ‘a’, the simulations were not carried out because the complex automatic algorithm (developed by the manufacturer and not available to the user) involved in the process. To overcome this drawback, the manufacturer provided a table that showed the maximum temperatures generated by set a pair of parameters, such as: current and speed factor. In the following work a speed factor value of 98 was used, set by the manufacturer.

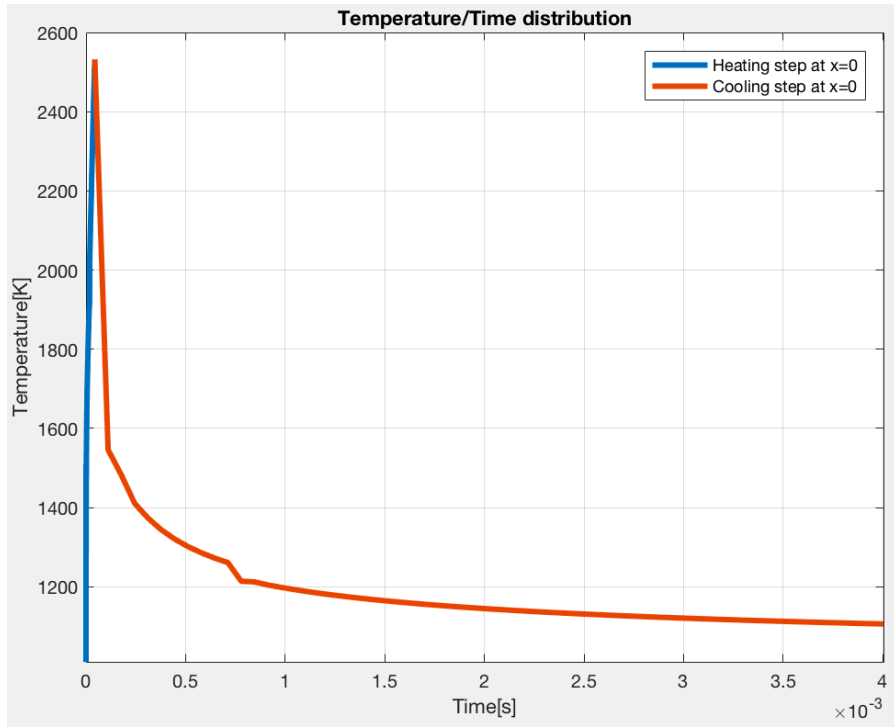


Figure 84 Sample b:  $I=15$  mA,  $v=4,53$  m/s

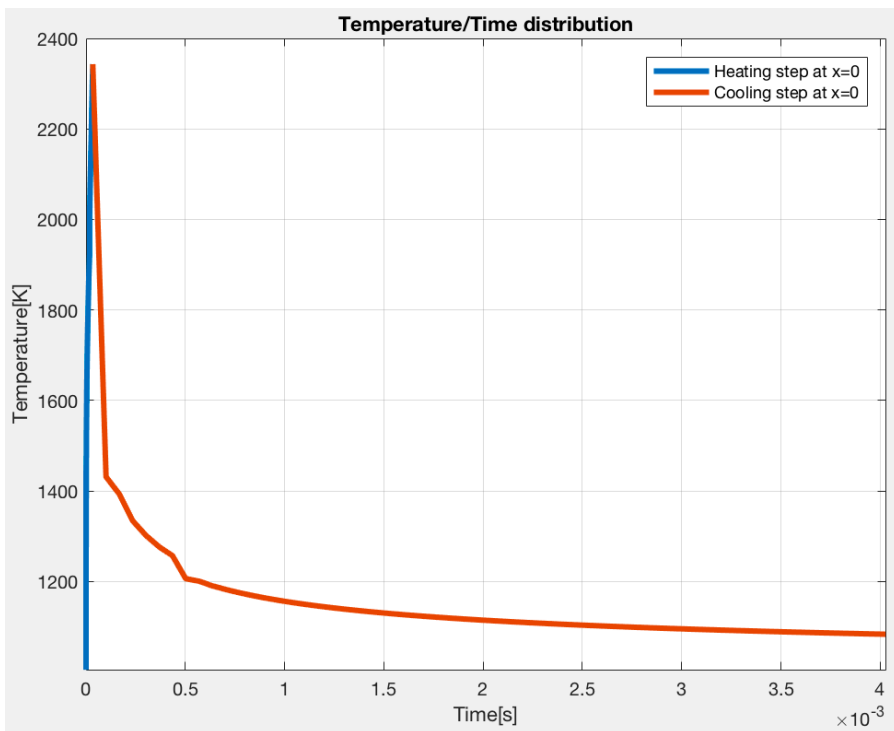


Figure 85 Sample c:  $I=15$  mA,  $v=5,9$  m/s

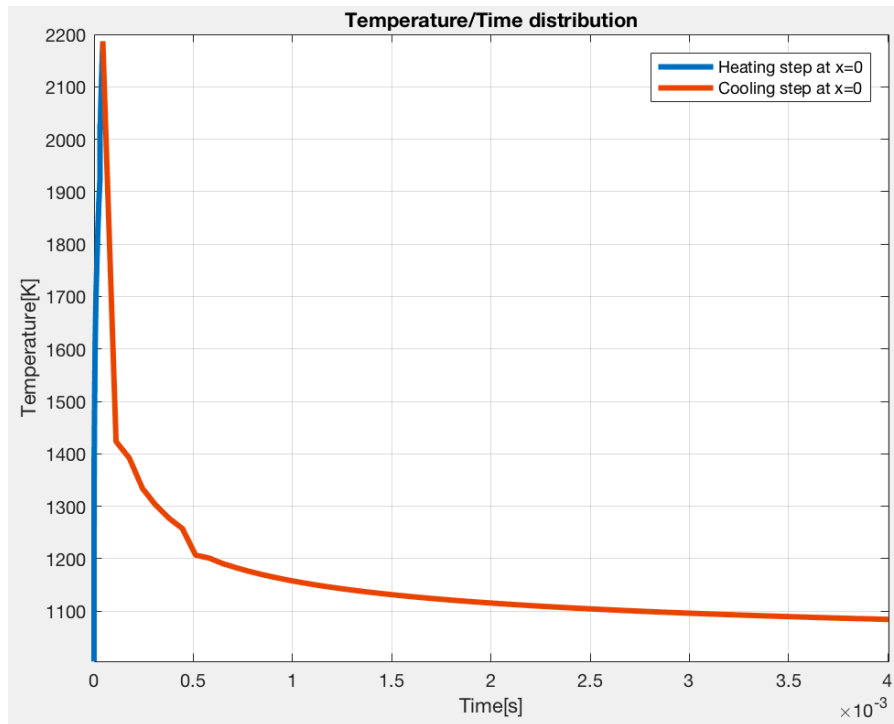


Figure 86 Sample “d”:  $I=12$  mA,  $v=4,53$  m/s

As it can be observed, the temperature profile is similar to that of many other studies ([120], [96], [108], [121] etc.). It should be noted that the time ( $\tau$ ) for which the maximum temperature is reached is around the order of  $10^{-4}$  s, as in the documents ([119], [96]). Observing the rapid cooling occurred during the process, and comparing the trend with other studies, a probable formation of martensite could be admitted. The model was validated with the documents ([96], [108]). Thinking in terms of maximum generated temperatures and looking for correlations with the analyzed microstructures [chapter 5.6] it can be seen that: the finest microstructure was obtained in the sample ‘a’ where the maximum reached temperature was around  $2900^{\circ}\text{C}$  (tabulated value), however it had higher presences of unmelted zones and porosity (linked to the high quantity of evaporated aluminum), large distortions and deformations (linked to the high shrinkage stresses of the material)[Figure 22, Figure 34 - Figure 36]. These defects make the final product unacceptable and lead to discard, in this case, the BTM as a methodology process choice. This does not mean that the BTM is less good than the MM, but it is a proof that BTM is not always the best methodology to adopt. The defects of the sample ‘a’ were related to the high temperatures linked with the speed factor, which must be modified in order to obtain more reasonable results. Turning to the MM, the sample ‘b’ was the one that showed higher temperature than the samples ‘c’ and ‘d’, about  $2532^{\circ}\text{C}$ . The microstructure of the sample ‘b’ was slightly coarser and had more microporosities than the sample ‘a’ [Figure 32] even if the deformations were slightly

smaller [Figure 23]; nevertheless, the deformations were considerably larger than the samples 'c' and 'd'. Also in this case the causes of these defects were linked to the high temperature. About the sample 'c', the maximum reached temperature was 2343 °C, there were still some not fused areas on the bottom of the specimen [Figure 37] but the shape of the sample was quite in accordance to the CAD design measurements. The sample 'd' showed a maximum temperature of 2187 °C proving a good microstructure, less aesthetic and internal defects compared to the other cases [Figure 25, Figure 31,

Figure 33], good mechanical properties and it was in good agreement with the CAD design measurements [Figure 20, Figure 19]. The presence of defects can not be only influenced by the maximum generated temperature, since there are convective and heat accumulation effects between the deposited layers that would greatly affect the results obtained. However, the simplified MatLab model gave a general idea of the established temperatures during the process. To achieve better quality and accuracy results, the model calibration through real-time temperature measurements would be necessary, using infrared cameras or other optical supervision systems.

## 7. Inconveniences and future work

Working several times with the EBM machine, different 'inconveniences', which caused considerable loss of time, were faced. The aspects that have influenced more in terms of production times were considered in the following exposition.

For the production of three tensile specimens and three cylindrical specimens in a single process [Figure 19 and Figure 20] the following times were recorded:

- Time to reach the vacuum ( $10^{-5}$  mbar)  $\sim$  40 min
- Time to heat the build plate up to  $730^{\circ}\text{C}$   $\sim$  30/40 min
- Time to cool down the build plate from  $730^{\circ}\text{C}$  to  $T_{amb}$   $\sim$  3/4 hours (only when the system stop before starting the build step).
- Time to cool down the system when the build is done  $\sim$  6-7 hours

Because of these very long times, a sudden stop of the machine or even errors during the calibration of some components would lead to high loss of time.

Many times the process was started and suddenly the machine stopped. The problem, in most cases, was connected to an inadequate cleaning of the machine. Titanium powder or evaporated aluminum residues infiltrated both into the Beam column, where a very thin aluminum sheet is positioned, and into the two parts shown below: the drift tube and the anode.

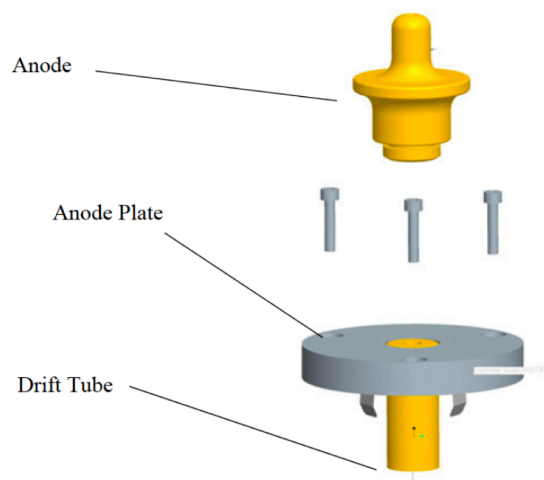
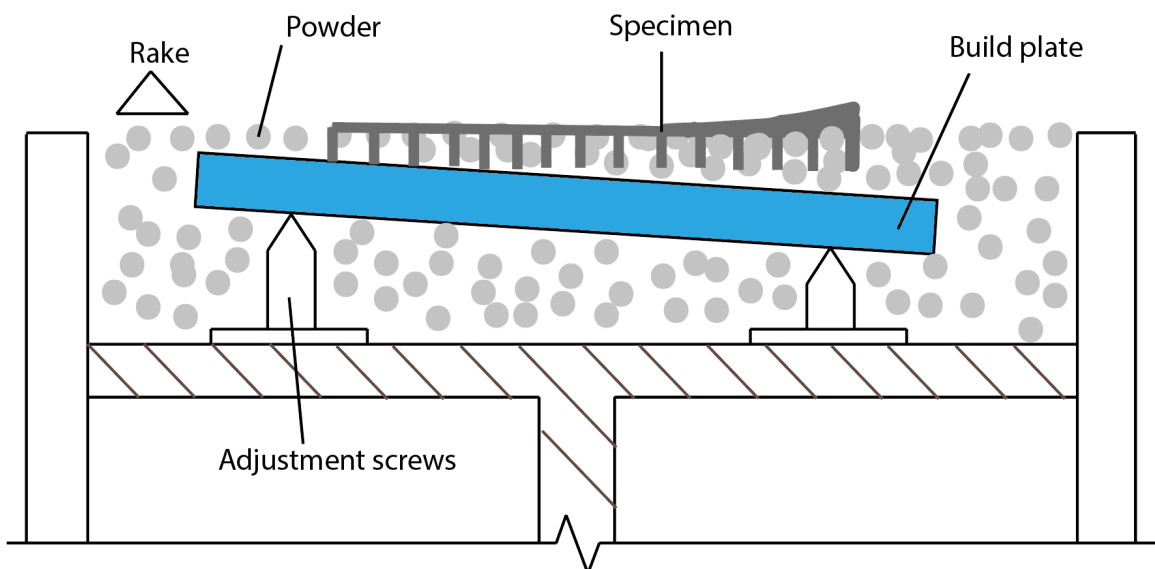


Figure 87 The anode and the drift tube

In order to solve the problem, before starting the process, these components had to be removed and cleaned thoroughly with a clean cloth and an appropriate liquid. Sometimes, even after have cleaned the components, the machine still suffered sudden stops and there was no other way to clean everything again.

- Another drawback was the centering and alignment of the build plate.

This procedure took place in a completely manual manner and had to be carried out every time before starting the process. This procedure was fundamental because the wrong alignment of the plate makes the process unstable. If the plate is not perfectly aligned, once the rake has passed, the powder will have an irregular distribution on the surface. In those areas where more powder is, the supports do not well adhere to the build plate and deformations due to shrinkage of the material can not be avoided, resulting in completely deformed parts, see [Figure 88].



*Figure 88 Miss alignment with respect to the EBM axis.*

The machine has 4 adjustment screws on which the build plate is placed. To guarantee a good alignment of the plate, the powder should be spread on the surface as good as possible by the use of the rake. It has been tried to perform a faster procedure through the use of a liquid bubble measuring instrument, but the results were not acceptable because the lack of parallelism between the build plate and the floor on which the machine was placed, see [Figure 89]. The following image shows the exact calibration performed with the rake that results completely different from the liquid bubble measurement.

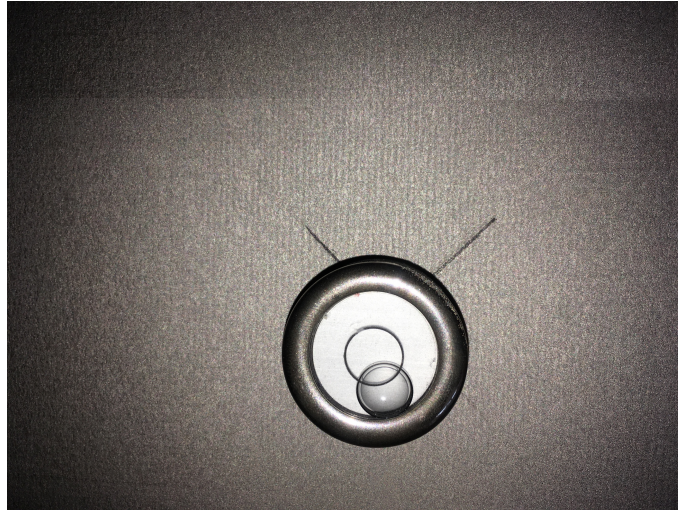


*Figure 89 Correct positioning of the build plate through the rake system vs. wrong positioning of the build plate through liquid bubble measuring instrument.*

- Frequent cleaning of the beam gun (column inside which the electron beam passes) and the components inside the chamber are required. The high amount of aluminum evaporation causes sudden machine blockages that force to re-initialize the process.
- One of the main relevant inconveniences is the impossibility to detect the temperatures during the process. The machine has only a thermocouple located at the bottom of the build plate. To monitor the temperatures during the process it would be necessary an infrared camera. In many documents, constructive machine modifications were made allowing the installation of infrared cameras. Some examples are available in the following works ( [122], [123], [124]) and showed the subsequent configurations:

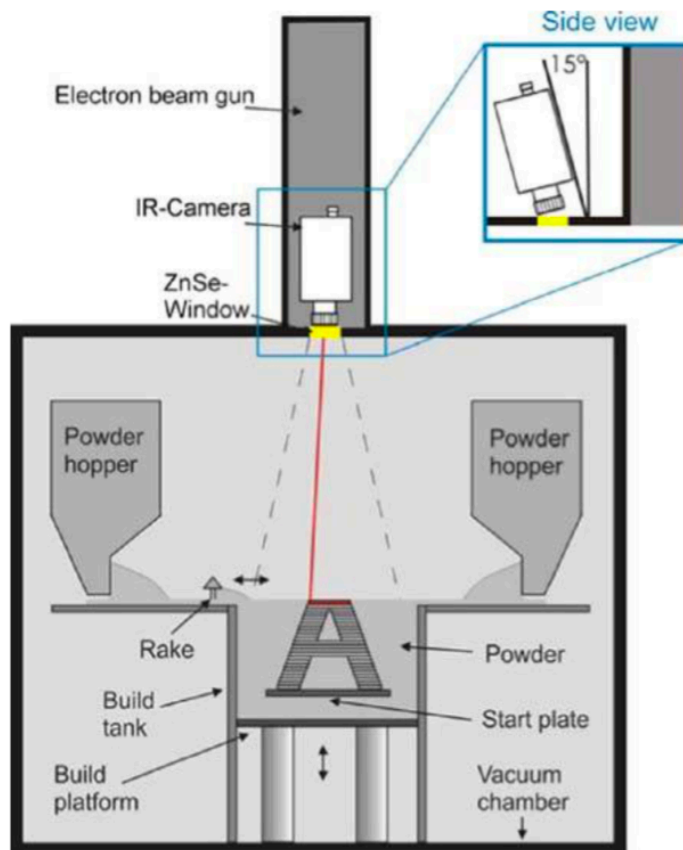


Figure 90 Side view of the IR-camera setup mounted with a 15° angle relative to the beam column. From [124].

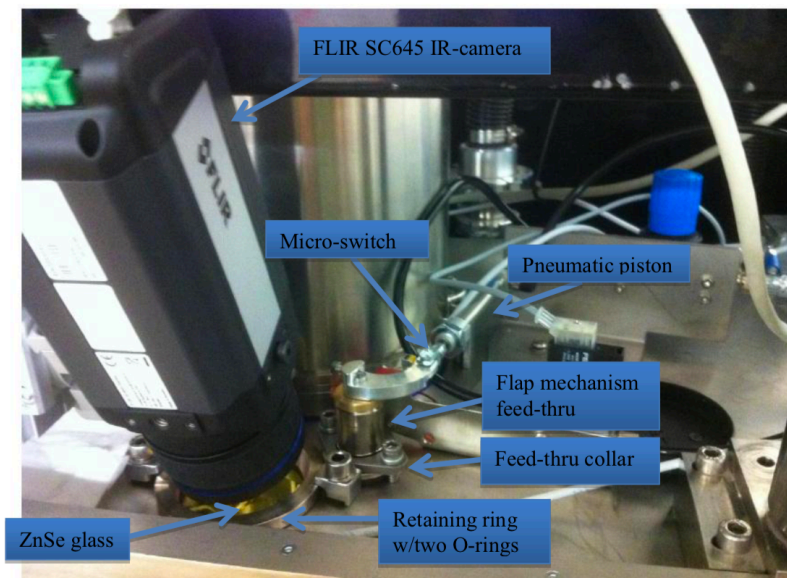


Figure 91 Top of Arcam-A2 build chamber with new component location and IR-camera. From [123].

## 8. Conclusions

In the subscribed work, comparisons between the two EBM process methodology were studied in terms of: Microstructure, Mechanical properties and Macro instrumented indentation test, studying the relations among the parameters and discussing the results. The development of a MatLab model gave an additional tool to better understand the connections between microstructure, mechanical properties and process parameters, even if the results of the simulations were affected by approximation errors and were not compared with the real operating temperatures.

Mainly 4 Macro groups were discussed:

### 1) Microstructure

The porosity of the specimens through the Archimedes' principle was analyzed and an average value of  $4.39 \frac{g}{cm^3}$  was found for the samples "a, c and d" while a slightly lower value for the sample "b" was detected.

The observed microstructure is called "graded microstructure" since it varies with the distance from the build plate. Three macro areas have been observed: i) Bottom part: consisting of prior equiaxed  $\beta$  grains due to the isotropic heat flow, within which there is a mixed structure of  $\alpha$  lamellae (with columnar structure or with Widmanstätten morphology) and  $\beta$  phase. ii) Core part: is the transition zone between the prior equiaxed beta grains and the prior columnar  $\beta$  grains. Within these primary grains there is still a mixed  $\alpha + \beta$  microstructure, finer than that of the bottom part. iii) Top part: consisting of prior columnar  $\beta$  grains due to the hindered atomic diffusion by rapid cooling. Within these prior columnar  $\beta$  grains, very fine  $\alpha + \beta$  phase (perhaps martensite on the topmost surface) was inspected.

The sample 'a', obtained through the BTM, appeared to have many defects in terms of unfused layers and microporosities. The microstructure was quite fine compared to other cases even if the shape and size of the specimens were affected by very pronounced deformations to make the samples not suitable for the project specifications. The sample 'd' was the best obtained, showing a fine microstructure, with a good distribution of the pores and free non-fused zones.

### 2) Tensile test

The UTS values were 1047 Mpa for the specimen produced with the BTM and ranged between 992 and 1065 Mpa for the specimens made with the MM. The Young modulus was minimal for the sample 'a' (107 GPa) and was maximum for the sample 'd' (116 GPa) while the other two specimens had intermediate values. The elongation was minimal for the sample 'c' (11.7%) and was almost the same in the other cases (12 ÷ 12.6)%.

### 3) Macro instrumented indentation test (MII)

The specimens were subjected to the MII test using a load of 300 N. It was observed that the Ti-6Al-4V material responded very positively to the test, showing comparable results to the traditional tensile test. As for Indentation hardness (Hit), higher values were obtained for the samples 'a' and 'd' and lower values for the samples 'b' and 'c' [Figure 72]. These values were converted to equivalent Vickers hardness values [Figure 74] and were fairly in agreement with the real Vickers hardness values found in the literature. Regarding the indentation modulus, lower 'Eit' values for the samples 'b' and 'c' were obtained and higher values for the samples 'a' and 'd' were inspected [Figure 71]. On average, the values in [Figure 71] were quite in agreement with those found in the tensile test [Figure 64]. It was verified that indentation hardness increased as the microstructure size decreased. The UTS values obtained through the Tabor formula ( $H_{it} / 3$ ) were compared with the real UTS values, and similar results were obtained with an error less than 20%.

### 4) EBM simplified model

A MatLab model was developed both to predict the temperature distribution on the surface of the material and to create links between microstructure, mechanical properties and process parameters. The model showed results that were in agreement with the literature in terms of trend and maximum temperatures. Temperatures that were too high would lead to major deformations because the shrinkage stresses and probable trapping of evaporated gases during the cooling step, instead, too low temperatures would lead the formation of unfused layers and porosities. About the performed work, the sample 'a' showed higher temperatures, causing pronounced defects and distortions of the material. The sample 'd', which was the best obtained, exhibited much lower temperature than the sample 'a', ensuring good microstructure, mechanical properties and well congruence with the design dimensions.

5) Making a general report, the sample 'd' ( $I = 12 \text{ mA}$ ,  $v = 4.53 \text{ m / s}$ ) was the one that showed the best results in terms of shape, geometry, microstructure and mechanical properties. This conclusion does not mean that the MM is better than the BTM, but it is a proof that the BTM is not always the best methodology to adopt. Generally, the BTM leads to advantages when the current variation range is correctly chosen, generating homogeneous density and temperatures over the entire surface. In this work, the 98 preset speed factor parameter (speed function 98) was adopted, which did not seem to lead to optimal results. The MM, however, is more difficult to calibrate but presents excellent results in maximum yield conditions.

# References

- [1] V. T. L. H. P. M. S. Guillaume Mandil, *Building new entities from existing titanium part by electron beam melting: microstructures and mechanical properties*, International Journal of Advanced Manufacturing Technology, Springer Verlag, 2015, <10.1007/s00170-015-8049-3>. <hal-01230836v1>, 2015.
- [2] A. Neira Arce, «Thermal Modeling and Simulation of Electron Beam Melting for Rapid Prototyping on Ti6Al4V Alloys.,» North Carolina State University, 2012.
- [3] J. Emsley, «Nature's building blocks: an A-Z guide to the elements.,» 2001.
- [4] F. M. G. a. M. A. I. Froes, Cost-affordable titanium: The component fabrication perspective., JOM Journal of the Minerals, Metals and Materials Society, 2007.
- [5] R. Boyer, «Attributes, characteristics, and applications of titanium and its alloys.,» in *JOM Journal of the Minerals, Metals and Materials Society*, 2010.
- [6] K. C. M. B. ., N. S. D. S. A. S. P. W. H. Yamamoto Y., «Consolidation Process in Near Net Shape Manufacturing of Armstrong CP-Ti/Ti- 6Al-4V Powders, in Cost Affordable Titanium III,» vol. T.P. Switzerland, 2010.
- [7] H. T. C. a. J. M. Salimijazi, «Vacuum plasma spraying: A new concept for manufacturing Ti-6Al-4V structures.,» 2006.
- [8] M. a. F. F. Ashraf Imam, «TMS 2010 symposium: Cost-Affordable Titanium III.,» in *OM Journal of the Minerals, Metals and Materials Society*, 2010.
- [9] G. D. Thomas, *Additive Manufacturing for the Aerospace Industry, in American Helicopter Society 68th Annual Forum*, American Helicopter Society International, Inc.: Fort Worth, Texas.: Southeastern Tool & Die – Additive Manufacturing Division, 2012.
- [10] P. H. J. L. Leblanc, On Vacuum Plasma Spray Forming of Ti-6Al-4V, in *Thermal Spray 2003: Advancing the Science and Applying the Technology.,* B.R.M.a.C. Moreau, 2003.
- [11] Y. a. Z. X. Xu, «Interstitial segregation and embrittlement in Ti-6Al-4V alloy.,» JOURNAL OF MATERIALS SCIENCE., 1990.

- [12] M. K. G. L. C. G. K. R. O. T. Koike M, «Evaluation of titanium alloy fabricated using electron beam melting system for dental applications.,» Vol. %1 di %2J Mater Process Technol 211(8):1400-1408. doi:10.1016/j.jmatprotec.2011.03.013, 2011.
- [13] L. P. D. R. B. J.-. J. V. F. V. F. Suard M, «Towards stiffness prediction of cellular structures made by electron beam melting (EBM),» Vol. %1 di %2Powder Metall 57(3):190-195. doi:10.1179/1743290114Y.0000000093, 2014.
- [14] S. A. E. H. L. J. Karlsson J, *Characterization and comparison of materials produced by Electron Beam Melting (EBM) of two different Ti6Al4V powder frac- tions*, Vol. %1 di %2J Mater Process Technol 213(12):2109-2118. doi:10.1016/j.jmatprotec.2013.06.010, J Mater Process Technol 213(12):2109-2118. doi:10.1016/j.jmatprotec.2013.06.010, 2013.
- [15] G. P. O. K. e. a. Koike M, *Eval- uation of Titanium Alloys Fabricated Using Rapid Prototyping Technologies-Electron Beam Melting and Laser Beam Melting. Materials*, (Basel) 4(12):1776- 1792. doi:10.3390/ma4101776, 2011.
- [16] K. N. G. H. S. T. S. B. Rafi HK, *Microstructures and Mechanical Proper- ties of Ti6Al4V Parts Fabricated by Selective Laser Melting and Electron Beam Melting*, J Mater Eng Perform 22(12):3872-3883. doi:10.1007/s11665-013- 0658-0, 2013.
- [17] M. E. R. P. M. A. Facchini L, *Microstructure and mechanical properties of Ti-6Al-4V produced by electron beam melting of pre- alloyed powders.*, Rapid Prototyp J 15(3):171-178. doi:10.1108/13552540910960262, 2009.
- [18] Q. S. G. S. e. a. Murr LE, *Microstructure and mechanical behavior of Ti-6Al-4V produced by rapid-layer manufacturing, for biomed- ical applications.*, J Mech Behav Biomed Mater 2(1):20-32. doi:10.1016/j.jmbbm.2008.05.004, 2009.
- [19] B. M. Z. W. T. I. Al-Bermani SS, *The Origin of Microstructural Diversity, Texture, and Mechanical Properties in Electron Beam Melted Ti-6Al-4V.*, Metall Mater Trans A 41(13):3422-3434. doi:10.1007/s11661-010-0397-x, 2010.
- [20] A.-S. H. A.-A. A. A.-. W. K. M. M. Syam WP, *Preliminary fabri- cation of thin-wall structure of Ti6Al4V for dental restoration by electron beam melting*, Rapid Proto- typ J 18(3):230-240. doi:10.1108/13552541211218180, 2012.
- [21] G. W. L. F. Guo C, *Effects of scan- ning parameters on material deposition during Electron Beam Selective Melting of Ti-6Al-4V powder.*, J Mater Process Technol 217:148-157. doi:10.1016/j.jmatprotec.2014.11.010, 2015.
- [22] W. J. H. L. H. T. X. K. Y. H. Weiwei H, *Research on Preheating of Titanium Alloy Powder in Electron Beam Melting Technology.*, Rare Met Mater Eng 40(12):2072-2075. doi:10.1016/S1875-5372(12)60014-9, 2011.
- [23] T. Q. Nikolas Hrabe, *Effects of processing on microstructure and mechanical properties of a titanium alloy (Ti-6Al-4V) fabricated using electron beam melting*

- (EBM), part 1: Distance from build plate and part size, National Institute of Standards and Technology (NIST), 325 Broadway, Stop 647, Boulder, CO 80305-3328, USA, 2013.
- [24] R. K. T. Q. Nikolas Hrabe, *Effects of Processing on Microstructure and Mechanical Properties of Ti-6Al-4V Fabricated using Electron Beam Melting (EBM): Orientation and Location\**, National Institute of Standards and Technology (NIST), Boulder, CO.
- [25] S. M. G. D. A. R. E. M. J. H. K. N. A. P. W. S. F. R. M. a. R. B. W. Lawrence E. Murr, *Metal Fabrication by Additive Manufacturing Using Laser and Electron Beam Melting Technologies*, Department of Metallurgical and Materials Engineering, The University of Texas at El Paso, El Paso, TX 79968, USA, 2012.
- [26] L. M. Guo N, *Additive manufacturing: technology, applications and research needs.*, *Front Mech Eng* 8(3):215-243. doi:10.1007/s11465-013-0248-8, 2013.
- [27] F. WE, *Metal Additive Manufacturing: A Review.*, *J Mater Eng Perform* 23(6):19171928. doi:10.1007/s11665-014-0958-z.
- [28] L. P. M. A. H. L. Huang S, *Additive manufacturing and its societal impact: a literature review.*, *Int J Adv Manuf Technol* 67(5-8):1191-1203. doi:10.1007/s00170-012-4558-5.
- [29] R. D. S. B. Gibson I, *Additive Manufacturing Technologies*, Boston, MA: Springer US. doi:10.1007/978-1-4419-1120-9, 2010.
- [30] R. Hague R.J.M., *Rapid Prototyping, Tooling, and Fabrication Rapra Review Reports*, ed. R.T. Ltd. 2000..
- [31] D. J.R, *Heat-resistant materials*, Technology & Engineering, ed. A. International. 1997, Materials Park, OH. .
- [32] D. Bäuerle, *Chemical processing with lasers.*, Technology & Engineering, ed. Springer-Verlag. 1986. 245 .
- [33] K. Zäh M. F., *Elektronenstrahl für das selektive Sintern von metallischen Pulvern nutzen*, in *Euro-uRapid2006*. 2006. Frankfurt..
- [34] K. Zaeh M., *The effect of scanning strategies on electron beam sintering*, 3. *Production Engineering*(3): p. 217-224., 2009.
- [35] W. F. J. R. B. Burkins M., *The Mechanical and Ballistic Properties of an Electron Beam Single Melt of Ti-6Al-4V Plate*, A.R.L. ARL, Editor. 2001, Army Research Laboratory: Aberdeen probing Ground, MD 21005., 2001.

- [36] D. S. V. Dandekar, *Shock Response of Ti-6Al-4V*, in *Conference on Shock Compression of Condensed Matter*, American Physical Society: Snowbird, Utah. , 1999.
- [37] A. S. H. H. L.-Y. W. A. S. L. E. C. d. Paz, *Effect of process parameters settings and thickness on surface roughness of EBM produced Ti-6Al-4V*, *Rapid Prototyping Journal*, Vol. 18 Iss 5 pp. 401 - 408, 2012.
- [38] G. S. C. A. e. a. Murr LE, *Characterization of titanium aluminide alloy components fabricated by additive manufacturing using electron beam melting.*, *Acta Mater* 58(5):1887-1894. doi:10.1016/j.actamat.2009.11.032, 2010.
- [39] H. O. W. H. Cormier D, *Characterization of high alloy steel produced via electron beam melting.*, *Proc Solid Free Fabr Symp*:548-558, 2003.
- [40] M. E. G. S. e. a. Murr LE, *Microstructural Architecture, Microstructures, and Mechanical Properties for a Nickel-Base Superalloy Fabricated by Electron Beam Melting*, *Metall Mater Trans A* 42(11):3491-3508. doi:10.1007/s11661-011-0748-2, 2011.
- [41] M. E. P. X. e. a. Murr LE, *Microstructures of Rene 142 nickel-based superalloy fabricated by electron beam melting.*, *Acta Mater* 61(11):4289-4296. doi:10.1016/j.actamat.2013.04.002, 2013.
- [42] M. L. M. E. e. a. Ramirez DA, *Novel precipitate-microstructural architecture developed in the fabrication of solid copper components by additive manufacturing using electron beam melting.*, *Acta Mater* 59(10):4088-4099. doi:http://dx.doi.org/10.1016/j.actamat.2011.03.033, 2011.
- [43] H. O. R. D. Frigola P, *Fabricating Copper Components with Electron Beam Melting.*, *Adv Mater Process* 172(7) (ASM International, 2014).
- [44] D. H. O. a. W. H. Cormeir, *Characterization of H13 steel produced via electron beam melting*, *Rapid Prototyping Journal*, Vol. 10 No. 1, pp. 35-41., 2004.
- [45] K. Cooper, *Direct digital manufacturing with layer by layer melt deposition processes*, *Supplemental Proceedings Vol. 1 TMS.*, 2009.
- [46] L. E. E. Q. S. G. S. L. M. a. M. E. Murr, *Microstructures and mechanical properties of electron beam-rapid manufactured Ti-6Al-4V biomedical prototypes compared to wrought Ti-6Al-4V*, *Materials Characterization*, Vol. 60 No. 2, pp. 96-105., 2009.
- [47] A. T. N. Z. V. I. O. M. P. T. R. a. S. S. Kalinyuk, *Microstructure, texture and mechanical properties of electron beam melted Ti-6Al-4V*, *Material Science and Engineering A*, Vol. 346, pp. 178-88., 2003.
- [48] Arcam, EBM User 's Manual.

- [49] S. M. L. M. F. M. E. L. M. a. W. R. Gaytan, *Advanced metal powder-based manufacturing of complex components by electron beam melting.*, Materials Technology, in press., 2009.
- [50] Y. K. ., Y. J. T. ., M. D. ., D. M. ., S. B. T. ., K. F. L. ., C. K. C. Xipeng Tan, *Graded microstructure and mechanical properties of additive manufactured Ti-6Al-4V via electron beam melting*, ingapore Centre for 3D Printing, School of Mechanical and Aerospace Engineering, Nanyang Technological University, 2015.
- [51] Y. K. W. Q. T. Y. J. T. M. D. D. M. S. B. T. K. F. L. &. C. K. C. Xipeng Tan, *Revealing martensitic transformation and  $\alpha/\beta$  interface evolution in electron beam melting three-dimensional-printed Ti-6Al-4V*, 2016.
- [52] M. B. W. Z. I. T. S.S. Al-Bermani, *The origin of microstructural diversity, texture, and mechanical properties in electron beam melted Ti-6Al-4V.*, Metall. Mater. Trans. A 41 (2010) 3422–3434..
- [53] X. T. S. T. C. C. Y.H. Kok, *Fabrication and microstructural characterisation of additive manufactured Ti-6Al-4V parts by electron beam melting*, Virtual Phys., Prototyp. 10 (2015) 13–21..
- [54] W. Z. K. K. M. M. J. Sieniawski, *Microstructure and mechanical properties of high strength two-phase titanium alloys*, Titan. Alloy. Prop. Control (2013) 69–80..
- [55] H. R. T. Ahmed, *Phase transformations during cooling in  $\alpha + \beta$  titanium alloys*, Mater. Sci. Eng. A 243 (1998) 206–211..
- [56] G. W. E. C. R. Boyer, *Materials Properties Handbook: Titanium Alloys*, Materials Park (OH), 1994..
- [57] d. L.-Y. W. A. S. Z. L. A. Safdar, *Evaluation of microstructural development in electron beam melted Ti-6Al-4V*, Elsevier, 2011.
- [58] R. Cagliero, *Ph.D. Thesis: Macro instrumented indentation test for structural materials: experimental and numerical methods*, Politecnico di Torino, 2016.
- [59] S. IN., *The relation between load and penetration in the axisymmetric Boussinesq problem for a punch of arbitrary profile.*, International Journal of Engineering Science 1965, (3):47-57..
- [60] *ISO/TR 29381:2008(E) - Measurement of mechanical properties by an instrumented indentation test - Indentation tensile properties.*, Metallic materials.
- [61] A. I., *Frictionless and adhesive nanoindentation: Asymptotic modeling of size effects.*, Mechanics of Materials 2010; 42(8):807-815..
- [62] K. L. H. G. M. L. Hayes WC, *A mathematical analysis for indentation tests of articular cartilage.*, Journal of Biomechanics 1972; 5(5):541-551..

- [63] C. C. L. J. Gao H, *Elastic contact versus indentation modeling of multi-layered materials.*, International Journal of Solids and Structures 1992; 29(20):2471-2492. .
- [64] B. E. Perriot A, *Elastic contact to a coated half-space: Effective elastic modulus and real penetration*, Journal of Materials Research 2004; 19(2):600-608..
- [65] D. A. M. G. R. S. W. D. Argatov I, *Accounting for the thickness effect in dynamic spherical indentation of a viscoelastic layer: Application to non-destructive testing of articular cartilage.*, European Journal of Mechanics A/Solids 2013; 37:304-317..
- [66] H. IM., *The contribution of David Tabor to the science of indentation hardness*, Journal of Materials Research 2009; 24(3):581-589..
- [67] B. G. M. G. G. G. Cagliero R, *Measurement of elastic modulus by instrumented indentation in the macro-range: Uncertainty evaluation.*, International Journal of Mechanical Sciences 2015; 101-102:161-169..
- [68] *ISO 14577-4:2007 - Instrumented indentation test for hardness and materials parameters - Part 4: Test method for metallic and non-metallic coatings.*, Metallic materials.
- [69] M. G. B. G. Cagliero R, *Unconventional mechanical testing for process set up and product qualification in additive manufacturing.*, Polaris Innovation Journal 2015; 25:18-25. .
- [70] *BS EN ISO 6507-2:2005 - Vickers hardness test. Verification and calibration of testing machines.*, Metallic materials..
- [71] *ASTM E92-82(2003) - Standard Test Method for Vickers Hardness of Metallic Materials.*..
- [72] *ASTM E384 - 11e1 - Standard Test Method for Knoop and Vickers Hardness of Materials.*..
- [73] *ISO 14577-1:2002 - Instrumented indentation test for hardness and materials parameters - Part 1: Test method.*, Metallic materials.
- [74] J. N. Chudoba T, *Higher accuracy analysis of instrumented indentation data obtained with pointed indenters*, Journal of Physics D: Applied Physics 2008; 41(215407):1-16..
- [75] *ISO 14577-2:2002 - Instrumented indentation test for hardness and materials parameters*, Metallic materials.
- [76] P. G. Oliver WC, *An improved technique for determining hardness and elastic modulus using load and displacement sensing indentation experiments.*, Journal of Materials Research 1992; 7(6):1564-1583..

- [77] P. G. O. W. L. B. H. J. Herbert EG, *On the measurement of stress–strain curves by spherical indentation.*, Thin Solid Films 2001; 398–399:331–335..
- [78] ASTM E1876 - 09 - *Standard Test Method for Dynamic Young's Modulus, Shear Modulus, and Poisson's Ratio by Impulse Excitation of Vibration.*
- [79] F.-C. AC., *Nanoindentation*. 2nd ed. New York: Springer; 2003..
- [80] G. J. M. O. M. G. Loubet JL, *Vickers indentation curves of magnesium oxide (MgO)*, Journal of Tribology 1984; 106(1):43-48..
- [81] N. W. Doerner MF, *A method for interpreting the data from depth-sensing indentation instruments.*, Journal of Materials Research 1986; 1(.
- [82] H. R. O. W. Pethica JB, *Hardness measurement at penetration depths as small as 20 nm.*, Philosophical Magazine A 1983; 48(4):593-606..
- [83] M. S. H. S. Philipp Drescher, *An Investigation of Sintering Parameters on Titanium Powder for Electron Beam Melting Processing Optimization*, Fluid Technology and Microfluidics, University of Rostock, Justus-von-Liebig Weg 6, 18059 Rostock, Germany;; Jai-Sung Lee, 2016.
- [84] P. R. T. a. S. H. Drescher, *Investigation of powder removal of net-structured titanium parts made from electron beam melting*, Int. J. Rapid Manufacturing, Vol. 4, Nos. 2/3/4, pp.81–89., 2014.
- [85] X. T. S. B. T. a. C. K. C. Yihong Kok, *Fabrication and microstructural characterisation of additive manufactured Ti-6Al-4V parts by electron beam melting*, Virtual and Physical Prototyping, 2015 Vol. 10, No. 1, 13–21, <http://dx.doi.org/10.1080/17452759.2015.1008643>, 2015.
- [86] P. D. ., R. B. ., H. S. ., H. H. a. N. L. Volker Weißmann, *Comparison of Single Ti6Al4V Struts Made Using Selective Laser Melting and Electron Beam Melting Subject to Part Orientation*, Manoj Gupta, 2017.
- [87] H. P. D.P. DeLo, *Early stage consolidation mechanisms during hot isostatic pressing of Ti–6Al–4V powder compacts*, Department of Materials Science and Engineering, Carnegie Mellon University, Pittsburgh, PA 15213, U.S.A., 1999.
- [88] L. E. M. S. M. G. E. M. F. M. R. B. W. Karina Puebla, *Effect of Melt Scan Rate on Microstructure and Macrostructure for Electron Beam Melting of Ti-6Al-4V*, University of Texas at El Paso, El Paso, USA.: Materials Sciences and Applications, 2012, 3, 259-264.
- [89] T. D., *The hardness of metals.*, Oxford: Clarendon Press, 1951..
- [90] T. G. (. H.E. Boyer, *Metals Handbook, Desk Edition, ASM International, Metals Park, Ohio, 1985.*

- [91] W. C. Jr., *Materials Science and Engineering – An Introduction*, John- Wiley, NewYork, 1992..
- [92] S. L. Z. Z. P. Zhang, *General relationship between strength and hardness*, Shenyang National Laboratory for Materials Science, Institute of Metal Research, Chinese Academy of Sciences, Shenyang 110016, PR China.
- [93] S. P. J. L. K. C. K. C. Bo Cheng, *On Process Temperature in Powder-Bed Electron Beam Additive Manufacturing: Model Development and Validation*, [DOI: 10.1115/1.4028484].
- [94] N. S. a. K. Chou, *THERMAL MODELING OF ELECTRON BEAM ADDITIVE MANUFACTURING PROCESS - POWDER SINTERING EFFECTS*, Proceedings of the ASME 2012 International Manufacturing Science and Engineering Conference MSEC2012, 2012.
- [95] E. Attar, *Simulation of Selective Electron Beam Melting Processes*, Universita ıt Erlangen-Nu ırnberg.
- [96] J. V. D. A. B. D. J. S. a. U. P. A. POWELL, *Analysis of Multicomponent Evaporation in Electron Beam Melting and Refining of Titanium Alloys*.
- [97] M. F. a. L. S. Zah, *Modeling and Simulation of Electron Beam Melting*, Prod. Eng. Res. Develop., 4(1), pp. 15–23., 2010.
- [98] C. W. B. a. Z. J. Liu, *Numerical Investigation of Residual Stress in Thick Titanium Alloy Plate Joined With Electron Beam Welding*, Metall. Mater. Trans. B, 41(5), pp. 1129–1138., 2010.
- [99] Y. L. J. a. Y. H. Luo, *An Analytical Model and Tomographic Cal- culation of Vacuum Electron Beam Welding Heat Source*, Vacuum, 84(6), pp. 857–863..
- [100] P. a. A. K. Lacki, *Numerical Simulation of the Electron Beam Welding Process*, Comput. Struct., 89(11–12), pp. 977–985., 2011.
- [101] S. G. J. a. L. M. P. Rouquette, *Estimation of the Parameters of a Gaussian Heat Source by the Levenberg–Marquardt Method: Application to the Electron Beam Welding*, Int. J. Therm. Sci., 46(2), pp. 128–138., 2007.
- [102] H. a. G. Hemmer, *Prediction of Penetration Depths During Electron Beam Welding*, Sci. Technol. Weld. Joining, 4(4), pp. 219–225., 1999.
- [103] L. F. S. G. Y. W. P. T. a. H. M. F. Wang, *Optimization of the LENS Process for Steady Molten Pool Size*, Mater. Sci. Eng. A, 474(1–2), pp. 148–156., 2008.
- [104] I. A. W. C. J. E. R. S. M. a. M. D. J. Roberts, *A Three-Dimensional Finite Element Analysis of the Temperature Field Dur- ing Laser Melting of Metal Powders in Additive Layer Manufacturing*, Int. J. Mach. Tools Manuf., 49(12–13), pp. 916–923..

- [105] K. T. J. F. a. G. M. Lankalapalli, *A Model for Estimating Penetration Depth of Laser Welding Processes*, J. Phys. D: Appl. Phys., 29(7), pp. 1831–1841., 1996.
- [106] S. A. P. P. a. K. T. Tsirkas, *Numerical Simulation of the Laser Welding Process in Butt-Joint Specimens*, J. Mater. Process. Technol., 134(1), pp. 59–69., 2003.
- [107] S. B. Patricio Mendez, *Modeling of Selected SFF Process Limits*, Department of Materials Science and Engineering Massachusetts Institute of Technology.
- [108] E. M. B. a. B. H. K. L. E. Greenwald, *Heat transfer properties and microstructures of laser surface melted alloys*, AIP Conference Proceedings 50, 189 (1979); doi: 10.1063/1.31658.
- [109] K. C. Mills, *Recommended Values of Thermophysical Properties for Selected Commercial Alloys*, Woodhead Publishing, 2002.
- [110] M. K. A. A. T. L. a. L. F. Nikolay K. Tolochko, *Mechanisms of selective laser sintering and heat transfer in Ti powder*, Rapid Prototyping Journal, Vol. 9 Issue: 5, pp.314-326, 2003.
- [111] C. C. D. D. V. E. M.-H. N. B. W. a. G. P. M. Boivineau, *Thermophysical Properties of Solid and Liquid Ti-6Al-4V (TA6V) Alloy*.
- [112] D. H. R. K. M. LABUDOVIĆ, *A three dimensional model for direct laser metal powder deposition and rapid prototyping*, JOURNAL OF MATERIALS SCIENCE 38 (2003)35–49, 2003.
- [113] .. H. S. C. a. C. JAEGER, *Conduction of Heat in Solids*, (Clarendon Press, Oxford, UK, 1959) p. 134..
- [114] M. Ozisik, *Boundary Value Problems of heat conduction*, Inter. Textbook Co., 1968.
- [115] S. S. S. & J. W. BARLOW, *The Prediction of the Emissivity and Thermal Conductivity of Powder Beds*, Particulate Science and Technology: An International Journal, 22:3, 291-304, DOI: 10.1080/02726350490501682a, 2004.
- [116] A. McCormick, Brooks e R. F, *McCormick, A; Brooks, R F: MTS Programme on processability: Thermophysical property data for commercial alloys measured in PMP19 2 and 3*, (Apr 93-Mar 96), NPL (1996) Chapter 1., 1996.
- [117] A. Luikov, *Heat and Mass Transfer. Handbook*, Energia, Moscow., 1971.
- [118] Y. a. R. Y. Zel'dovich, *Physics of Shock Waves and High-temperature Hydrodynamic Phenomena*, Vol. 2, Academic Press, New York., 1967.
- [119] V. a. S. Skorohod, *Physical-Metallurgic Basics of Powder Sintering*, Metallurgiya, Moscow., 1984.

- [120] M. F. Z. . • S. Lutzmann, *Modelling and simulation of electron beam melting*, Prod. Eng. Res. Devel. (2010) 4:15–23 DOI 10.1007/s11740-009-0197-6, 2010.
- [121] S. O. T.-M. C. I. E. B. A. MANUFACTURING, *Ninggang Shen and Kevin Chou*, Mechanical Engineering Department The University of Alabama Tuscaloosa, AL 35487, 2012.
- [122] M. M. K. P. D. L. R. R. D. L. E. L. G. S. M. R. B. Dinwiddie, *Calibrating IR Cameras for In-Situ Temperature Measurement During the Electron Beam Melting Process using Inconel 718 and Ti-Al6-V4*, Oak Ridge National Laboratory, Manufacturing Demonstration Facility, 2370 Cherahala Blvd., Knoxville TN 37932-1563, 2013.
- [123] F. M. D. E. C. T. D. M. C. H. E. M. a. R. B. W. Emmanuel Rodriguez, *Integration of a Thermal Imaging Feedback Control System in Electron Beam Melting*, W.M. Keck Center for 3D Innovation, The University of Texas at El Paso, El Paso, TX 79968, USA 2Lockheed Martin Aeronautics Company, Marietta, GA 30063, USA.
- [124] R. F. S. C. K. Jan Schwerdtfeger, *In situ flaw detection by IR-imaging during electron beam melting*, Rapid Prototyping Journal, Vol. 18 Issue: 4, pp.259-263, <https://doi.org/10.1108/13552541211231572>.
- [125] S. M. G. F. M. E. M. H. H. M. M. I. L. R. B. W. a. S. C. L. E. Murr, *EFFECT OF BUILD PARAMETERS AND BUILD GEOMETRIES ON RESIDUAL MICROSTRUCTURES AND MECHANICAL PROPERTIES OF Ti-6Al-4V COMPONENTS BUILT BY ELECTRON BEAM MELTING (EBM)*, Department of Metallurgical and Materials Engineering The University of Texas at El Paso, El Paso, TX 79968 USA, 2009.
- [126] J. W. A. G. G. Lütjering, *Microstructure and mechanical properties of titanium alloys*, J.C.M. Li (Ed.), *Microstruct. Prop. Mater.*, World Scientific, Singapore, 1998, pp. 1–77..

# Acknowledgments

Ripensare ai momenti, alle esperienze e alle emozioni accumulate durante questo percorso di vita mi rende un uomo fiero, felice e consapevole dei sacrifici che sono stati fatti in tutti questi anni. Lo sforzo, l'impegno continuo e gli stimoli che le persone mi hanno trasmesso, mi hanno guidato verso obiettivi notevoli, di cui mi sento veramente orgoglioso. Il raggiungimento di questo traguardo, pertanto, è frutto di un lavoro congiunto di persone che hanno contribuito direttamente e indirettamente a fortificare il mio spirito e la mia voglia di fare.

Mi sento di ringraziare il Prof. Giovanni Maizza, che mi ha dato la possibilità di svolgere questo importante lavoro di tesi in collaborazione con l'Università di Rostock, spronandomi ed affiancandomi nei momenti di difficoltà sia in Italia che all'estero.

Vorrei ringraziare i miei genitori, per avermi sostenuto ed essersi fatti carico delle mie preoccupazioni e delle mie problematiche. Li ringrazio per avermi aiutato in ogni momento, con ogni mezzo, credendo sempre nelle mie capacità e nella mia voglia di fare.

Ringrazio la mia compagna Martina, dalla quale è partito tutto. La ringrazio per il sostenimento continuo, sia fuori che dentro l'università. La ringrazio per aver creduto sempre in me, per i confronti di idee, per i consigli, per la sua capacità di ascolto e di critica e per avermi insegnato i valori fondamentali della vita. Se oggi sono quello che sono, dovrei dedicare a lei questo premio.

Infine, non per minore importanza, vorrei ringraziare tutti gli amici e i parenti che hanno contribuito a sostenermi moralmente, spronandomi a dare sempre il meglio ed aiutandomi a crescere come persona, come amico e come uomo. Grazie a tutti.